

DYNAMICAL EVOLUTION OF COSMIC SUPERMASSIVE BINARY BLACK HOLES AND THEIR GRAVITATIONAL WAVE RADIATION

YUNFENG CHEN¹, QINGJUAN YU^{1,†}, AND YOUJUN LU^{2,3}

¹ Kavli Institute for Astronomy and Astrophysics, and School of Physics, Peking University, Beijing, 100871, China; †yuqj@pku.edu.cn

² National Astronomical Observatories, Chinese Academy of Sciences, Beijing, 100012, China

³ School of Astronomy and Space Science, University of Chinese Academy of Sciences, Beijing 100049, China

Draft version July 24, 2020

ABSTRACT

We investigate the evolution of supermassive binary black holes (BBHs) in galaxies with realistic property distributions and the gravitational-wave (GW) radiation from the cosmic population of these BBHs. We incorporate a comprehensive treatment of the dynamical interactions of the BBHs with their environments by including the effects of galaxy triaxial shapes and inner stellar distributions, and generate a large number of BBH evolution tracks. By combining these BBH evolution tracks, galaxy mass functions, galaxy merger rates, and supermassive black hole–host galaxy relations into our model, we obtain the statistical distributions of surviving BBHs, BBH coalescence rates, the strength of their GW radiation, and the stochastic GW background (GWB) contributed by the cosmic BBH population. About $\sim 1\%$ – 3% (or $\sim 10\%$) of supermassive BHs at nearby galactic centers are expected to be binaries with mass ratio $> 1/3$ (or $> 1/100$). The characteristic strain amplitude of the GWB at frequency 1 yr^{-1} is estimated to be $\sim 2.0_{-0.8}^{+1.4} \times 10^{-16}$, and the upper bound of its results obtained with the different BH–host galaxy relations can be up to 5.4×10^{-16} , which await testing by future experiments (e.g., the Square Kilometer Array, FAST, Next-Generation Very Large Array). The turnover frequency of the GWB spectrum is at $\sim 0.25 \text{ nHz}$. The uncertainties on the above estimates and prospects for detecting individual sources are also discussed. The application of the cosmic BBH population to the Laser Interferometer Space Antenna (LISA) band provides a lower limit to the detection rate of BBHs by LISA, $\sim 0.9 \text{ yr}^{-1}$.

Keywords: Astrodynamics (76); Gravitational waves (678); Cosmological evolution (336); Galaxy dynamics (591); Galaxy mergers (608); Galaxy nuclei (609); Gravitational wave astronomy (675); Supermassive black holes (1663)

1. INTRODUCTION

In the modern paradigm of hierarchical galaxy formation and evolution, a natural consequence of mergers of galaxies with central supermassive black holes (SMBHs, hereafter BHs) is the formation of supermassive binary black holes (SMBBHs, hereafter BBHs) at galactic centers (e.g., Begelman et al. 1980; Yu 2002; Benson et al. 2010). The formed binaries interact with surrounding stars and gas, which may distinguish the systems with some unique astronomical phenomena different from those with only one BH. If the separation of the two BHs can decay to be sufficiently close through the interactions, significant gravitational waves (GWs) will be radiated, taking away energy and angular momentum, leading to mergers of the BBHs, and contributing to the GW background (GWB) at the relatively low-frequency band [e.g., the detection frequency bands of the Pulsar Timing Array (PTA) experiments (Hobbs 2013; McLaughlin 2013; Desvignes et al. 2016; Verbiest et al. 2016), Laser Interferometer Space Antenna (LISA; <https://www.lisamission.org>), and Taiji/Tianqin (Ruan et al. 2019; Wang et al. 2019)]. Studies of the strength of the GW radiation caused by BBH mergers, the characteristics of BBH systems and their statistical properties, would provide an important probe to the hierarchical structure formation and evolution model, BH physics, and the gravitation theory.

In this work, we investigate the expected statistical

distributions of BBHs surviving in the nearby universe and the strength of the GWs radiated by merging BBHs. To determine how many BBHs can survive or coalesce, the dynamical evolution timescales of BBHs play a vital role. For example, Yu (2002) shows that the evolution of BBHs in a gas-poor system depends on BH mass ratio and host galaxy type. BBHs with very low mass ratios (say, $\lesssim 0.001$) are hardly formed by mergers of galaxies, because the dynamical friction timescale is too long for the smaller BH to sink into the galactic center within a Hubble time. For BBHs with moderate mass ratios, one essential factor to determine their evolution timescales is how many stars can pass by the vicinity of the BBH to interact strongly with the BBH and make it lose energy, and it has been shown that BBHs in low-dispersion galaxies or in highly flattened or triaxial galaxies have relatively low evolution timescales (Yu 2002). Over-simplified treatments on the interaction of a BBH with its environments may lead to some uncertainty in the current estimation of the strength of the GW radiation emitted by the BBHs, as the interactions affect how many BBHs are surviving at a given separation, and when and where gravitational radiation becomes dominant in making a BBH lose energy; and a realistic treatment of the BBH interaction with their environments is necessary for the BBH dynamical evolution models and the GW radiation estimation (Shannon et al. 2015; Arzoumanian et al. 2016; Lentati et al. 2015). To obtain

the coalescence rate of merging BBHs in the realistic universe and the realistic statistical distribution of surviving BBHs, in this work we model the dependence of the BBH dynamical evolution on stellar distributions and galaxy shapes, and we incorporate the BBH dynamical evolution model with the realistic distributions of galaxy properties (e.g., stellar distributions, galaxy shapes, galaxy merger rates).

This paper is organized as follows. In Section 2, we review the dynamical processes and the model for the evolution of a BBH in gas-poor systems. The detailed model is mainly adopted from Yu (2002). In Section 3, we describe the modeling of the distribution of surviving BBHs, BBH coalescence rates, and the strength of stochastic GWB. In Section 4, we describe the galaxy samples, the realistic galaxy distributions and the galaxy merger rates used in the model. In Section 5, we present our results for the distribution of surviving BBHs and the GW strength radiated by merging BBHs. Discussion is given in Section 6 and conclusions are given in Section 7.

2. ORBITAL EVOLUTION OF BBHS

In a gas-poor galaxy merger, the formation and evolution of a BBH can be divided into the following stages, according to the dominant physical mechanisms that act to drain the energy of the orbit of two BHs (Begelman et al. 1980; Yu 2002). The relative importance of each mechanism is determined by the spatial scale of the separation between the two BHs. (1) Dynamical friction stage: after two galaxies merge, each BH in its progenitor galaxy will sink into the center of the common potential well of the merging galaxy, due to dynamical friction, from a separation of several tens of kpc to ~ 10 pc. (2) Non-hard binary stage: the two BHs with masses M_1 and M_2 ($M_2 \leq M_1$) form a bound system with semi-major axis

$$a \lesssim R_{\text{inff}} \equiv \frac{GM_{\text{BH}}}{\sigma_c^2} \simeq 10 \left(\frac{M_{\text{BH}}}{10^8 M_\odot} \right) \left(\frac{\sigma_c}{200 \text{ km s}^{-1}} \right)^{-2} \text{ pc}, \quad (1)$$

where $M_{\text{BH}} = M_1 + M_2$, σ_c is the one-dimensional velocity dispersion of the merged galaxy core. The dynamical friction continues to make the BBH lose energy but becomes less and less effective as the binary orbital velocity increases and its orbital period decreases. Meanwhile, from time to time a star walks to the vicinity of the BBH and the three-body interactions between the BBH and the stars gradually become the dominant mechanism to make the BBH lose energy. This stage is an intermediate stage between the previous dynamical friction stage and the next hard binary stage. (3) Hard binary stage: the BBH becomes hard when its semi-major axis

$$a \lesssim a_{\text{h}} \equiv \frac{GM_2}{4\sigma_c^2} \simeq 2.8 \left(\frac{M_2}{10^8 M_\odot} \right) \left(\frac{\sigma_c}{200 \text{ km s}^{-1}} \right)^{-2} \text{ pc}. \quad (2)$$

A hard binary loses energy mainly by interacting with stars passing in their vicinity, most of which will be expelled from the BBH with an energy gain after one or more encounters with it. In such expulsions, the relative

change in the BBH orbital energy is independent of the energy (Heggie 1975), which can simplify the analysis of the BBH evolution timescale at this stage. (4) Gravitational radiation stage: when the semimajor axis of the BBH is small enough (e.g., $< 10^{-2}$ pc), gravitational radiation becomes the dominant effect to drive the BBH orbital decay. This stage is likely to occur before the BBH becomes hard if $M_2 \ll M_1$.

In this paper, we obtain the orbital evolution of a BBH by following the model presented in Yu (2002), supplemented with a numerical method to calculate the stellar orbital motion and obtain the stars that can move to the vicinity the BBH in triaxial gravitational potentials. We summarize the model of the evolution timescales of the BBH at the four stages in Section 2.1-2.4, respectively. Note that the evolution of the BBHs at the non-hard and the hard stages is critical to determine how the BBHs are distributed at pc and sub-pc scales, and when and where the gravitational stages start. One essential factor to determine the BBH evolution timescales in those stages is how many stars on low-angular momentum orbits, which can pass through the vicinity of the BBH, are available to interact strongly with the BBH. Even if the low-angular momentum stars initially in the stellar system are expelled away by interactions with the BBH, the stars on high-angular momentum orbits can still move onto low-angular momentum orbits by the two-body relaxation or by orbital precession in non-spherical (e.g., flattened or triaxial) gravitational potentials (Magorrian & Tremaine 1999; Yu 2002; Berczik et al. 2006; Khan et al. 2011; Preto et al. 2011; Khan et al. 2013; Vasiliev et al. 2015). In this work, we include the effect of the non-spherical potentials, as well as that of the two-body relaxation. We define a “loss region” by the (specific energy, specific angular momentum) phase space of the stars that can precess onto low-angular momentum orbits with pericenter distances $\sim a$. The stars in the loss region can pass by the BBH vicinity and then escape from the BBH after strong interactions with it. We obtain the loss region by numerical simulations, and the method is described in Section 2.5.

In the model, we assume that the BHs are on nearly circular orbits and ignore their eccentricity evolution at the least for the following reasons. (1) At the dynamical friction stage, the orbital decay of a star cluster or a secondary BH generally does not result in a highly eccentric orbit when the two BHs become bound (Polnarev & Rees 1994). (2) If the BBH eccentricity when the two BHs become bound is small (e.g., $\lesssim 0.3$), Quinlan (1996) shows that the BBH eccentricity hardly grows as the BBH hardens. (3) The BBH eccentricity decays quickly at the gravitational radiation stage (Peters & Mathews 1963; Baker 2006). (4) In kinematically anisotropic spherical systems with stars mostly counter-rotating with the BBH orbit, some simulations show that the BBH eccentricity could increase significantly (Amaro-Seoane et al. 2010; Sesana et al. 2011; Holley-Bockelmann & Khan 2015), however it is expected that the significant increase in BBH eccentricity can be decreased or erased if the systems are triaxial, by applying the same reasoning as for the alignment-erasing effect obtained in Cui & Yu (2014). (5) Evolution of triple or multiple BHs can result in BBHs with extreme eccentricity; however, the contribution of those cases to the stochastic GWB at the PTA bands is shown

to be insignificant (see the left panel of Fig. 4 in [Bonetti et al. 2018](#)). (6) It was suggested that a significant fraction of BBHs should have extreme eccentricities close to 1 so that the strength of gravitational waves radiated by mergers of those BBHs can be relatively low (e.g., see Fig. 1 in [Chen et al. 2016](#)), in order to relieve the tension between the non-detection of the stochastic GWBs and the model expectation. According to the results of this work below, the assumption of BBHs with extreme eccentricities are not necessarily required. In addition, exploration on detection prospects for individual BBH sources specifically with extreme eccentricities formed in special conditions are beyond the scope of this work.

In the model, the evolution of the BBH orbital semi-major axis is described by $a(t)$ or $a(\tau)$, where a is the orbital semi-major axis of the BBH or the separation of the two BHs (if they are not bound, yet), t is the cosmic time, and $\tau \equiv t - t'$ is the period since an event at cosmic time t' (e.g, galaxy merger). The BBH evolution timescale at a given a is defined by

$$t_{\text{evol}} \equiv |a/\dot{a}|, \quad (3)$$

where $\dot{a} \equiv da/dt = da/d\tau$.

At the dynamical friction stage, \dot{a} comes mainly from the contribution of dynamical friction, and we denote the corresponding evolution timescale by the dynamical friction timescale t_{df} . After the BBH becomes bound, if we only include the contribution of gravitation radiation to \dot{a} , the corresponding evolution timescale is denoted by t_{gr} (see Eq. 11 below); and if we only include the contribution of the BBH interaction with stars to \dot{a} , the corresponding evolution timescale is denoted by the BBH hardening timescale t_{h} . We obtain the BBH evolution timescale after the BBH becomes bound by

$$t_{\text{evol}} = (t_{\text{h}}^{-1} + t_{\text{gr}}^{-1})^{-1}. \quad (4)$$

We have $t_{\text{evol}} \simeq t_{\text{h}}$ at the non-hard and the hard stages and $t_{\text{evol}} \simeq t_{\text{gr}}$ at the gravitational radiation stage.

2.1. Dynamical friction stage

In the dynamical friction stage, each of the BHs sinks into the common center of the merger remnant independently. We carry out a simple analysis of the evolution timescale at the dynamical friction stage. Assume that a BH of mass M_1 is located at the center of a spherical galaxy with stellar mass density $\rho(r)$ and one-dimensional velocity dispersion $\sigma(r)$. Suppose that a BH with mass M_2 that used to be at the center of a galaxy is orbiting with a velocity \mathbf{v} and spiraling into the center of the parent galaxy by dynamical friction. Because the in-spiraling BH M_2 is accompanied by the stars bound to it with total mass $M_{2,*}$, dynamical friction brings the two BHs together much more rapidly than if M_2 is naked ([Milosavljević & Merritt 2001](#); [Yu 2002](#)). The dynamical friction exerts on M_2 and its accompanying stars $M_{2,*}$ and decelerate them at a rate given by

$$\begin{aligned} \frac{d\mathbf{v}}{dt} = & \frac{4\pi G^2(M_2 + M_{2,*})\rho(r) \ln \Lambda}{v^3} \\ & \times \left[\text{erf}(X) - \frac{2X}{\sqrt{\pi}} e^{-X^2} \right] \mathbf{v}, \end{aligned} \quad (5)$$

where $v = |\mathbf{v}|$, $X = v/(\sqrt{2}\sigma)$, erf is the error function, and the logarithm of the ratio of the maximum and the minimum impact parameter $\ln \Lambda$ is set to unity.

The mass of the stars bound to the secondary BH M_2 can be estimated as follows. In the potential of the spherical galaxy with central BH M_1 , the stars around the BH M_2 is tidally truncated at the radius

$$r_{\text{t}} \simeq \left[\frac{G(M_2 + M_{2,*})}{4\Omega^2 - \kappa^2} \right]^{1/3} \simeq \left[\frac{GM_{2,*}}{4\Omega^2 - \kappa^2} \right]^{1/3}, \quad (6)$$

$M_{2,*} \gg M_2$

where Ω and κ are the circular frequency and epicycle frequency in the parent galaxy. If the stars surrounding each of the BHs follow a singular isothermal distribution, and their one-dimensional velocity dispersions σ_1 and σ_2 , respectively, we have $\Omega^2 = 2\sigma_1^2/r^2$, $\kappa^2 = 4\sigma_1^2/r^2$ and $M_{2,*} = 2\sigma_2^2 r_{\text{t}}/G$. By applying them into Equation (6), we have $r_{\text{t}} = \frac{\sigma_2}{\sqrt{2}\sigma_1} r$, and the total mass of the stars bound to the BH M_2 is given by

$$M_{2,*}(r) = \frac{2\sigma_2^2 r_{\text{t}}}{G} \simeq \frac{\sqrt{2} r \sigma_2^3}{G \sigma_1}. \quad (7)$$

We follow equations (40)-(42) in [Yu \(2002\)](#) to obtain the BBH evolution timescale at the dynamical friction stage t_{df} .

2.2. Non-hard binary stage

The BBH orbital decay in the non-hard binary stage comes from both dynamical friction from distant stars and three-body interactions between the BBH and the stars passing the BBH vicinity. As done in [Yu \(2002\)](#), we apply the dynamical friction timescale t_{df} to estimate the BBH hardening timescales t_{h} at the non-hard binary stage, because scattering experiments with the restricted three-body approximation basically give a hardening timescale similar to the application of the dynamical friction timescale ([Quinlan 1996](#)).

Stars may gain energy and be removed from the galactic core by interactions with the BBH. Before the BBH becomes bound, the stellar mass removed from the galactic core due to the BH orbit decay can be ignored. During the non-hard binary stage, the depletion of the stars can be significant in some galaxies. Before the BBH becomes hard, if the mass of the initial stellar population in the loss region is not sufficient, the BBH would lose energy mainly by dynamical friction with distant stars (which becomes more and more inefficient as the BBH hardens) and by three-body interactions with the low-angular-momentum stars diffused from high-angular-momentum orbits by two-body relaxation (which will dominate the BBH hardening timescales in the hard binary stage). Thus the BBH hardening timescale should be higher than those estimated from t_{df} and smoothly increase to connect the hardening timescale in the hard binary stage. We use the linear approximation to obtain the BBH hardening timescale at $a_{\text{h}} \leq a \leq a_{\text{dp}}$:

$$\ln[t_{\text{h}}(a)] = \ln[t_{\text{h}}(a_{\text{h}})] + \ln[t_{\text{df}}(a_{\text{dp}})/t_{\text{h}}(a_{\text{h}})] / \ln(a_{\text{dp}}/a_{\text{h}}), \quad (8)$$

where a_{dp} is the semimajor axis where the initial population of stars in the loss region are all removed from the

loss region, t_{df} is obtained from Section 2.1, and $t_{\text{h}}(a_{\text{h}})$ is obtained from Section 2.3.

2.3. Hard binary stage

In the hard binary stage, the orbital decay of a BBH is mainly driven by three-body interactions with low-angular-momentum stars passing its vicinity. The BBH orbital decay timescale is mainly determined by how many stars are available to move onto low-angular-momentum orbits and how fast they can move onto the orbits to strongly interact with the BBH. After such strong interactions, the stars escape with energy gain and are considered to be cleared from the loss region. We denote the orbital binding energy of a star per unit mass by \mathcal{E} . Assuming that $F(\mathcal{E}, a)d\mathcal{E}$ is the number clearing rate from the loss region for stars with energy $\mathcal{E} \rightarrow \mathcal{E} + d\mathcal{E}$ and $\Delta\mathcal{E}$ is the corresponding average change of the specific energy of the stars escaping from the BBH during an interaction with the BBH, the orbital energy loss rate of the BBH is given by

$$\left| \frac{dE}{dt}(a) \right| = -m_* \int \Delta\mathcal{E} F(\mathcal{E}, a) d\mathcal{E}, \quad (9)$$

where $E = -GM_{\text{BH}}\mu_{12}/2a$ is the orbital energy of the BBH, $\mu_{12} = M_1M_2/M_{\text{BH}}$ is the reduced mass of the BBH, m_* is the mass of a single star, and all stars are assumed to have the same mass. The quantity $\Delta\mathcal{E}$ is only weakly dependent on \mathcal{E} for hard binaries. Hence we assume $\Delta\mathcal{E} = -KG\mu_{12}/a$ where K is a constant which is determined from the numerical experiment of [Quinlan \(1996\)](#). Therefore, after the BBH becomes hard, its hardening timescale due to stellar interaction is given by

$$t_{\text{h}}(a) = \left| \frac{a}{\dot{a}} \right| = \left| \frac{E}{\dot{E}} \right| = \frac{M_{\text{BH}}}{2Km_*} \frac{1}{\int F(\mathcal{E}, a) d\mathcal{E}}, \quad (10)$$

where m_* is the mass of a star and is assumed to be a solar mass in this work. We obtain the clearing rate $F(\mathcal{E}, a)$ by following the analysis in section 3.2 in [Yu \(2002\)](#), which is affected by the size of the loss region and the two-body relaxation processes.

2.4. Gravitational radiation stage

In the gravitational radiation stage, the evolution timescale of the BBH is described by

$$t_{\text{gr}}(a, e) = \frac{5}{64} \frac{c^5 a^4 (1 - e^2)^{7/2}}{G^3 \mu_{12} M_{\text{BH}}^2 (1 + 73e^2/24 + 37e^4/96)}, \quad (11)$$

where e is the orbital eccentricity of the binary ([Peters 1964](#)) is set to zero in this work as argued above. The transition from the evolution stages of the BBH interacting with its surrounding environments (the hard binary and non-hard binary stages) to the gravitational radiation stage can be marked by $t_{\text{gr}}(a = a_{\text{gr}}) = t_{\text{h}}(a = a_{\text{gr}})$. At $a = a_{\text{gr}}$, the BBH GW frequency and the orbital period are labeled by f_{gr} and P_{gr} , respectively.

Note that a large eccentricity can not only make the BBH enter the gravitational radiation earlier, but also accelerate the orbital decay, and the gravitational radiation energy spectrum can be correspondingly changed.

2.5. Loss region

The size of the loss region in the phase space depends on galaxy shapes. The loss region in a spherical stellar system is a ‘loss cone’ given by

$$J \leq J_{\text{lc}} \simeq \sqrt{2GM_{\text{BH}}f_a a} \quad (12)$$

(f_a is a dimensionless factor ~ 1). In an axisymmetric or triaxial system, there exist centrophilic orbits such as box orbits, which pass arbitrarily close to the center and have low angular momentum, as well as centrophobic orbits such as loop or tube orbits, which avoid the center and have high angular momentum. We use a characteristic specific angular momentum J_s to mark the transition from centrophilic ($J \lesssim J_s$) to centrophobic ($J \gtrsim J_s$) orbits. The loss region in an axisymmetric system can be approximated as a ‘loss wedge’ where stars on centrophilic orbits with $|J_z| < J_{\text{lc}}$ can precess into the loss cone, while those on centrophobic orbits with $J > J_{\text{lc}}$ cannot. In a triaxial system, the loss region can be approximated by $J < J_s$ in which most of the stars can precess into the loss cone.

In this work, we obtain $J_s(\mathcal{E})$ by numerically simulating the motion of a star under the combined gravitational potential of a central point mass M_{BH} and the galactic stars (see eq. 7 in [Cui & Yu 2014](#)). The galactic potential is spherical if it can be described in the form $\Phi(r)$ ($r = |\mathbf{r}|$) and triaxial if it can be described in the form $\Phi(x^2 + y^2/\xi^2 + z^2/\zeta^2)$ ($\zeta < \xi < 1$). If the shape distribution of host galaxies is described in mass density, we use the following equation (which is derived for logarithmic potentials) to approximately convert it into the shape distribution in gravitational potentials:

$$q_{\Phi} = \sqrt{\frac{1 + \sqrt{1 + 8q_{\rho}^2}}{4}}, \quad (13)$$

where q_{ρ} represents the medium-to-major or the minor-to-major axis ratio in the density shape, and q_{Φ} represents the corresponding ratio in the potential shape (see Eq. 2.72b in [Binney & Tremaine 2008](#)). If $1 - q_{\rho} \ll 1$, we have $1 - q_{\Phi} \simeq (1 - q_{\rho})/3$.

Noting that it is time-consuming to obtain $J_s(\mathcal{E})$ in a large number of galaxies by numerically tracing the motion of each star in a galaxy for a sufficiently long time to judge whether it can move to the center on a centrophilic orbit, we improve the judging efficiency for a centrophilic orbit and describe the method to obtain J_s below.

In a general triaxial system, for a centrophilic orbit, the motion of the stars can pass arbitrarily close to the center, and the stellar orbital angular momentum will flip its direction during the orbital motion. Numerically we count a star as one in the loss region, if all the three x , y , and z components of its orbital angular momentum flipped their directions. This criterion is effective and efficient enough in practice, although in principle the stars that change the signs of their orbital angular momentum components are not exactly the same population of the stars that can move to the center (on centrophilic orbits). Given the potential of a merger remnant, we obtain the characteristic angular momentum J_s as a function of the binding energy \mathcal{E} . In practice, only stars in a certain range of \mathcal{E} have considerable importance to the three-body interactions with a BBH. We set the boundaries

of \mathcal{E} as $[-\Phi(r_{\max}), -\Phi(r_{\min})]$, where $r_{\min} = 0.1R_{\text{inff}}$ and $r_{\max} = 100R_{\text{inff}}$. For each system, we obtain $J_s(\mathcal{E})$ for 401 values of \mathcal{E} equally spaced within the given range. For each \mathcal{E} , we use the Monte Carlo method to generate 2000 test particles whose squared angular momenta are uniformly distributed in $[0, J_c^2(\mathcal{E})]$ with isotropic velocity distributions, where $J_c(\mathcal{E})$ is the specific angular momentum of a circular orbit at \mathcal{E} . We follow the evolution of these test particles within the potential of the host merger remnant, which is composed of two parts, i.e., the potential from the BBH and the galactic potential from the host galaxy, where the potential of the BBH is simplified as a Keplerian potential around a point mass M_{BH} and the galactic potential is assumed to be triaxial. We calculate the fraction η of the test particles that flipped the signs of all the x , y , and z components of the orbital angular momentum during an evolution time of $160P_c(\mathcal{E})$, where $P_c(\mathcal{E})$ is the period of a circular orbit at energy \mathcal{E} . The characteristic angular momentum $J_s(\mathcal{E})$ is then obtained by $J_s(\mathcal{E}) = \sqrt{\eta(\mathcal{E})J_c^2(\mathcal{E})}$. The above method to obtain $J_s(\mathcal{E})$ is efficient enough.

We have done some tests to show that the above method is effective, although the stars that change the signs of their orbital angular momentum components are not exactly the same population stars that can move to the center and the evolution of the orbital angular momentum of a star is traced with an evolution time of only $160P_c(\mathcal{E})$. The tests are done for the galaxies (with a limited number ~ 800) randomly selected from the mock galaxy sample (with the shape distribution in Padilla & Strauss 2008) presented in Section 4.2. In each galaxy, the motions of 500 stars at a given \mathcal{E} are traced for a sufficiently long time ($8000P_c(\mathcal{E})$), where the two values of $\mathcal{E} = -\Psi(10R_{\text{inff}})$ and $-\Psi(100R_{\text{inff}})$ are tested. Our tests show that the number ratios of the stars that change the signs of their orbital angular momentum components to the stars that can move the center is close to 1 and the extension of the evolution time of a star does not affect our results significantly.

As mentioned above, in a configuration close to being axisymmetric, the loss region is approximated as a loss wedge, and the $J_s(\mathcal{E})$ obtained by the above method may be too low and is not appropriate to be taken as the $J_s(\mathcal{E})$ defined in the loss wedge, as a star is recognized as being in the loss region only if all the three x , y , and z components of its angular momentum flipped their directions during the orbital evolution. We estimate the size of the loss wedge by the following criterion: a star is recognized as being in the loss wedge if at the least one (but not all) of the three x , y , and z components of its angular momentum flipped their directions and the remaining components possess a combined specific angular momentum smaller than J_c (where a is set to $GM_{\text{BH}}/44\sigma_c^2$ in Eq. 12, i.e., the values of a_h with $q_{\text{BH}} = 0.1$). We calculate the fraction η of the stars satisfying the above conditions, and the characteristic angular momentum $J_s(\mathcal{E})$ in the loss wedge is then obtained by $J_s(\mathcal{E}) = \eta(\mathcal{E})J_c^2(\mathcal{E})/(2J_c)$.

Given a shape configuration of a system, we use the above methods to numerically estimate both the size of the loss region by applying the criterion for a general triaxial system and the size of the loss wedge by applying the criterion for an axisymmetric system, and the stars in the loss wedge and in the loss region both contribute

to the stellar reservoir to have strong interactions with the BBH.

In the model, for simplicity, we do not consider the time evolution of galaxy shapes (e.g., rotation of a triaxial system or changes in axis ratios)¹ and the difference of galaxy shapes at different galactic radii.

3. MODELING OF THE DISTRIBUTIONS OF MERGING BBHS AND SURVIVING BBHS

3.1. Distributions of surviving BBHs

We define the distribution of surviving BBHs by $\Phi_{\text{BBH}}(M_{\text{BH}}, q_{\text{BH}}, a, z)$ ($q_{\text{BH}} \leq 1$) so that $\Phi_{\text{BBH}}(M_{\text{BH}}, q_{\text{BH}}, a, z)dM_{\text{BH}}dq_{\text{BH}}da$ is the comoving number density of BBHs at redshift z with total mass in the range $M_{\text{BH}} \rightarrow M_{\text{BH}} + dM_{\text{BH}}$, mass ratio in the range $q_{\text{BH}} \rightarrow q_{\text{BH}} + dq_{\text{BH}}$, and semimajor axis (or separation) in the range $a \rightarrow a + da$.

We define the galaxy stellar mass function (GSMF) by $n_{\text{gal}}(M_{\text{gal}}, z)$ so that $n_{\text{gal}}(M_{\text{gal}}, z)dM_{\text{gal}}$ is the comoving number density of galaxies with mass in the range $M_{\text{gal}} \rightarrow M_{\text{gal}} + dM_{\text{gal}}$ at redshift z . We describe the galaxy merger rate per galaxy at redshift z by $\mathcal{R}_{\text{gal}}(q_{\text{gal}}, z|M_{\text{gal}})$ ($q_{\text{gal}} \leq 1$) so that $\mathcal{R}_{\text{gal}}(q_{\text{gal}}, z|M_{\text{gal}})dq_{\text{gal}}dt$ represents the average number of galaxy mergers with mass ratio in the range $q_{\text{gal}} \rightarrow q_{\text{gal}} + dq_{\text{gal}}$ within time $t \rightarrow t + dt$ for a descendant galaxy with mass M_{gal} , where t is the corresponding cosmic time at redshift z . Similarly as the above definition for galaxies, we also define the corresponding variables for the spheroidal components of merging remnants. (which are also called “bulge” for simplicity and denoted by the subscript $*$ below), i.e., the stellar mass function $n_*(M_*, z)$, the merger rate per spheroidal component $\mathcal{R}_*(q_*, z|M_*)$, and the mass ratio q_* . For major mergers, we assume that galaxy mergers form spheroids characterized by mass $M_* = M_{\text{gal}}$ and merger mass ratio $q_* = q_{\text{gal}}$. For minor mergers, the secondary galaxy is assumed to be accreted onto the spheroidal component of the primary galaxy, and the mass of the spheroidal component of the merging remnant is assumed to be the sum of the stellar masses in the secondary galaxy and in the spheroidal component of the primary galaxy, and the merger mass ratio q_* is their mass ratio.

We connect the BBH distribution function with the

¹ Some possible effects of the changes in axis ratios can be partly inferred from this work done by adopting three different sets of the galaxy triaxial shape distributions and comparing their results. Regarding the rotation of a triaxial system, the characteristic rotating pattern timescale is generally much longer than one orbital period of a star with the relevant energy, but it can be shorter than the timescale of the star on a centrophilic orbit to precess into the loss cone. The assumption of ignoring the shape rotation is plausible and does not affect the above estimate of J_s much if the stellar centrophilic orbits in the triaxial system are mostly stochastic (which generally have relatively large apocenter distances and low \mathcal{E} ; cf. the right panel in Figure 4 of Magorrian & Tremaine 1999). The shape rotation may affect the above estimate of J_s if the precessions of the stellar orbits into the loss cone are regular, which needs a further detailed complement for its statistical effect; nevertheless, an extreme case of fast rotation of a triaxial system would result in the dynamical effects partly close to those in axisymmetric systems, and the effects in axisymmetric systems can be partly seen from the results obtained from one of the three observational galaxy shape distribution adopted in this work (i.e., Weijmans et al. 2014, which prefers the axisymmetric shape configurations).

galaxy merger rate by the following equations:

$$\begin{aligned}
& \Phi_{\text{BBH}}(M_{\text{BH}}, q_{\text{BH}}, a, z) \\
&= \int_0^t dt' \int dM_* \int dq_* n_*(M_*, z') \mathcal{R}_*(q_*, z' | M_*) \\
&\quad \times p_{\text{BH}}(M_{\text{BH}}, q_{\text{BH}} | M_*, q_*, z') \\
&\quad \times p_a(a, t - t' | M_*, q_*, M_{\text{BH}}, q_{\text{BH}}, z') \\
&\quad \times P_{\text{intact}}(z, z' | M_*) \tag{14}
\end{aligned}$$

and

$$\begin{aligned}
& n_*(M_*, z') \mathcal{R}_*(q_*, z' | M_*) \\
&= \int dM_{\text{gal}} \int dq_{\text{gal}} n_{\text{gal}}(M_{\text{gal}}, z') \mathcal{R}_{\text{gal}}(q_{\text{gal}}, z' | M_{\text{gal}}) \\
&\quad \times p_*(M_*, q_* | M_{\text{gal}}, q_{\text{gal}}, z') \tag{15}
\end{aligned}$$

where $p_{\text{BH}}(M_{\text{BH}}, q_{\text{BH}} | M_*, q_*, z')$ is a probability function defined so that $p_{\text{BH}}(M_{\text{BH}}, q_{\text{BH}} | M_*, q_*, z') dM_{\text{BH}} dq_{\text{BH}}$ represents the probability that a galaxy merger characterized by the bulge mass of the merging remnant M_* and mass ratio q_* at redshift z' leads to a BBH with total mass in the range $M_{\text{BH}} \rightarrow M_{\text{BH}} + dM_{\text{BH}}$ and mass ratio in the range $q_{\text{BH}} \rightarrow q_{\text{BH}} + dq_{\text{BH}}$, $p_a(a, \tau | M_*, q_*, M_{\text{BH}}, q_{\text{BH}}, z')$ is a probability function defined so that $p_a(a, \tau | M_*, q_*, M_{\text{BH}}, q_{\text{BH}}, z') da$ represents the probability that the galaxy merger leads to a BBH with semimajor axis in the range $a \rightarrow a + da$ at a time τ after the galaxy merger, $p_*(M_*, q_* | M_{\text{gal}}, q_{\text{gal}}, z')$ is the probability that a galaxy merger with total mass M_{gal} and mass ratio q_{gal} at redshift z' results in the merging remnants characterized by M_* and q_* , and $\int \int p_{\text{BH}}(M_{\text{BH}}, q_{\text{BH}} | M_*, q_*, z') dM_{\text{BH}} dq_{\text{BH}} = 1$, $\int p_a(a, \tau | M_*, q_*, M_{\text{BH}}, q_{\text{BH}}, z') da = 1$, and $\int \int p_*(M_*, q_* | M_{\text{gal}}, q_{\text{gal}}, z') dM_{\text{gal}} dq_{\text{gal}} = 1$. The distributions of p_{BH} and p_* depend on BH demography and galaxy demography, and the distribution of p_a depends on the distribution of the intrinsic structure of galaxies. As to be seen below, the BBH mergers contributing to the GWB comes mainly from redshift $z \lesssim 2$. The distribution of the intrinsic structure of galaxies and BH demography used in this work are mainly based on observations in the nearby universe, and we assume that they are independent of redshift at low redshift $z \lesssim 2$ and then distributions of p_{BH} and p_a are independent of redshift in this work. The function p_a is obtained by assuming that the BBH evolves independently inside the merging galaxy remnant and that no other later galaxy mergers affect the BBH evolution. However, before the BBH reaches the gravitational radiation stage, it is possible that the host merger remnant undergoes a big impact, that is, a major merger with another galaxy or being accreted by another bigger galaxy to become a satellite galaxy in this work; in these cases the interactions of triple or multiple BHs may lead to quick BBH coalescence or BH kicks out of the host merger remnant. The function $P_{\text{intact}}(z, z' | M_*)$ ($z < z'$) is introduced in Equation (14) to represent the probability that the host merger remnant M_* does not experience such big impacts from redshift z' to z . The detailed method to obtain $P_{\text{intact}}(z, z' | M_*)$ is described in Section 3.4. In this work, the effects of the

big impacts (e.g., on the surviving BBH distributions, BBH coalescence rates, GWBs; see also Eqs. 21 and 31 below) are included by removing a corresponding BBH system from consideration if it experiences a big impact during its evolution, and we neglect the contribution from possibly newly formed BBHs caused by triple or multiple BH interactions.

As to be shown below, we use Monte-Carlo simulations to generate galaxy mergers and calculate the BBH evolution in the galaxy mergers. Suppose that we have N galaxy mergers with parameters (M_*, q_*) leading to the formation of BBHs with parameters $(M_{\text{BH}}, q_{\text{BH}})$ and semimajor axis $a_{i|M_*, q_*, M_{\text{BH}}, q_{\text{BH}}}(\tau)$ ($i = 1, 2, \dots, N$) at a time τ after the galaxy mergers. The probability function $p_a(a, \tau | M_*, q_*, M_{\text{BH}}, q_{\text{BH}})$ can be obtained by

$$\begin{aligned}
& p_a(a, \tau | M_*, q_*, M_{\text{BH}}, q_{\text{BH}}) \\
&= \frac{1}{N} \sum_{i=1}^N \delta[a - a_{i|M_*, q_*, M_{\text{BH}}, q_{\text{BH}}}(\tau)]. \tag{16}
\end{aligned}$$

By applying Equation (16) into Equation (14), we have

$$\begin{aligned}
& \Phi_{\text{BBH}}(M_{\text{BH}}, q_{\text{BH}}, a, z) \\
&= \frac{1}{N} \sum_{i=1}^N \int dM_* \int dq_* n_*(M_*, z_i) \mathcal{R}_*(q_*, z_i | M_*) \\
&\quad \times p_{\text{BH}}(M_{\text{BH}}, q_{\text{BH}} | M_*, q_*, z_i) H(t - \tau_{a,i}) \frac{t_{\text{evol},i}}{a} \\
&\quad \times P_{\text{intact}}(z, z_i | M_*), \tag{17}
\end{aligned}$$

where

$$t_{\text{evol},i} = a \left| \frac{da_{i|M_*, q_*, M_{\text{BH}}, q_{\text{BH}}}}{d\tau} \right|_{\tau=\tau_{a,i}|M_*, q_*, M_{\text{BH}}, q_{\text{BH}}}^{-1}, \tag{18}$$

is the BBH evolution timescale at a (see Eq. 3), $\tau_{a,i|M_*, q_*, M_{\text{BH}}, q_{\text{BH}}}$ is the solution of equation $a_{i|M_*, q_*, M_{\text{BH}}, q_{\text{BH}}}(\tau) = a$, $H(t - \tau_{a,i})$ is a step function defined by $H(t - \tau_{a,i}) = 1$ if $t > \tau_{a,i}$ and $H(t - \tau_{a,i}) = 0$ if $t \leq \tau_{a,i}$, and z_i is the corresponding redshift of cosmic time $t - \tau_{a,i}$.

In a simplified or extreme case, if $p_{\text{BH}}(M_{\text{BH}}, q_{\text{BH}} | M_*, q_*, z) = \delta(M_{\text{BH}} - A \cdot M_*) \delta(q_{\text{BH}} - q_*)$ with A being a constant, and the BBH evolution $a_i(\tau)$ ($i = 1, \dots, N$) is the same for the same (M_*, q_*) , Equation (17) is simplified as

$$\begin{aligned}
& \Phi_{\text{BBH}}(M_{\text{BH}}, q_{\text{BH}}, a, z(t)) \\
&= A^{-1} H(t - \tau_a) a^{-1} t_{\text{evol}} \cdot n_*(M_* = A^{-1} M_{\text{BH}}, z(t - \tau_a)) \\
&\quad \times \mathcal{R}_*(q_* = q_{\text{BH}}, z(t - \tau_a) | M_* = A^{-1} M_{\text{BH}}) \\
&\quad \times P_{\text{intact}}(z(t), z(t - \tau_a) | M_* = A^{-1} M_{\text{BH}}). \tag{19}
\end{aligned}$$

3.2. BBH coalescence rates

We define the BBH coalescence rate $R_{\text{BH}}(M_{\text{BH}}, q_{\text{BH}}, z)$ so that $R_{\text{BH}}(M_{\text{BH}}, q_{\text{BH}}, z) dM_{\text{BH}} dq_{\text{BH}} dt$ represents the comoving number density of the BBH coalescence events occurring during cosmic time $t \rightarrow t + dt$ and with the total mass of the two coalescing BHs in the range $M_{\text{BH}} \rightarrow M_{\text{BH}} + dM_{\text{BH}}$ and their mass ratio in the range $q_{\text{BH}} \rightarrow q_{\text{BH}} + dq_{\text{BH}}$. The BBH coalescence rate can be

obtained by

$$\begin{aligned}
 & R_{\text{BH}}(M_{\text{BH}}, q_{\text{BH}}, z(t)) \\
 &= \frac{d}{dt} \left[\int_0^t dt' \int dM_* \int dq_* n_*(M_*, z') \mathcal{R}_*(q_*, z' | M_*) \right. \\
 & \quad \times p_{\text{BH}}(M_{\text{BH}}, q_{\text{BH}} | M_*, q_*, z') \\
 & \quad \left. \times f_{\text{coal}}(t - t' | M_*, q_*, M_{\text{BH}}, q_{\text{BH}}, z') \right], \quad (20)
 \end{aligned}$$

where $f_{\text{coal}}(\tau | M_*, q_*, M_{\text{BH}}, q_{\text{BH}}, z')$ represents the fraction of the BBHs that can coalesce before cosmic time $t' + \tau$ among those BBHs with parameters $(M_{\text{BH}}, q_{\text{BH}})$ caused by galaxy mergers with parameters (M_*, q_*) occurring at redshift z' . The fraction of f_{coal} can be obtained by

$$\begin{aligned}
 & f_{\text{coal}}(\tau | M_*, q_*, M_{\text{BH}}, q_{\text{BH}}, z') \\
 &= \frac{1}{N} \sum_{i=1}^N \left[H(\tau - \tau_{a=0,i} | M_*, q_*, M_{\text{BH}}, q_{\text{BH}}) \right. \\
 & \quad \left. \times P_{\text{intact}}(z(t' + \tau_{a=0,i} | M_*, q_*, M_{\text{BH}}, q_{\text{BH}}), z' | M_*) \right], \quad (21)
 \end{aligned}$$

where the term P_{intact} removes the contribution of a BBH system if it experiences a big impact before its expected coalescence time $t' + \tau_{a=0}$ obtained by assuming it evolves independently.

Applying Equation (21) into Equation (20) gives

$$\begin{aligned}
 & R_{\text{BH}}(M_{\text{BH}}, q_{\text{BH}}, z(t)) \\
 &= \frac{1}{N} \sum_{i=1}^N \int dM_* \int dq_* n_*(M_*, z_i) \mathcal{R}_*(q_*, z_i | M_*) \\
 & \quad \times p_{\text{BH}}(M_{\text{BH}}, q_{\text{BH}} | M_*, q_*, z_i) H(t - \tau_{a=0,i}) \\
 & \quad \times P_{\text{intact}}(z(t), z_i | M_*), \quad (22)
 \end{aligned}$$

where z_i is the redshift at cosmic time $t - \tau_{a=0,i}$.

In the extreme case used for Equation (19), if $\tau_{a=0} < t$, Equation (22) is simplified as

$$\begin{aligned}
 & R_{\text{BH}}(M_{\text{BH}}, q_{\text{BH}}, z(t)) \\
 &= A^{-1} n_*(M_* = A^{-1} M_{\text{BH}}, z(t - \tau_{a=0})) \\
 & \quad \times \mathcal{R}_*(q_* = q_{\text{BH}}, z(t - \tau_{a=0}) | M_* = A^{-1} M_{\text{BH}}) \\
 & \quad \times P_{\text{intact}}(z(t), z(t - \tau_{a=0}) | M_* = A^{-1} M_{\text{BH}}). \quad (23)
 \end{aligned}$$

The above equation can be further simplified in the following two cases.

- For sufficiently small a , the difference of n_{gal} and \mathcal{R}_{gal} (or n_* and \mathcal{R}_*) at different redshifts $z(t - \tau_a)$ and $z(t - \tau_{a=0})$ is negligible, and applying Equation (23) into Equation (19) gives

$$\Phi_{\text{BBH}}(M_{\text{BH}}, q_{\text{BH}}, a, z) = R_{\text{BH}}(M_{\text{BH}}, q_{\text{BH}}, z) |da/dt|. \quad (24)$$

- If the BBH coalescence occurs immediately after a galaxy merger (i.e., $\tau_a \sim 0$), Equation (23) is simplified as

$$\begin{aligned}
 & R_{\text{BH}}(M_{\text{BH}}, q_{\text{BH}}, z) \\
 & \simeq A^{-1} n_*(M_* = A^{-1} M_{\text{BH}}, z) \\
 & \quad \times \mathcal{R}_*(q_* = q_{\text{BH}}, z | M_* = A^{-1} M_{\text{BH}}), \quad (25)
 \end{aligned}$$

and the BBH coalescence rate can be approximately obtained from the galaxy merger rate at the same redshift.

3.3. Stochastic gravitational-wave background

We denote the total present-day energy density in gravitational radiation by \mathcal{E}_{gw} , which can be expressed by

$$\mathcal{E}_{\text{gw}} \equiv \int \frac{\pi}{4} \frac{c^2}{G} f^2 h_c^2(f) d \ln f, \quad (26)$$

where c is the speed of light, G is the gravitational constant, f is the frequency of gravitational waves observed today on earth, and h_c is the characteristic strain amplitude of the GW spectrum over a logarithmic frequency interval (Phinney 2001).

The present-day GW energy density can be obtained by an integration over the contribution from the GW radiation sources (BBHs in this work) in the cosmic history as follows,

$$\begin{aligned}
 \mathcal{E}_{\text{gw}} &= \int dz dM_{\text{BH}} dq_{\text{BH}} da \left| \frac{dt}{dz} \right| \\
 & \quad \times \Phi_{\text{BBH}}(M_{\text{BH}}, q_{\text{BH}}, a, z) \cdot \frac{1}{1+z} \cdot \left| \frac{E}{t_{\text{gr}}} \right| \quad (27)
 \end{aligned}$$

where f_{r} is the frequency of the GW signal in the source's cosmic rest frame and is related with f through $f_{\text{r}} = f(1+z)$, $\left| \frac{E}{t_{\text{gr}}} \right|$ is the GW energy per unit time radiated by an in-spiraling BBH with parameters $(M_{\text{BH}}, q_{\text{BH}}, a)$ (see the definition of t_{gr} in Eq. 11), and the term $\frac{1}{1+z}$ accounts for the redshift of the GWs since emission.

During the in-spiral, the frequency of the GW signal is twice the Keplerian orbital frequency of the BBH and increases monotonically till the final coalescence and can be estimated by

$$f \simeq 3.4 \times 10^{-9} \left(\frac{M_{\text{BH}}}{10^8 M_{\odot}} \right)^{1/2} \left(\frac{a}{10^{-2} \text{ pc}} \right)^{-3/2} \text{ Hz}. \quad (28)$$

The upper limit of f when the circular in-spiral assumption in Equation (32) is valid can be roughly estimated by twice of the Keplerian orbital frequency at the innermost stable circular orbit (ISCO) for a Schwarzschild BH with mass the same as the total mass of the BBH, that is,

$$f \simeq f_{\text{ISCO}} \simeq 2.2 \times 10^{-5} \left(\frac{M_{\text{BH}}}{10^8 M_{\odot}} \right)^{-1} \text{ Hz}. \quad (29)$$

The above upper limit for BBHs is safely outside the frequency band probed by PTAs.

From Equations (26)-(27) and (17), we can estimate the overall strain amplitude of the expected stochastic

GWB from BBHs by

$$\begin{aligned}
& \frac{\pi}{4} \frac{c^2}{G} f^2 h_c^2(f) \\
&= \int dz dM_{\text{BH}} dq_{\text{BH}} \left| \frac{dt}{dz} \right| \cdot \Phi_{\text{BBH}}(M_{\text{BH}}, q_{\text{BH}}, a, z) \\
& \quad \times \left| \frac{da}{d \ln f_r} \right| \cdot \frac{1}{1+z} \cdot \left| \frac{E}{t_{\text{gr}}} \right| \quad (30) \\
&= \int dz dM_{\text{BH}} dq_{\text{BH}} \left| \frac{dt}{dz} \right| \\
& \quad \times \frac{1}{N} \sum_{i=1}^N \int dM_* \int dq_* n_*(M_*, z_i) \mathcal{R}_*(q_*, z_i | M_*) \\
& \quad \times p_{\text{BH}}(M_{\text{BH}}, q_{\text{BH}} | M_*, q_*, z_i) H(t - \tau_{a,i}) \\
& \quad \times P_{\text{intact}}(z, z_i | M_*) \\
& \quad \times \frac{(\pi G)^{2/3}}{3} \mathcal{M}^{5/3} f^{2/3} (1+z)^{-1/3} \cdot \frac{t_{\text{evol},i}}{t_{\text{gr}}} \quad (31)
\end{aligned}$$

where z_i is the corresponding redshift of cosmic time $t - \tau_{a,i}$, \mathcal{M} is the chirp mass of the BBH defined by $\mathcal{M}^{5/3} \equiv M_1 M_2 (M_1 + M_2)^{-1/3}$, $t_{\text{evol},i}^{-1} = t_{\text{h},i}^{-1} + t_{\text{gr}}^{-1}$, and

$$\left| \frac{E}{a} \cdot \frac{da}{d \ln f_r} \right| = \left| \frac{dE}{d \ln f_r} \right| = \frac{(\pi G)^{2/3}}{3} \mathcal{M}^{5/3} f_r^{2/3} \quad (32)$$

is used.

For sufficiently high f , the difference of n_{gal} and \mathcal{R}_{gal} (or n_* and \mathcal{R}_*) at different redshifts $z(t - \tau_a)$ and $z(t - \tau_{a=0})$ is negligible; and in this case, applying Equation (22) into Equation (31) gives

$$\begin{aligned}
& \frac{\pi}{4} \frac{c^2}{G} f^2 h_c^2(f) \\
& \simeq \int dz dM_{\text{BH}} dq_{\text{BH}} \left| \frac{dt}{dz} \right| R_{\text{BH}}(M_{\text{BH}}, q_{\text{BH}}, z) \\
& \quad \times \frac{(\pi G)^{2/3}}{3} \mathcal{M}^{5/3} f^{2/3} (1+z)^{-1/3} \cdot \left\langle \frac{t_{\text{evol},i}}{t_{\text{gr}}} \right\rangle. \quad (33)
\end{aligned}$$

where

$$\begin{aligned}
& \left\langle \frac{t_{\text{evol},i}}{t_{\text{gr}}} \right\rangle \\
& \equiv \frac{1}{N} \sum_{i=1}^N \int dM_* \int dq_* n_*(M_*, z_i) \mathcal{R}_*(q_*, z_i | M_*) \\
& \quad \times p_{\text{BH}}(M_{\text{BH}}, q_{\text{BH}} | M_*, q_*, z_i) H(t - \tau_{a,i}) \cdot \frac{t_{\text{evol},i}}{t_{\text{gr}}} \\
& \quad \times R_{\text{BH}}^{-1}(M_{\text{BH}}, q_{\text{BH}}, z). \quad (34)
\end{aligned}$$

If $t_{\text{gr}} \ll t_{\text{h},i}$ ($i = 1, 2, \dots, N$), we have $t_{\text{evol},i}/t_{\text{gr}} \simeq 1$, $\langle t_{\text{evol},i}/t_{\text{gr}} \rangle \simeq 1$, and $h_c \propto f^{-2/3}$; and if $t_{\text{gr}} \gg t_{\text{h},i}$ and $t_{\text{h},i} \propto a^{\alpha_a}$ (where the power law α_a is a constant, $i = 1, 2, \dots, N$), we have $\langle t_{\text{evol},i}/t_{\text{gr}} \rangle \propto f^{2(4-\alpha_a)/3}$ and $h_c \propto f^{\alpha_h}$ with $\alpha_h = (2 - \alpha_a)/3$.

3.4. Multiple galaxy mergers during the evolution of a BBH

In this subsection, we present a rough way on how to obtain the function $P_{\text{intact}}(z, z' | M_*)$ shown in Equation

(14), the probability that the host merger remnant M_* does not experience big impacts (including major mergers with other galaxies and mergers with bigger galaxies) from redshift z' to z .

We define the progenitor galaxy merger rate per galaxy at redshift z by $\mathcal{R}_{\text{prog}}(M_{\text{gal},2}, z | M_{\text{gal},1})$ so that $\mathcal{R}_{\text{prog}}(M_{\text{gal},2}, z | M_{\text{gal},1}) dM_{\text{gal},2} dt$ represents the average number of mergers of a galaxy with mass $M_{\text{gal},1}$ undergoing with a second galaxy with mass within $M_{\text{gal},2} \rightarrow M_{\text{gal},2} + dM_{\text{gal},2}$ during time $t \rightarrow t + dt$. We define $\mu_{\text{gal}} \equiv M_{\text{gal},2}/M_{\text{gal},1}$, and thus $q_{\text{gal}}(\leq 1) = \min(\mu_{\text{gal}}, 1/\mu_{\text{gal}})$. The function $\mathcal{R}_{\text{prog}}(M_{\text{gal},2}, z | M_{\text{gal},1})$ can be obtained from the GSMF $n_{\text{gal}}(M_{\text{gal}}, z)$ and the descendant galaxy merger rate $\mathcal{R}_{\text{gal}}(q_{\text{gal}}, z | M_{\text{gal}})$ (see their definitions in Section 3.1) through the following equation on the number of the galaxy merger events per unit comoving volume:

$$\begin{aligned}
& \mathcal{R}_{\text{prog}}(M_{\text{gal},2}, z | M_{\text{gal},1}) dM_{\text{gal},2} dt \cdot n_{\text{gal}}(M_{\text{gal},1}, z) dM_{\text{gal},1} \\
&= \frac{1}{2} \mathcal{R}_{\text{gal}}(q_{\text{gal}}, z | M_{\text{gal}}) dq_{\text{gal}} dt \cdot n_{\text{gal}}(M_{\text{gal}}, z) dM_{\text{gal}}, \quad (35)
\end{aligned}$$

where $M_{\text{gal}} = M_{\text{gal},1} + M_{\text{gal},2}$, and the factor of 1/2 accounts for the symmetry between $M_{\text{gal},1}$ and $M_{\text{gal},2}$ in the definition of the progenitor merger rate; and thus we have

$$\begin{aligned}
& \mathcal{R}_{\text{prog}}(M_{\text{gal},2}, z | M_{\text{gal},1}) \\
&= \frac{1}{2} \frac{n_{\text{gal}}(M_{\text{gal}}, z)}{n_{\text{gal}}(M_{\text{gal},1}, z)} \mathcal{R}_{\text{gal}}(q_{\text{gal}}, z | M_{\text{gal}}) \left| \frac{\partial(M_{\text{gal}}, q_{\text{gal}})}{\partial(M_{\text{gal},1}, M_{\text{gal},2})} \right|, \quad (36)
\end{aligned}$$

where $|\partial(M_{\text{gal}}, q_{\text{gal}})/\partial(M_{\text{gal},1}, M_{\text{gal},2})| = (1 + q_{\text{gal}})^2/M_{\text{gal}}$. The average number of big impacts that a host merger remnant with mass $M_{\text{gal},1}$ is expected to go through between redshifts z and z' ($z' > z$) is given by

$$\begin{aligned}
\mathcal{I}(z, z' | M_{\text{gal},1}) &= \int_z^{z'} \int_{q_{\text{major}}}^{\infty} \mathcal{R}_{\text{prog}}(M_{\text{gal},2}, z'' | M_{\text{gal},1}) \\
& \quad \times \left| \frac{dM_{\text{gal},2}}{d\mu_{\text{gal}}} \right| \cdot \left| \frac{dt(z'')}{dz''} \right| d\mu_{\text{gal}} dz'', \quad (37)
\end{aligned}$$

where q_{major} is the lower limit of the mass ratios for major mergers, and $|dM_{\text{gal},2}/d\mu_{\text{gal}}| = M_{\text{gal},1}$. The probability that the host merger remnant keeps intact between redshifts z and z' , $P_{\text{intact}}(z, z' | M_{\text{gal},1})$ can be given by

$$\begin{aligned}
& P_{\text{intact}}(z, z' | M_{\text{gal},1}) \\
&= [1 - \mathcal{I}(z, z' | M_{\text{gal},1})] H(1 - \mathcal{I}(z, z' | M_{\text{gal},1})), \quad (38)
\end{aligned}$$

which is reduced to 1 if $\mathcal{I}(z, z' | M_{\text{gal},1}) = 0$ and 0 if $\mathcal{I}(z, z' | M_{\text{gal},1}) > 1$.

For major mergers of galaxies, whose merging remnants are spheroids, the term $P_{\text{intact}}(z, z' | M_*)$ in Equation (14) can be obtained by replacing $M_{\text{gal},1}$ directly with M_* in the function $P_{\text{intact}}(z, z' | M_{\text{gal},1})$ obtained in Equation (14). For minor mergers of galaxies, we also do this replacement, which is a rough approximation and deserves further improvements.

4. GALAXY DISTRIBUTIONS, SMBH DEMOGRAPHY, AND GALAXY MERGER RATES

In this section, we present the galaxy samples, the realistic galaxy distributions, the galaxy merger rates, and the BH-host galaxy relations used in the model. We also describe the BBH evolution tracks obtained with those distributions.

We generally use a Λ CDM cosmology model with parameters $\Omega_m = 0.307$, $\Omega_\Lambda = 0.693$, $h = 0.678$, $\sigma_8 = 0.823$, and $n_S = 0.96$ (Planck Collaboration et al. 2016). The results of some previous works adopted by our model may have some differences in their used cosmological models. For example, the GSMF adopted from Behroozi et al. (2019) is obtained with a cosmology model with parameters as mentioned above, and the galaxy merger rates adopted from Rodriguez-Gomez et al. (2015) is obtained with a cosmology model with parameters $\Omega_m = 0.2726$, $\Omega_\Lambda = 0.7274$, $h = 0.704$, $\sigma_8 = 0.809$, and $n_S = 0.963$ (Hinshaw et al. 2013). In this work, it is plausible to assume the differences in our conclusions caused by the different versions of the cosmological models are negligible. We use the results from the previous works directly without doing conversion between the different cosmological models, except that they are converted to the values with $h = 0.678$.

4.1. Observational galaxy surface brightness and triaxial shape distributions

To model the dynamics of BBHs inside galaxy merger remnants, the stellar density distributions of the host remnants are needed. To construct a sample of host galaxy merger remnants with a realistic stellar distribution, we use the early-type galaxies obtained in the ATLAS^{3D} survey (Cappellari et al. 2011) and in Lauer et al. (2007a), both of which have high spatial resolution *HST* (Hubble Space Telescope) imaging to detect the inner part of the stellar surface brightness distributions, as described in Section 4.1.1. Regarding the intrinsic triaxial shape distributions of galaxies, we use the observational results summarized from the ATLAS^{3D} survey and the Sloan Digital Sky Survey (SDSS), as described in Section 4.1.2.

4.1.1. Observational galaxy surface brightness distributions

The ATLAS^{3D} survey is based on a volume-limited sample of nearby ($\lesssim 42$ Mpc) early-type galaxies, with multi-band imaging as well as two-dimensional bulk kinematic information as derived from the optical integral-field spectroscopy. Among these early-type galaxies, 135 were found to have *HST* archive data (Krajinović et al. 2013). In the compilation of Krajinović et al. (2013), 13 galaxies show strong dust features in the nuclei and are thus excluded from the analysis. The surface brightness of the remaining 122 galaxies, which are observed by *HST* surveys are all converted to the F555W band (broad-band V), in order to make comparison with previous studies. The “Nuker law” profile (Lauer et al. 1995) is used to fit the surface brightness of these galaxies, i.e.,

$$I(R) = 2^{\frac{\beta-\gamma}{\alpha}} I_b \left(\frac{R}{R_b} \right)^{-\gamma} \left[1 + \left(\frac{R}{R_b} \right)^\alpha \right]^{\frac{\gamma-\beta}{\alpha}}, \quad (39)$$

where I_b is the surface brightness at the break radius R_b , γ and β are the asymptotic inner and outer slopes of the surface brightness profile, respectively, and α parameterizes the sharpness of the break. Cappellari et al. (2013)

provides the mass-to-light ratio M/L in the r band for the ATLAS^{3D} galaxies, which is obtained by the best-fitting self-consistent Jeans Anisotropic Multi-Gaussian Expansion model. Note that the five Nuker-law parameters are obtained in the V band, whereas the above mass-to-light ratios are obtained in the SDSS r band. We convert the M/L from the r band to the V band as follows, based on the magnitude differences in the two bands. Cappellari et al. (2013) provides the total SDSS r -band luminosities for these galaxies. Among the 122 ATLAS^{3D} galaxies adopted in our study, 53 have the V -band apparent magnitudes and all of them have the B -band apparent magnitudes. For the 66 galaxies without the V -band magnitudes but with the SDSS *ugriz* ones, we convert their B -band apparent magnitudes to the V -band ones, based on one empirical equation, $B - V = 0.90(g - r) + 0.21$ listed in <http://www.sdss3.org/dr8/algorithms/sdssUBVRITransform.php> (see also Jester et al. 2005). For the remaining 3 galaxies without the V -band and the SDSS g - and r -band magnitudes, we do the conversion by $B - V = 0.95$ (e.g., Lauer et al. 2007a). The absolute magnitudes M_V can be converted from their apparent magnitudes, given the distances and the extinctions of these galaxies (listed in Table 3 of Cappellari et al. 2011), by assuming the extinction ratio $A_B/A_V = 1.324$ (Table 3.21 in Binney & Merrifield 1998).

Lauer et al. (2007a) provide the “Nuker law” parameters R_b , μ_b , α , β , and γ together with some other parameters for a sample of 219 galaxies, which are compiled from several *HST* investigations of the central structure of early-type galaxies. The mass-to-light ratio of these galaxies can be estimated according to the following empirical galaxy scaling relation in the V -band (Magorrian et al. 1998):

$$\frac{(M/L)_V}{(M/L)_\odot} = 4.9 \left(\frac{L_V}{10^{10} L_\odot} \right)^{0.18}, \quad (40)$$

where L_V is the galaxy luminosity in the V -band.

In Figure 1, we show the ATLAS^{3D} galaxy sample (blue) and the Lauer et al. (2007a) sample (red) in the six-dimensional parameter space composed of the five “Nuker law” parameters (i.e., break radius R_b , surface brightness at break radius μ_b , α , β , γ) and the mass-to-light ratio M/L in the V band. In the figure, the mass-to-light ratios of the Lauer et al. (2007a) sample are estimated by Equation (40). There are 61 common galaxies in the two samples, and the fit parameters of the same galaxies may be different in the two samples, which are all shown in Figure 1.

4.1.2. Observational galaxy triaxial shape distributions

The triaxial shape of a galaxy can be characterized by the two parameters, i.e., the medium-to-major axis ratio b/a and the minor-to-major axis ratio c/a , where a , b , and c represent the major, the medium, and the minor axis of an iso-density layer of the galaxy, respectively. The triaxial shape can also be described by an equivalent set of parameters i.e., the triaxiality $T \equiv (a^2 - b^2)/(a^2 - c^2)$ and the minor-to-major axis ratio c/a . The general triaxial description can be reduced to the following special cases: spherical shape with $b/a = c/a = 1$, oblate spheroid with $c/a < b/a = 1$, and

prolate spheroid with $c/a = b/a < 1$.

In the left panel of Figure 2, we show the shape distributions of early-type galaxies obtained from observations. The results obtained from the photometric study in the SDSS indicate that early-type galaxies are better described by triaxial shapes than by purely spheroidal shapes. As shown in the figure, the green plus symbol marks the possible range of the mean medium-to-major and minor-to-major axis ratios of the early-type galaxies in the SDSS DR3 data set (Vincent & Ryden 2005). The blue and red contours indicate the two-dimensional axis ratio distribution of early-type galaxies in the SDSS DR6 data set (Padilla & Strauss 2008) and the SDSS DR8 data set (Rodríguez & Padilla 2013), respectively. The results obtained from the ATLAS^{3D} galaxy sample, where both the photometric and the bulk kinematic information are used, show that early-type galaxies can be classified by fast- and slow-rotators (Emsellem et al. 2007; Krajnović et al. 2011). The magenta color bar marks the mean and the standard deviation of the minor-to-major axis ratios for a nearly oblate fast-rotator galaxy sample from the ATLAS^{3D} galaxy survey, obtained through a triaxial configuration fitting (Weijmans et al. 2014) (where the mean values of c/a and $\ln(1-b/a)$ are 0.33 and -5.0 , respectively, and their standard deviations are 0.11 and 0.08, respectively). The shape parameters cannot be well constrained for the slow-rotator galaxies, due to the limited sample size and the lack of a clearly defined projected rotation axis in many of the systems.

We will apply the different shape distributions to our study and see how different the results are affected by them.

4.2. Mock galaxy sample

As the observational sample size shown in Figure 1 is small, we construct a mock galaxy sample with a larger size for the statistical study of the BBH evolution in galaxies with realistic property distributions. The mock galaxy sample is generated based on all the galaxies shown in Figure 1 and follow the statistical distributions of their properties. For each galaxy in the mock galaxy sample, we first select a galaxy, e.g., galaxy i with parameters $\{\log R_b^i, \mu_b^i, \alpha^i, \beta^i, \gamma^i, M/L^i\}$, randomly from Figure 1, then add small scatters $\{\delta \log R_b^i, \delta \mu_b^i, \delta \alpha^i, \delta \beta^i, \delta \gamma^i, \delta M/L^i\}$ to the corresponding parameters and assign the new parameter set to the galaxy. All of the scatters are assumed to follow Gaussian distributions with zero means, and their standard deviations are assumed to be $\sigma_{\log R_b} = 0.2$, $\sigma_{\mu_b} = 0.4$, $\sigma_{\alpha} = 1.0$, $\sigma_{\beta} = 0.2$, $\sigma_{\gamma} = 0.2$, and $\sigma_{M/L} = 2.0$. None of those assumed standard deviations are larger than the standard deviations of the corresponding parameters of all the observational points shown in Figure 1. We delete those systems generated with unphysical $\beta < 0$ or $M/L < 0$. It is likely that some generated parameters lead to extreme systems, but they are rare and do not affect our results statistically.

Our calculations show that the detailed results are not sensitive to the exact values of the boundaries. Thus, a mock sample with a size of $\sim 10^7$ galaxies is generated in our study (see details in Section 4.5).

The generation of the scatters in observational parameters and the large number of the mock galaxy sample

will make the statistical results obtained from our Monte Carlo study appear smooth. If the standard deviations assigned to the parameter set are too small, the parameters of the mock galaxy sample will cluster around the points shown in Figure 1 and the application of the mock sample will result in significant discreteness or discontinuity in the statistical results (e.g., the curves of the surviving BBH distributions shown below). If the standard deviations are too large, some intrinsic cross correlations among the parameters of the observational galaxies shown in Figure 1 will be lost significantly in the mock sample. The values of the standard deviations in our mock sample are roughly chosen to be as small as possible to make our statistical results smooth and keep the correlations originally existing in the observational sample as much as possible.

Given a galaxy in the Mock galaxy sample with parameters $\{\log R_b, \mu_b, \alpha, \beta, \gamma, M/L\}$, the stellar density distribution within the galaxy can be determined as done by Equations (48)-(49) in Section 5.1 in Yu (2002).

The triaxial shape of a galaxy in the mock sample is generated randomly from the observational galaxy triaxial shape distribution described in Section 4.1.2, without considering the possible dependence of the galaxy shapes on galaxy properties, such as galaxy masses. In this work, we explore three sets of galaxy shape distributions presented in Padilla & Strauss (2008), Rodríguez & Padilla (2013), and Weijmans et al. (2014), respectively.

4.3. GSMFs and galaxy merger rates

As shown by Equation (14) in Section 3, the GSMFs, and the galaxy merger rates are needed to model the BBH populations. We present the GSMFs and the galaxy merger rates in Section 4.3.1 and 4.3.2, respectively.

4.3.1. Galaxy stellar mass functions

The GSMFs can be obtained from either observations (e.g., see Bernardi et al. 2013; Muzzin et al. 2013; Ilbert et al. 2013; Tomczak et al. 2014; Kelvin et al. 2014) or hydrodynamical simulations (e.g., see Torrey et al. 2015; Lim et al. 2017).

In the left panel of Figure 3, we show the observational GSMFs obtained at several discrete redshifts. In the right panel of Figure 3, we show the GSMF used in this work, which is obtained from Behroozi et al. (2019) and derived by matching their model to a compilation of different observational results and constraining the galaxy growth history inside DM haloes. The GSMF in Behroozi et al. (2019) extends from $z \sim 0$ to high redshifts up to $z \sim 10$ in sufficiently dense redshift space, and we illustrate them only at several redshifts in the figure. The observational results obtained from Ilbert et al. (2013) are also shown in this panel for comparison. We also illustrate the GSMF evaluated from the Illustris simulation (Vogelsberger et al. 2014), by adopting the fitting formula and the best-fitting parameters from Torrey et al. (2015), which appears to be relatively higher at both the low-mass (i.e., $\lesssim 10^{10} M_{\odot}$) and the high-mass (i.e., $\gtrsim 10^{11} M_{\odot}$) ends than the observational ones. The differences in the results caused by the difference in the GSMFs will be discussed in Section 6.

4.3.2. Galaxy merger rates

The galaxy merger rates can be evaluated from different ways including observations, numerical simulations, semi-analytical models, and semi-empirical methods (Hopkins et al. 2010a).

Observationally, it is usually determined by dividing the fraction of merging galaxies by a characteristic merger timescale, i.e., the fractional merger rate. The fraction of merging galaxies is usually determined through either close-pair counts or galaxy morphological disturbance. The characteristic merger timescale, which is usually called merger-averaged observability time, can be calibrated by hydrodynamic simulations of galaxy mergers (Lotz et al. 2008, 2010, 2011; Snyder et al. 2017) or cosmological dark matter halo N -body simulations (Kitzbichler & White 2008). For example, the fractional major merger rate of galaxies with total mass greater than M_{gal} at redshift z can be defined by

$$\mathcal{R}(> M_{\text{gal}}, z) \equiv \frac{f_{\text{mrg}}(> M_{\text{gal}}, z)}{\langle T_{\text{mrg}} \rangle} = \frac{C_{\text{mrg}} f_{\text{pair}}(> M_{\text{gal}}, z)}{\langle T_{\text{mrg}} \rangle}. \quad (41)$$

Here major mergers mean that the mass ratio of the two galaxies q_{gal} is greater than a value q_{major} , such as 1/3 or 1/4. In Equation (41), f_{mrg} represents the fraction of galaxies undergoing merging processes, which is the fraction of galaxies in close pairs f_{pair} multiplied by a factor C_{mrg} describing the probability of an observed close pair that will merge within a given time, e.g., ~ 0.6 in Lotz et al. (2011), and $\langle T_{\text{mrg}} \rangle$ is the merger-averaged observability time.

Alternatively, given the GSMF $n_{\text{gal}}(M_{\text{gal}}, z)$ and the galaxy merger rate per galaxy $\mathcal{R}_{\text{gal}}(q_{\text{gal}}, z | M_{\text{gal}})$ as defined in Section 3.1, the fractional major merger rate can be obtained by

$$\mathcal{R}(> M_{\text{gal}}, z) = \frac{\int_{M_{\text{gal}}}^{\infty} dM_{\text{gal}} n_{\text{gal}}(M_{\text{gal}}, z) \int_{q_{\text{major}}}^1 \mathcal{R}_{\text{gal}}(q_{\text{gal}}, z | M_{\text{gal}}) dq_{\text{gal}}}{\int_{M_{\text{gal}}}^{\infty} n_{\text{gal}}(M_{\text{gal}}, z) dM_{\text{gal}}}, \quad (42)$$

where $q_{\text{major}} = 1/4$. In this work, we adopt the galaxy merger rate from the Illustris simulation (Rodríguez-Gomez et al. 2015) (see Table 1 therein), where a simple formula is provided to describe the merger rate as a function of progenitor stellar mass ratio, descendant total stellar mass, and redshift.

We illustrate the fractional galaxy merger rates obtained from both the Illustris simulation and observations in Figure 4. To obtain galaxy merger rate from observations, the merger timescale $\langle T_{\text{mrg}} \rangle$ used in Equation (41) is obtained from numerical simulations. Below we list several examples.

- Based on virtual galaxy catalogues derived from the Millennium Simulation (Springel 2005), Kitzbichler & White (2008) calibrate the average observability timescale for galaxies in close pairs within a projected separation of r_{p} as

$$\langle T_{\text{mrg}} \rangle = 2.2 \text{ Gyr} \left(\frac{r_{\text{p}}}{50 \text{ kpc}} \right) \times \left(\frac{M_{\text{gal}}}{4 \times 10^{10} h^{-1} M_{\odot}} \right)^{-0.3} \left(1 + \frac{z}{8} \right), \quad (43)$$

where this timescale is for close pairs with relative radial velocity $< 300 \text{ km s}^{-1}$. For those close pairs

without the radial velocity difference constraint, the normalization of the observability timescale is increased by a factor of ~ 1.5 . In Equation (43), the dependences of $\langle T_{\text{mrg}} \rangle$ on the total mass M_{gal} and redshift z are both relatively weak.

- Lotz et al. (2008) and Lotz et al. (2010) conduct a series of hydrodynamic simulations of galaxy mergers with different mass ratios and orbital parameters to determine their average observability timescale. Based on these results, in Lotz et al. (2011), the distributions of baryonic gas fraction and mass ratio, as well as their redshift evolutions from cosmological-scale galaxy evolution models are adopted to obtain the average observability timescale for candidate galaxy mergers identified based on either close-pair counts or morphology disturbance. By fitting the results of Lotz et al. (2011), $\langle T_{\text{mrg}} \rangle$ is estimated to be 0.3 Gyr for a projected separation of $< 20 \text{ kpc}$; given that the candidates are selected by their masses ($\gtrsim 10^{10} M_{\odot}$, according to Xu et al. 2012), and thus we have

$$\langle T_{\text{mrg}} \rangle = 0.3 \text{ Gyr} \left(\frac{r_{\text{p}}}{20 \text{ kpc}} \right) \left(\frac{M_{\text{gal}}}{4 \times 10^{10} h^{-1} M_{\odot}} \right)^{-0.3} \left(1 + \frac{z}{8} \right), \quad (44)$$

where the dependences on the total mass M_{gal} and redshift z are adopted as those in Kitzbichler & White (2008) because the study in Lotz et al. (2011) does not provide the dependence. The timescale shown in Equation (44) is a factor of ~ 3 smaller than that of Equation (43).

- By comparing the synthetic close-pair catalogue with the intrinsic galaxy merger rate in the Illustris Simulations (up to redshift $z \sim 3$), Snyder et al. (2017) conclude that the averaged observability time incorporating C_{mrg} (i.e., $\langle T_{\text{mrg}} \rangle / C_{\text{mrg}}$) is a strong function of redshift, that is

$$\langle T_{\text{mrg}} \rangle / C_{\text{mrg}} \simeq 2.4 \times (1 + z)^{-2} \text{ Gyr}. \quad (45)$$

In the upper panel of Figure 4, we show the observational close-pair fractions at different redshifts and different galaxy mass ranges. In the lower panel of Figure 4, we show the fractional galaxy merger rates obtained from the numerical simulations in Rodríguez-Gomez et al. (2015), and the observational ones converted by using Equation (41) and Equation (45). We also convert the fractional galaxy merger rates obtained from the numerical simulations in Rodríguez-Gomez et al. (2015) to the close-pair fractions by using Equation (41) and Equation (45) and show them in the upper panel. As seen from the figure, the fractional galaxy merger rates obtained from the Illustris simulation in Rodríguez-Gomez et al. (2015) is close to the observational one converted by using Equation (45) (which evolves with redshift strongly). However, if the merger timescale depends weakly on redshifts as shown in Equation (44) or (43), the galaxy merger rates of Rodríguez-Gomez et al. (2015) will be much higher than those converted from observations at high redshifts $z \gtrsim 2$.

4.4. BH–host galaxy relations

As shown by the modeling of the BBH population in Equation (14) in Section 3, besides the GSMFs and the galaxy merger rates, the BH–host galaxy relation is also needed to determine the probability function $p_{\text{BH}}(M_{\text{BH}}, q_{\text{BH}} | M_{\text{gal}}, q_{\text{gal}}, z)$ and $p_*(M_*, q_* | M_{\text{gal}}, q_{\text{gal}}, z)$.

The determination of the BH–host galaxy relation is composed of the two parts: the relation between the MBH mass and the physical property of the hot component of a galaxy (i.e., either an elliptical galaxy or the bulge of a spiral or S0 galaxy), and the relation (e.g., mass ratio) between the physical properties of the hot component and the total component of a galaxy. Here the two parts are simply called as the BH–bulge relation and the bulge–galaxy relation.

In Figure 5, we show the BH–bulge relations obtained from different works in the literature (many of which can also be seen in Sesana 2013). The BH–bulge relations are parameterized in the equation below and the related parameters are listed in Table 1.

$$\log M_{\text{BH},1} = \tilde{\gamma} + \tilde{\beta} \log \sigma_{200} + \tilde{\alpha} \log M_{*,11}, \quad (46)$$

where $M_{\text{BH},1}$, σ_{200} , and $M_{*,11}$ correspond to the MBH mass in units of $1M_{\odot}$, the one-dimensional velocity dispersion in units of 200 km s^{-1} , and the bulge mass in units of $10^{11}M_{\odot}$, respectively. The intrinsic scatters of the different BH–bulge relations are quantified by $\tilde{\epsilon}$ in the table. We call the relation as the $M_{\text{BH}}\text{--}\sigma$ relation if $\tilde{\alpha} = 0$, the $M_{\text{BH}}\text{--}M_*$ relation if $\tilde{\beta} = 0$, and the $M_{\text{BH}}\text{--}M_*$ – σ relation if none of $\tilde{\alpha}$ and $\tilde{\beta}$ is zero. For those $M_{\text{BH}}\text{--}\sigma$ relations and $M_{\text{BH}}\text{--}M_*$ – σ relations with $\tilde{\beta} \neq 0$, we apply the relation between the velocity dispersion σ and the bulge mass M_* from Gallazzi et al. (2006), $\log(\sigma / \text{km s}^{-1}) = 0.286 \log(M_*/M_{\odot}) - 0.895$ (with an intrinsic scatter of 0.071dex) and convert them to the $M_{\text{BH}}\text{--}M_*$ ones to be shown in Figure 5, and the corresponding scatters in the converted $M_{\text{BH}}\text{--}M_*$ relations are set to be $\sqrt{\tilde{\epsilon}^2 + 0.071^2 \tilde{\beta}^2}$.

The bulge–galaxy relation is often characterized by the bulge-to-total stellar mass ratio B/T . The bulge-to-total ratio depends on the properties of the host galaxies, such as the morphology or the galaxy mass. In this work, we follow the prescription used by Ravi et al. (2015), where early-type galaxies are divided into ellipticals and S0s. The fractions of S0s and ellipticals are 75% and 25%, respectively, for $10 \leq \log(M_{\text{gal}}/M_{\odot}) \leq 11.25$, and 55% and 45%, respectively, for more massive galaxies. For ellipticals, the bulge-to-total mass ratio is $B/T = 1$; whereas for S0s, $B/T = 0.7$. For late-type galaxies, 90% of them have the bulge-to-total ratio $B/T = 0.2$, and the remaining 10% have no bulge component, i.e., $B/T = 0$. The scatter in B/T is assumed to be 0.1 dex for both early- and late-type galaxies. The fraction of early-type galaxies as a function of redshift and galaxy mass are approximated by the fraction of quenched galaxies presented in Behroozi et al. (2019).

4.5. Mock BBH evolution track library

In this subsection, we describe the construction of the mock BBH evolution library, based on the mock host galaxy sample described in Section 4.2, which will be

used to determine the statistical distributions of surviving BBHs, BBH coalescence rates, and GWB etc. in Section 5.

The BBH evolution track library contains the BBH evolution tracks, with different parameters $\{M_*, q_*, M_{\text{BH}}, q_{\text{BH}}\}$. The parameter grids are set in the following way. We set the BBH properties $(M_{\text{BH}}, q_{\text{BH}})$ so that $\log(M_{\text{BH}}/M_{\odot})$ is in the range from 5 to 10 with an interval of 0.1 and $\log q_{\text{BH}}$ is in the range from -3 to 0 with an interval of 0.1. Given each $(M_{\text{BH}}, q_{\text{BH}})$, we select 25,000 galaxies randomly from the mock galaxy sample constructed in Section 4.2. The mass of the spheroidal component of each galaxy can be evaluated based on its associated Nuker-law parameters and mass-to-light ratio. We use the method presented in Section 2 to calculate the BBH evolution track in each (triaxial) galaxy. For each host galaxy, the pre-merger mass ratio q_* is set so that $\log q_*$ is in the range from -3 to 0 with an interval of 0.1. In the BBH evolution library, the BBH evolution tracks do not depend on q_* . The number of the parameter grids is 3.75×10^7 . Note that the different systems in the mock library do not appear in the universe with the same probability, their existence probabilities in the universe are modulated by galaxy merger rates and the correlations between the MBHs and their host galaxies etc. (see more in Section 4.5.1 below).

We have tested that the above grids are sufficient for obtaining the GWB results, but more are needed to obtain the statistical distributions of surviving BBHs. For the systems with $\log(M_{\text{BH}}/M_{\odot})$ being in the range from 5 to 10 with an interval of 1.0 and $\log q_{\text{BH}}$ being in the range from -2 to 0 with an interval of 0.5 (see the illustrated example systems in Figs. 8–15), we increase the selected galaxy number from 25,000 to 100,000 for each $(M_{\text{BH}}, q_{\text{BH}})$, which adds another 1.5×10^6 evolution tracks to the library.

The mock BBH evolution track library is applied in the following way. Given a system with parameters $(M_*, q_*, M_{\text{BH}}, q_{\text{BH}})$, its BBH evolution track is obtained by matching to the appropriate BBH track in the BBH evolution library. The match is done by finding out the one in the BBH evolution library, e.g., system k , which has the minimum value of $\sum_j (\log X_j^k - \log X_j)^2$ ($j = 1, 2, \dots, 4$), where $X_j \in \{M_*, q_*, M_{\text{BH}}, q_{\text{BH}}\}$.

4.5.1. Monte Carlo integrations: application of the BBH evolution library

Below we describe how to obtain the distributions of the surviving BBHs $\Phi_{\text{BBH}}(M_{\text{BH}}, q_{\text{BH}}, a, z)$ (see Eq. 17) by applying the above BBH evolution library in a Monte-Carlo method. The similar method is also applied to obtain the coalescence rate $R_{\text{BH}}(M_{\text{BH}}, q_{\text{BH}}, z)$ and the stochastic GWB $h_c(f)$ etc. in this work.

We evaluate the distribution function of $\Phi_{\text{BBH}}(M_{\text{BH}}, q_{\text{BH}}, a, z)$ at the mesh points $(M_{\text{BH}}, q_{\text{BH}})$ of the BBH evolution track library, with $\log(a/p\text{c})$ being in the range from -6 to 1 with an interval of 0.1 and z being in the range of 0–3 with an interval of 0.1. As seen from Equation (17), given each point of $(M_{\text{BH}}, q_{\text{BH}}, a, z)$, the integration of Equation (17) is done over the $(\log M_*, \log q_*)$ space. We set the integration range of $\log(M_*/M_{\odot})$ to be within [8, 13] and that of $\log q_*$ to be within [−3, 0]. We divide the space of $(\log M_*, \log q_*)$ into 1500 small grids with

intervals $\Delta \log M_* = 0.1$ and $\Delta \log q_* = 0.1$, do a Monte Carlo integration within each small grid, and then add the integration results of all the grids up.

The part of the function $\Phi_{\text{BBH}}(M_{\text{BH}}, q_{\text{BH}}, a, z)$ contributed by the integrand within each small grid (see Eq. 17) can be obtained by

$$\begin{aligned} & (\ln 10)^2 \Delta \log M_* \Delta \log q_* \\ & \times \frac{1}{N} \sum_{i=1}^N n_*(M_*, z_i) \mathcal{R}_*(q_*, z_i | M_*) \\ & \times p_{\text{BH}}(M_{\text{BH}}, q_{\text{BH}} | M_*, q_*, z_i) H(t - \tau_{a,i}) \frac{t_{\text{evol},i}}{a}, \quad (47) \end{aligned}$$

where we set the number of the randomly generated galaxy merger events within a grid $N = 1000$, and the function $\Phi_{\text{BBH}}(M_{\text{BH}}, q_{\text{BH}}, a, z)$ can be obtained by the sum over all the grids. The value of $n_*(M_*, z) \mathcal{R}_*(q_*, z | M_*)$ in Equation (47) can be obtained (from some analytical formula) as described in Section 4.3. The function $p_{\text{BH}}(M_{\text{BH}}, q_{\text{BH}} | M_*, q_*, z)$ can also be described in an analytical way (see Section 4.4). The variables of $\tau_{a,i}$ and $t_{\text{evol},i}$ in the integrand of Equation (47) represent the BBH evolution in each generated galaxy merger event, which are evaluated by matching to the appropriate BBH track in the BBH evolution library as described in Section 4.5.

Note that the integration is dependent on the following physical ingredients, including the GSMF (n_{gal}), the galaxy merger rate per galaxy, the BH-host galaxy relation (p_{BH}), as well as the shape distribution of the host galaxies. In this paper, we consider how the results are affected with different inputs of those ingredients in our results.

5. RESULTS

In this section, we present the main results of this study. In Section 5.1, we illustrate some examples of BBH evolution tracks and the dependence of BBH evolution timescales on host galaxy triaxial shapes. In Section 5.2, we present the statistical properties of BBH evolution tracks expected in the realistic universe, e.g., the distribution of their bottleneck evolution timescales and the distribution of the slopes in their evolution timescale curves during the hard binary stages. In Section 5.3, we present statistical distributions of surviving BBHs, which are the very target of many observational surveys. In Section 5.4, we present the BBH coalescence rates. In Section 5.5, we present the strain amplitude of the stochastic GWB produced by the cosmic population of BBHs. In Section 5.6, we discuss some prospects for detecting individual sources at the PTA bands. In Section 5.7, we extend the study to investigate the contribution of the BBH mergers to the LISA detection bands.

5.1. BBH evolution tracks and timescales

In this subsection, we illustrate the examples for the BBH evolution tracks and the dependence of the BBH evolution timescales on galaxy triaxial shapes.

Figure 6 shows an example for the evolution tracks of a BBH inside a galaxy merger remnant. The example host galaxy (i.e., the merger remnant containing the BBH) has the typical properties, with surface brightness following a Nuker-law profile characterized by parameters

$\alpha = 3.97$, $\beta = 1.26$, $\gamma = 0.72$, and $R_b = 466$ pc. The system has a total stellar mass of $\log(M_*/M_\odot) = 12$ and contains a BBH at the center with total mass satisfying $\log(M_{\text{BH}}/M_\odot) = 8.6$. Two sets of BH mass ratios are assumed, i.e., 1/1 and 1/10, as shown by solid and dashed curves in the figure. Given a BBH mass ratio, the five sets of intrinsic triaxial shapes are assumed for the host merger remnant, i.e., $(b/a, c/a) = (1.0, 1.0)$ (red), $(1.0, 0.8)$ (green), $(1.0, 0.6)$ (blue), $(0.9, 0.8)$ (cyan) and $(0.8, 0.6)$ (magenta).

As described in Section 2, the evolution of a BBH goes through several stages driven by different physical mechanisms. In Figure 6, we mark the boundaries between these different stages, according to the definitions in Section 2. Along the direction of decreasing a , the black arrow labeled with “bound” marks the formation of a bound BBH, the black arrow labeled with “hard” marks the formation of a hard BBH, and the color arrows mark the transition to the gravitational radiation stage for the BBH evolution curves with the corresponding colors and line styles. We use the horizontal arrows labeled with t_{peak} to mark the maximum BBH evolution timescales after the BBHs become bound. As seen from the figure, the galaxy triaxiality can decrease the maximum BBH evolution timescale significantly, as shown by Figures 7–9 in Yu (2002).

For the example BBH system with $q_{\text{BH}} = 1$ shown in Figure 6, we also calculate their evolution with other galaxy host galaxy shapes, and show the dependence of their maximum evolution timescales on the shapes in Figures 2–7.

The right panel of Figure 2 shows the contours of $\log t_{\text{peak}}$, as a function of the two axis ratios of the mass density distribution (i.e., the medium-to-major axis ratio b/a and the minor-to-major axis ratio c/a). As seen from the figure, the contours of $\log t_{\text{peak}}$ are quite dense at the boundaries of $b = c$ and $a = c$, which implies that even a minor triaxiality can decrease t_{peak} significantly. As shown by the label on the contours, the values of t_{peak} decrease to significantly short timescales (shorter than the Hubble timescale) in a wide parameter space of triaxiality.

As an alternative way to illustrate the results in Figure 2, Figure 7 shows t_{peak} of the example BBH system as a function of the triaxiality parameter $T = (a^2 - b^2)/(a^2 - c^2)$ for the five sets of different minor-to-major axis ratios c/a . Except for the curves in nearly spherical system ($c/a = 0.99$ or 0.95), t_{peak} decreases sharply when the triaxiality deviates from $T = 0$ ($b/a = 1$) and $T = 1$ ($b = c$), which is consistent with the result shown in Figure 2.

5.2. Statistical properties of BBH evolution tracks

In this section, the statistical distributions of some properties describing the BBH dynamical evolution tracks are investigated, including the coalescence timescale $\tau_0 \equiv \tau_{a=0}$ (e.g., see Eq. 21) defined by the total time to be taken by a BBH to the final coalescence from the mergers of their host galaxies, the maximum timescale t_{peak} defined by the maximum evolution timescale of a BBH after the formation of the binary, the slope of the evolution curve of a BBH in the $\log t_{\text{evol}} - \log a$ space before its gravitational radiation stage, and

some other orbital properties of a BBH when it enters the gravitational radiation stage.

Consider that a population of galaxy mergers occur at redshift z' . Below we describe the statistical distributions of the evolution tracks of the BBHs formed by those galaxy mergers (note that these distributions are different from the statistical distributions of the surviving BBHs at a given redshift to be described in Section 5.3). Given a physical property x describing the BBH evolution tracks, we define its probability distribution function $\psi_x(x|M_{\text{BH}}, q_{\text{BH}}, z')$ by

$$\psi_x(x|M_{\text{BH}}, q_{\text{BH}}, z') \equiv \frac{\Psi_x(x, M_{\text{BH}}, q_{\text{BH}}, z')}{\Psi(M_{\text{BH}}, q_{\text{BH}}, z')}, \quad (48)$$

where

$$\begin{aligned} & \Psi(M_{\text{BH}}, q_{\text{BH}}, z') \\ & \equiv \int dM_* \int dq_* n_*(M_*, z') \mathcal{R}_*(q_*, z'|M_*) \\ & \quad \times p_{\text{BH}}(M_{\text{BH}}, q_{\text{BH}}|M_*, q_*, z'), \end{aligned} \quad (49)$$

and

$$\begin{aligned} & \Psi_x(x, M_{\text{BH}}, q_{\text{BH}}, z') \\ & \equiv \int dM_* \int dq_* n_*(M_*, z') \mathcal{R}_*(q_*, z'|M_*) \\ & \quad \times p_{\text{BH}}(M_{\text{BH}}, q_{\text{BH}}|M_*, q_*, z') \\ & \quad \times p_x(x|M_*, q_*, M_{\text{BH}}, q_{\text{BH}}, z'), \end{aligned} \quad (50)$$

In Equation (50), $p_x(x|M_*, q_*, M_{\text{BH}}, q_{\text{BH}}, z')$ is the probability function defined so that $p_x(x|M_*, q_*, M_{\text{BH}}, q_{\text{BH}}, z')dx$ represents the probability that the evolution tracks of the BBHs characterized by parameters $(M_{\text{BH}}, q_{\text{BH}}|M_*, q_*, z')$ has the corresponding physical property in the range $x \rightarrow x + dx$, where the BH mass growth is ignored before the BBH coalescence. We have $\int dx p_x(x|M_*, q_*, M_{\text{BH}}, q_{\text{BH}}, z') = 1$. The probability function $p_x(x|M_*, q_*, M_{\text{BH}}, q_{\text{BH}}, z')$ can be obtained by using Monte-Carlo simulations to generate $N (= 1000)$ galaxy mergers with the grid of the parameters (M_*, q_*) at z' leading to the formation of BBHs with parameters $(M_{\text{BH}}, q_{\text{BH}})$ and calculating the physical property x_i ($i = 1, 2, \dots, N$) of the corresponding BBH evolution tracks. Thus, we have

$$\begin{aligned} & p_x(x|M_*, q_*, M_{\text{BH}}, q_{\text{BH}}, z') \\ & = \frac{1}{N} \sum_{i=1}^N \delta(x - x_i|M_*, q_*, M_{\text{BH}}, q_{\text{BH}}) \\ & = \frac{1}{N} \frac{d}{dx} \sum_{i=1}^N H(x - x_i|M_*, q_*, M_{\text{BH}}, q_{\text{BH}}). \end{aligned} \quad (51)$$

In a similar way to obtain $\Phi_{\text{BBH}}(M_{\text{BH}}, q_{\text{BH}}, a, z)$ as described in Section 4.5.1, the part of the function $\Psi_x(x, M_{\text{BH}}, q_{\text{BH}}, z')$ contributed by the integrand within each small grid of (M_*, q_*) (see Eq. 50) can be obtained

by

$$\begin{aligned} & (\ln 10)^2 \Delta \log M_* \Delta \log q_* \\ & \times \frac{1}{N} \sum_{i=1}^N n_*(M_*, z') \mathcal{R}_*(q_*, z'|M_*) \\ & \times p_{\text{BH}}(M_{\text{BH}}, q_{\text{BH}}|M_*, q_*, z') H(x - x_i|M_*, q_*, M_{\text{BH}}, q_{\text{BH}}), \end{aligned} \quad (52)$$

and $\Psi_x(x, M_{\text{BH}}, q_{\text{BH}}, z')$ can be obtained by the sum over all the grids.

In Figures 8–11, we show the statistical results for the evolution tracks of BBHs caused by galaxy mergers occurring at $z' = 0$, by using Equation (48) and the method of the Monte Carlo integration as described above, where the galaxy merger rate is determined by the GSMF n_{gal} of Behroozi et al. (2019) and the galaxy merger rate per galaxy \mathcal{R}_{gal} of Rodriguez-Gomez et al. (2015). The BH mass is set, according to the $M_{\text{BH}}-M_*$ relation of Kormendy & Ho (2013) (KH13b in Table 1). The mock BBH evolution tracks obtained with the different intrinsic shape distributions of the early-type galaxies (see Figure 2) are adopted, and their results are compared.

Figure 8 shows the probability distribution of the logarithm of the BBH coalescence timescale, $\log \tau_0$. The left panels show the results for different M_{BH} , and the right panels show the results for different q_{BH} . From top to bottom panels, the results are obtained by choosing the different sets of the shape distribution of the host galaxy merger remnants presented in Weijmans et al. (2014), Rodriguez & Padilla (2013), and Padilla & Strauss (2008), respectively. As seen from the figure, we find the following points.

- The distribution of the coalescence timescale τ_0 spreads widely, from $\sim 10^8$ to $\sim 10^{12}$ yr.
- The left panels of the figure show that the distribution depends on the BBH total mass. The BBHs with high total masses (e.g., $\sim 10^9$ - $10^{10} M_{\odot}$) have a relatively large fraction of long τ_0 (e.g., longer than the Hubble timescale $\sim 10^{10}$ yr), as shown by that their distribution peaks shift rightwards, and those with low total masses have lower probabilities to have τ_0 longer than the Hubble timescale.
- The right panels of the figure show that the distribution depends on the BH mass ratios. The BBHs with smaller BH mass ratios (e.g., $q_{\text{BH}} = 0.01$) have a relatively larger fraction of long τ_0 , as shown by that the left sides of the distribution curves shift rightwards, which is mainly caused by the increasing dynamical friction timescales with smaller mass ratios, in consistency with the conclusions in Yu (2002). As shown in Yu (2002), for BBHs with mass ratio $\lesssim 10^{-3}$, the dynamical friction timescale is generally so long that they are hardly able to finish the in-spiral within a Hubble timescale.
- As seen from the different rows of the figure, the different choice of the shape distributions does not affect the above summary qualitatively. Quantitatively, the coalescence timescale distributions in the bottom panels, obtained by a nearly oblate spheroidal shape distribution of Weijmans et al.

(2014) are relatively broadened towards longer τ_0 , compared with those in the top and the middle panels. The coalescence timescale distributions in the top and the middle panels obtained from the triaxial shape distributions of Rodríguez & Padilla (2013) and Padilla & Strauss (2008), are close to each other.

Figure 9 shows the probability distribution of the logarithm of the maximum BBH evolution timescale t_{peak} after the BBHs become bound. As done in Figure 8, the results for the different shape distributions of the host merger remnants are adopted, the different BBH total masses, the different BBH mass ratios are shown in this figure. As seen from the left panels in Figures 8 and 9, the distributions of the peak evolution timescales are quite similar to those of the coalescence timescales, which suggests that the coalescence timescales τ_0 of BBHs with large mass ratios are dominated by their peak evolution timescale t_{peak} after the BBH becomes bound. However, different from the distributions shown in the right panels of Figure 8, the distributions of the peak evolution timescale after the BBH becomes bound is less sensitive to the BBH mass ratios.

Figure 10 shows the probability distribution of the slopes of the BBH evolution curves in the $\log t_{\text{evol}} - \log a$ space, during the hard binary stage, defined by $\alpha_{\text{BBH}} \equiv \frac{\log t_{\text{evol}}(a_{\text{gr}}) - \log t_{\text{evol}}[\max(a_{\text{h}}, a_{\text{dp}})]}{\log a_{\text{gr}} - \log[\max(a_{\text{h}}, a_{\text{dp}})]}$. The slope is an indicator of whether the loss cone is full or not. If the loss cone remains full at the hard binary stage, the slope is expected to be -1 . However, as the stars in the loss cone can be gradually removed due to the interaction with the BBH, the slope can deviate from -1 and be steeper significantly, if the stellar refilling rates into the loss cone are not high enough. The upper panels show the results obtained by using the intrinsic shape distribution of early-type galaxies from Padilla & Strauss (2008), and the lower panels show the results obtained by using the shape distribution from Weijmans et al. (2014). The results obtained by using the shape distribution from Rodríguez & Padilla (2013) are not shown here, as they are quite similar to those in the upper panels. As seen from the figure, the distribution of the slopes tends to shift leftwards (with decreasing or steeper values), as the BBH total mass becomes larger in the left panels or the BBH mass ratio becomes smaller in the right panels. Those trends are relatively stronger in the lower panels. Overall, the slopes are in the range from -4 to -1 for BBH systems with mass ratio greater than 0.1 , not deviating from the value -1 by orders of magnitude, which indicates that in most of those cases the stellar refilling rates to the loss cone are not low, compared to the rates in the full loss cone case.

Figure 11 shows the probability distributions of the physical properties marking the transition to the gravitational radiation stage, i.e., the semimajor axis a_{gr} , the GW frequency f_{gr} , and the orbital period P_{gr} in the top, middle, and bottom panels, respectively. As expected, the figure shows that larger BBHs tend to evolve into the gravitational radiation stage with larger semi-major axes and orbital periods and with smaller GW frequencies. The typical ranges of these properties shown in the figure can help to determine the chance of a given BBH system being at the gravitational radiation stage. In ad-

dition, the transitional orbital frequency is closely related with the bending frequency of the strain spectrum of the GWB from the cosmic population of BBHs, as will be seen in Section 5.5.

5.3. Distributions of the surviving BBHs

In this subsection, we present the results on the distributions of the surviving BBHs (e.g., see $\Phi_{\text{BBH}}(M_{\text{BH}}, q_{\text{BH}}, a, z)$ in Equation 14), by using the Monte Carlo integration described in Section 4.5.1. We show the distributions for the following physical variables: the BBH semi-major axis a , the orbital period P , the frequency f of their emitted GWs, and the relative circular velocity v of the BBHs. Given the total BBH mass, those variables are mutually convertible after the binary becomes bound (i.e., $a \lesssim R_{\text{inff}}$), since the gravitational force between the binary dominates the orbital motion of the BBH at such scales. For example, the orbital period distribution can be expressed through the semi-major axis distribution, i.e., $\Phi_{\text{BBH}}(M_{\text{BH}}, q_{\text{BH}}, a, z) \left| \frac{da}{dP} \right|$. The distributions of these variables may provide clues to discover surviving BBHs.

Figures 12–15 present the distributions of the BBH semi-major axis a , the orbital period P , the GW frequency f , and the relative circular orbital velocity v of the surviving BBHs, respectively. In each of these figures, the upper left panel shows the dependence of the distribution functions on the total mass of the BBHs at $z = 0$ with $q_{\text{BH}} = 1.0$ and $\log(M_{\text{BH}}/M_{\odot}) = 5.0, 6.0, 7.0, 8.0,$ and 9.0 ; the upper right panel shows the dependence on the BBH mass ratio for BBHs at $z = 0$ with $\log(M_{\text{BH}}/M_{\odot}) = 8.0$ and $\log q_{\text{BH}} = 0.0, -0.5, -1.0, -1.5,$ and -2.0 . Most of those surviving BBHs with properties significantly deviated from the corresponding peak locations have the evolution timescales significantly shorter than the Hubble timescale. The lower panels show the cumulative distributions of the corresponding upper panels. The figures show the medians of the results obtained by the different BH–host galaxy relations (similarly for Figs. 16 and 17 below). Regarding the orbital period distribution shown in the top left panel of Figure 13, we note that the observationally constrained orbital periods of some individual BBH candidates, e.g., ~ 12 yr for OJ 287 with $M_{\text{BH}} \simeq 1.83 \times 10^{10} M_{\odot}$ and $q_{\text{BH}} \simeq 0.01$ (Valtonen et al. 2008), $\sim 5.16 \pm 0.24$ yr for PG 1302 with $\log(M_{\text{BH}}/M_{\odot}) \simeq 8.3\text{--}9.4$ (Graham et al. 2015), or ~ 1.2 yr for Mrk 231 with $M_{\text{BH}} \simeq 1.5 \times 10^8 M_{\odot}$ and $q_{\text{BH}} \simeq 0.026$ (Yan et al. 2015), are not located at the peak locations of the distributions corresponding to their BBH masses, which would imply a relatively higher probability that more surviving BBH candidates are likely to be detected in future. In these figures, we also show the distributions contributed only by those BBHs with coalescence timescale τ_0 shorter than the Hubble timescale (by the dot-dashed curves). The differences between the solid and the dot-dashed curves in the figure indicate that the distributions of the surviving BBHs with large semi-major axes/long orbital periods/low GW frequency/low relative velocities (at the binary stages) are mainly contributed by those not being able to finish their final coalescences within the Hubble timescale, while the distributions of the BBHs with low semimajor axes (at the gravitational radiation stage) are those that can coalesce

within the Hubble timescale.

Figure 16 plots the fraction of MBHs in galaxies that host surviving BBHs, as a function of redshift. In the top left panel, only the BBHs with separation $0 < a \leq 10 \text{ pc}$ and mass ratio $q_{\text{BH}} \geq 1/3$ are included in estimating the BBH fraction, i.e., $\int_0^{10 \text{ pc}} da \int_{1/3}^1 dq_{\text{BH}} \Phi_{\text{BBH}}(M_{\text{BH}}, q_{\text{BH}}, a, z) / n_{\text{BH}}(M_{\text{BH}}, z)$, where $n_{\text{BH}}(M_{\text{BH}}, z)$ is defined so that $n_{\text{BH}}(M_{\text{BH}}, z) dM_{\text{BH}}$ represents the comoving number density of MBHs with mass within the range $M_{\text{BH}} \rightarrow M_{\text{BH}} + dM_{\text{BH}}$ at redshift z . As seen from the top left panel, the surviving BBH fractions are around $\sim 1\%$ – 3% (solid curves) for different BH masses at $z \lesssim 3$, and the BBH surviving fractions increase with increasing BH masses for $M_{\text{BH}} \lesssim 10^7 M_{\odot}$ and decrease with increasing BH masses for $M_{\text{BH}} \gtrsim 10^7 M_{\odot}$. The surviving fractions change mildly with redshifts for BBHs mass in the range of $10^6 M_{\odot} \lesssim M_{\text{BH}} \lesssim 10^9 M_{\odot}$. Among the surviving BBHs, more than about a half have total evolution timescales shorter than the Hubble timescale, according to the comparison between the dot-dashed curves and the solid curves. The surviving BBH fractions with $q_{\text{BH}} \geq 1/100$ increase to $\sim 10\%$ as shown in the bottom left panel. In the right panels, only the BBHs with orbital periods $1 \text{ yr} < P < 10 \text{ yr}$ or $1 \text{ yr} < P < 30 \text{ yr}$ are included in estimating the BBH fraction. As seen from the top right panel, at $z = 0$, the fractions of surviving BBHs with $q_{\text{BH}} \geq 1/3$ and orbital periods $1 \text{ yr} < P < 10 \text{ yr}$ are expected to be $\sim 0.5\%$ – 1% in MBHs with $M_{\text{BH}} \sim 10^6$ – $10^7 M_{\odot}$, the fractions of those with $1 \text{ yr} < P < 30 \text{ yr}$ are expected to be $\sim 2\%$ in MBHs with $M_{\text{BH}} \sim 10^6$ – $10^7 M_{\odot}$, and the fractions decrease in MBHs with other masses, down to 10^{-4} for $M_{\text{BH}} \sim 10^9 M_{\odot}$. The fractions are not sensitive to redshifts at $z \lesssim 3$. The fractions of surviving BBHs with $q_{\text{BH}} \geq 1/100$ and $1 \text{ yr} < P < 30 \text{ yr}$ increase to $\sim 10\%$ for $M_{\text{BH}} \sim 10^6$ – $10^7 M_{\odot}$ and $\sim 6 \times 10^{-3}$ for $M_{\text{BH}} \sim 10^9 M_{\odot}$, as shown in the bottom right panel.

5.4. BBH coalescence rates

In this subsection, we present the results on the BBH coalescence rates (see Eq. 20), by using the Monte Carlo method described in Sections 3–4. The BBH coalescence rate traces the merger rate of their host galaxies, but with a BBH evolution time delay. This time delay is obtained based on the BBH dynamical evolution model as described in Section 2.

Figure 17 shows the BBH coalescence rates (R_{BH} ; see Eq. 20) as a function of redshift (thick solid curves), and their dependence on BBH total masses (left panels) and mass ratios (right panels). In Equation (20), the BBH coalescence rates are obtained with including the BBH dynamical evolution after their host galaxy mergers, where we adopt the galaxy shape distribution of Padilla & Strauss (2008), the galaxy merger rate based on the galaxy stellar mass function of Behroozi et al. (2019), the merger rate per galaxy of Rodriguez-Gomez et al. (2015), and all the different BH–host galaxy relations shown in Table 1. We show the median values of the results obtained with the different BH–host galaxy relations as the thick solid curves in the figure. In the lower panels, we show the corresponding volume-integrated BBH coalescence rates as a function of redshift. If the BBH evolution

is ignored and the BBH coalescence is assumed to occur immediately after the host galaxy merger, we use Equation (25) to obtain the BBH coalescence rates and show them as dashed lines as a reference. As seen from the figure, for those BBHs with smaller mass ratios which have relatively larger coalescence timescales, the results obtained with the inclusion of the BBH evolution time delay (solid curves) have relatively lower rates at high redshifts for low q_{BH} , compared to the results obtained without including the BBH evolution time delay (dashed curves). The total BBH coalescence rate at $z \lesssim 3$ can be up to $\sim 1 \text{ yr}^{-1}$.

To illustrate the uncertainty in the BBH coalescence rate estimation, we use Figure 18 to show the BBH coalescence rates obtained by the different sets of the BH–host galaxy relations in Table 1. The left panels show the coalescence rates of BBHs with total mass $M_{\text{BH}} = 10^5 M_{\odot}$ and mass ratio $q_{\text{BH}} = 1$, and the right panels show the coalescence rates of BBHs with total mass $M_{\text{BH}} = 10^8 M_{\odot}$ and mass ratio $q_{\text{BH}} = 0.01$. The figure shows that the BBH coalescence rates estimated with the different choices of the BH–host galaxy relations can differ by two orders of magnitude.

5.5. Stochastic GWB at the PTA bands

In this subsection, we obtain the stochastic GWB spectra radiated from the cosmic population of BBHs, by using Equation (31) and the Monte Carlo integration method described in Section 4.5.1, where the characteristic strain amplitude of the background h_c is determined by several astrophysical ingredients, including the GSMF, the merger rate per galaxy, the BH–host galaxy relation, and the BBH evolution timescale after the host galaxy mergers. We try the different sets of BH–host galaxy relations in the estimation; with the results being treated with equal weight. Their median and the standard deviation are then used to characterize the expectation and uncertainty of the stochastic GWB.

We show the obtained characteristic strain spectra of the stochastic GWB across the PTA bands, produced by the modeled cosmic population of BBHs, in Figure 19. In the estimation, we adopt the GSMF of Behroozi et al. (2019) and the galaxy merger rate given by Rodriguez-Gomez et al. (2015), and we use the different color curves to show the results obtained by the different BH–host galaxy relations listed in Table 1. By treating all the results with equal weight, we show their median as the black solid curve and their standard deviation around the median as the shaded region in the lower panel of Figure 19. In Figure 19, at the relatively high-frequency bands ($f \gtrsim 10^{-9} \text{ Hz}$), the black dashed line represents the median strain spectrum obtained by assuming that the BBH coalescence occurs immediately after the galaxy merger (i.e., applying Eq. 25 and setting $\langle \frac{t_{\text{evol},i}}{t_{\text{gr}}} \rangle = 1$ in Eq. 33), which follows the $-2/3$ power law as a function of the observational frequency. The bending of the strain spectrum shown at the low-frequency end ($\lesssim 10^{-9} \text{ Hz}$) is caused by that a significant part of the BBH energy loss is driven by three-body interactions with surrounding stars, and the spectrum corresponds to the BBH evolution tracks at $a \gtrsim a_{\text{gr}}$. As seen from Figure 19, the largest strain amplitude at $f = 1 \text{ yr}^{-1}$, denoted by A_{yr} ,

is $A_{\text{yr}} \simeq 5.4 \times 10^{-16}$, obtained by adopting the $M_{\text{BH}}-M_*$ relation of [Kormendy & Ho \(2013\)](#); whereas the lowest strain amplitude is $A_{\text{yr}} \simeq 6.1 \times 10^{-17}$, obtained by adopting the $M_{\text{BH}}-M_*-\sigma$ relation of [Shankar et al. \(2016\)](#). The difference in the GWB estimates can be as large as ~ 10 due to different choices of the BH–host galaxy relationships. As seen from [Figure 19](#), the median value (black solid curve) at $f = 1 \text{ yr}^{-1}$ is $A_{\text{yr}} \simeq 2.0 \times 10^{-16}$, which is lower than that of the black dashed line by a factor of ~ 1.5 , with a standard deviation of ${}_{-0.8}^{+1.4} \times 10^{-16}$ around the median. As shown by the red and the yellow points in the figure, the current 95% upper limits on the stochastic GWB from the NANOGrav and the IPTA at $f = 1 \text{ yr}^{-1}$ are 1.45×10^{-15} ([Arzoumanian et al. 2018](#)) and 1.7×10^{-15} ([Verbiest et al. 2016](#)), respectively. The 95% upper limits from the PPTA at $f = 1 \text{ yr}^{-1}$ is 1.0×10^{-15} ([Shannon et al. 2015](#)). The largest strain amplitude at $f = 1 \text{ yr}^{-1}$ shown in [Figure 19](#) is below those currently constrained upper limit by a factor of ~ 2 , while the median of the predicted values is smaller than the current limit by a factor of ~ 5 . As shown in the figure, the expected strain amplitudes at a little lower frequency $f \sim 10^{-8}$ Hz are well within the expected detection ability of the on-going PTA experiments in the future [cyan curve estimated for the Square Kilometer Array (SKA) PTA formed by monitoring 50 pulsars at 100ns precision for 15 years ([Bonetti et al. 2018](#))], except for the lowest strain amplitudes estimated by using the BH–host relation provided by [Shankar et al. \(2016\)](#).

To quantify the bending trends of the strain spectrum, we fit each estimated strain spectrum shown in [Figure 19](#), by using the following equation:

$$h_c(f) = A \frac{(f/\text{yr}^{-1})^{-2/3}}{[1 + (f_{\text{bend}}/f)^{\kappa_{\text{gw}} \gamma_{\text{gw}}}]^{1/(2\gamma_{\text{gw}})}}, \quad (53)$$

where the parameters f_{bend} , κ_{gw} , and γ_{gw} encode the information about the physical processes driving the evolution of the BBHs before they enter the gravitational radiation stage and the distributions of the BBHs. Equation (53) is reduced to Equation (24) of [Arzoumanian et al. \(2016\)](#) if $\gamma_{\text{gw}} = 1$. The κ_{gw} is the low-frequency spectral index of the broken power-law GWB strain spectrum, related to the slope of the BBH evolution track during the hard binary stage, i.e., $\kappa_{\text{gw}} = 8/3 - 2/3(d \log t_{\text{evol}}/d \log a)$. The turnover frequency f_{turn} , defined by the frequency at which the strain spectrum reaches its maximum, is a function of f_{bend} , κ_{gw} , and γ_{gw} as follows (see Equation 30 in [Arzoumanian et al. 2016](#)).

$$f_{\text{turn}} = f_{\text{bend}} \left(\frac{3\kappa_{\text{gw}}}{4} - 1 \right)^{1/(\gamma_{\text{gw}} \kappa_{\text{gw}})}. \quad (54)$$

In [Table 1](#), we list the estimated GWB strain amplitudes at the observational GW frequency 1 yr^{-1} , A_{yr} , and the fitting parameters f_{turn} and κ_{gw} for each BH–host galaxy relation used in this study. As shown in [Figure 19](#), the assumption of instantaneous BBH mergers leads to an overestimate of the GWB strain amplitudes, compared to the case with considering the BBH evolution processes. Our calculations show that the overestimates are in the range of ~ 0.10 – 0.20 dex for those corresponding cases listed in [Table 1](#) (see the ‘‘Drop’’

column). In the model, we use the shape distribution of [Padilla & Strauss \(2008\)](#) for the BBH evolution. We have checked that the adoption of galaxy shape distribution of [Rodríguez & Padilla \(2013\)](#) gives similar strain amplitudes, and the adoption of galaxy shape distribution of [Weijmans et al. \(2014\)](#) leads to a further decrease by ~ 0.15 dex.

In [Table 1](#), the turnover frequencies f_{turn} are all within the range $[10^{-10}, 10^{-9}]$ Hz, with a median of 0.25 nHz, which is beyond but close to the lower boundary of current PTA frequency band. If the evolution of the inspiraling BBHs during the hard binary stage is always in the full loss-cone regime, we have $d \log t_{\text{evol}}/d \log a = -1$ and $\kappa_{\text{gw}} = 10/3$. In realistic cases, however, the evolution of the BBHs gradually departs from the full loss-cone regime and correspondingly κ_{gw} (in the range of ~ 3.3 – 4.6) increases a little compared to the full loss-cone case.

At the high-frequency end of the PTA band, the integrated number of BBHs emitting GWs at these frequencies is too small for Equation (31) to act as a good approximation ([Roebber et al. 2016](#); [Kelley et al. 2017](#)). In addition to showing the results of the Monte Carlo integration, we evaluate the strain spectrum from a realization of the cosmic population of BBHs and show the results in [Figure 20](#). The realization of the cosmic BBH population is based on the number distribution function of these objects in the parameter space $(z, M_{\text{BH}}, q_{\text{BH}}, f_{\text{obs}})$ (in a rejection method; e.g., see [Bevington & Robinson 2003](#)) and the total number of the sources is the integration of the number distribution over the 4-dimensional parameter space. We obtain ten realizations of the cosmic BBH population by using the method. With the realizations, we can also select out the individual sources loud enough to stand out of the average background, which will be presented in the next subsection.

[Figure 20](#) shows that the GWB strain spectrum obtained from the ten realizations of the cosmic BBH populations (grey curves) which deviates from the $-2/3$ power law (purple curve) and fluctuates due to the small number of BBH sources at the high-frequency end. Here the strain spectrum is obtained by adopting the $M_{\text{BH}}-M_*$ relation of [Kormendy & Ho \(2013\)](#), which gives the largest estimate of the GWB amplitude in [Figure 19](#) (see the purple curve). In [Figure 20](#), each grey jagged curve show the strain spectrum estimated from one Monte Carlo realizations of the cosmic BBH sources. We present the details on how to divide frequency bins and obtain this curve in [Section 5.6](#) below. Note that in each frequency bin, the source with the strongest strain (h_c ; see [Eq. 58](#)) in each realization is excluded to obtain the grey curve, and it is counted as an individual source with its characteristic strain (cf. [Eq. 55](#)) being larger than the background, and the grey curve (background) is contributed by the remaining sources in the same frequency bin. As seen from the figure, the strain spectra based on Equation (55) below for the Monte Carlo realizations of the cosmic BBH sources are well described by the $-2/3$ power law at $f \lesssim 10^{-8}$ Hz. At higher frequencies, the strain spectra based on the Monte Carlo realizations tend to fall below the power-law expectation, but with some spikes being above the power law expectation (see also [Roebber et al. 2016](#)). This is the frequency range where

individual sources emerge from the background, and the detection of the individual sources will be discussed in the next subsection.

To study which parts of galaxy merger populations contribute significantly to the stochastic GWB, in Figure 21 we show the fractions of the total GW energy density (blue dashed) and the total characteristic strain amplitude (blue solid) contributed by galaxy mergers with merger redshift $< z$ (left), total galaxy mass $< M_{\text{gal}}$ (middle), and galaxy mass ratio $> q_{\text{gal}}$ (right), at the observational frequency $f = 1 \text{ yr}^{-1}$. Similarly, to tell the contribution of different parts of BBH populations to the stochastic GWB, in Figure 21 we also show the fractions of the total GW energy density (red dashed) and the total characteristic strain amplitude (red solid) contributed by BBHs with coalescence redshift $< z$ (left), total BBH mass $< M_{\text{BH}}$ (middle), and BBH mass ratio $> q_{\text{BH}}$ (right), at the observational frequency $f = 1 \text{ yr}^{-1}$. As seen from Figure 21, most of the GWB energy density is contributed by galaxy or BBH mergers within redshift lower than 2, with total galaxy mass within $\sim 10^{10}$ – $10^{12} M_{\odot}$ or BBH mass within $\sim 10^8$ – $10^{10} M_{\odot}$, and with merging galaxy or BH mass ratio greater than ~ 0.01 .

5.6. Individual sources

Detection of signals from individual BBH systems, though beyond the current capability of PTAs (Lee et al. 2011; Arzoumanian et al. 2014; Zhu et al. 2014; Babak et al. 2016), would be also of great interest and provide insights into the BBH population in a different way from the global constraint from the stochastic GWB. Individual BBH systems can be possible targets of telescopes detecting electromagnetic signals so that the physical properties of some sources can be further investigated individually. Detection of a large number of individual BBHs systems will also enable a statistical study of the formation and evolution of the BBH population (Rosado et al. 2015; Kelley et al. 2018).

The prospects of detecting GW signals from individual BBHs by current and future PTAs have been investigated in the previous works (e.g., see Sesana et al. 2009; Ravi et al. 2015; Rosado et al. 2015; Kelley et al. 2018). For example, based on the halo merger rate from the Millennium simulation, together with different BH–host halo relations, Sesana et al. (2009) assemble a cosmic BBH sample and estimate that at least one resolvable source might be detected by future PTAs involving with SKA observations. Ravi et al. (2015) find that though beyond the capability of current PTAs, signals from up to ~ 3 BBHs could be detected by a PTA consisting of ~ 100 pulsars with ~ 100 ns timing precision for an observation period of 5 yr with a cadence of two months (Ellis et al. 2012), which might be achievable with the SKA. Despite this, bursts from coalescing BBHs are still not likely to be detectable. On the other hand, Rosado et al. (2015) try to answer if the detection of signals from individual sources comes before that from the stochastic background. A broad set of simulations covering a large parameter space of the BBH populations are employed. And appropriate detection statistics are used to evaluate the detection probability for both kinds of signals. They find that though the stochastic GWB is more likely to be detected first, the detection probability for individ-

ual sources is not negligible. Recently, based on mock PTAs, Kelley et al. (2018) estimate that the individual sources are likely to be detected with ~ 20 yr total observing baselines of PTAs. However, this detection time may double if several red noises hide in the PTA data.

As mentioned in Section 5.5, we use the Monte Carlo method to generate the cosmic BBH sources; and then we obtain their GW strain spectrum in the following way. As done in Roebber et al. (2016), we assume a $T_{\text{obs}} = 25$ yr PTA program, with an observational cadence of 6 weeks. The width of each frequency bin is $\Delta f = 1/T_{\text{obs}} \simeq 1.3$ nHz. And the GWs at the frequencies between a minimum value $f_{\text{min}} \simeq 1.3$ nHz and a maximum value $f_{\text{max}} \simeq 100$ nHz is assumed to be explored by the PTA program. Within each frequency bin $[f_k, f_k + \Delta f]$ ($k = 1, 2, \dots$), the characteristic strain amplitude is the incoherent sum of the GW signal of each BBH with GW frequency $f_i \in [f_k, f_k + \Delta f]$ and given by

$$h_c(f_k) = \sqrt{\sum_i h_i^2(f_{r,i}) \min(\mathcal{N}_i, f_i T_{\text{obs}})}, \quad (55)$$

where $h_i(f_{r,i})$ is the sky- and polarization-averaged strain amplitude of GW produced by the BBH system i at the source-rest GW frequency $f_{r,i} = f_i(1 + z_i)$ and given by the following formula (Thorne 1987)

$$h_i(f_r) = \sqrt{\frac{32}{5} \frac{(GM)^{5/3}}{c^4 R_c(z)} (\pi f_r)^{2/3}}, \quad (56)$$

$R_c(z)$ is the comoving distance of the GW source at redshift z and lower than its luminosity distance by a factor of $1/(1 + z)$, $\mathcal{N} = f_r^2 / \dot{f}_r$, and

$$\dot{f}_r = \frac{96\pi^{8/3} G^{5/3}}{5c^5} \mathcal{M}^{5/3} f_r^{11/3}. \quad (57)$$

Within the given frequency bin, there are two types of sources, i.e., those continuous sources satisfying $\mathcal{N} \geq f T_{\text{obs}}$ and those in-spiraling sources satisfying $\mathcal{N} < f T_{\text{obs}}$, and $\min(\mathcal{N}_i, f_i T_{\text{obs}})$ is roughly the number of cycles that a binary spends within the given frequency bin during the observational time T_{obs} .

In Figure 20 we show the characteristic strain amplitude h_c of the individual sources of the ten realizations of the cosmic BBH populations. Note that in our model, given one realization of the cosmic BBH population, only the loudest source in each frequency bin is picked out as a candidate of an individual source and shown as a color circle in Figure 20, where different colors represent different BBH masses. Those individual sources are excluded when estimating the backgrounds whose strain spectra are shown by the grey curves in the figure. However, in principle, multiple loud sources from the same frequency bin could be extracted simultaneously, since signals may come from different directions of the sky and could be resolved by PTAs spatially, as well as chromatically (Ravi et al. 2012; Babak & Sesana 2012; Boyle & Pen 2012). In this work, we do not consider this situation, since its probability is small when the detector sensitivity is not high enough; (e.g., see also Kelley et al. 2018). As seen from Figure 20, the majority of the sources are located at frequencies $f \gtrsim 10^{-8}$ Hz, and some of the loudest individual sources have the characteristic strain larger than

that given by the purple curve following the $-2/3$ power law. The strongest individual sources are below the current upper limits from the PTA analysis (see red, green, and blue curves) by one order of magnitude.

In Figure 20, for reference, we also illustrate the characteristic strain amplitudes as a function of frequency of BBHs at redshift $z = 0.1, 0.2,$ and 1.0 , with BH mass ratio $q_{\text{BH}} = 0.1$, and with total masses $M_{\text{BH}} = 10^{10}M_{\odot}, 10^9M_{\odot},$ and 10^8M_{\odot} , respectively, which is given by

$$h_c(f) = h(f_r) \sqrt{\min(\mathcal{N}, fT_{\text{obs}})} \quad (58)$$

(see the black lines).

Figure 20 can provide some prospects for detecting individual BBH systems in the GW domain, though a quantitative investigation on the detection time estimation for these sources is beyond the scope of this work, which involves signal searching strategies, noise models and detector conditions. Firstly, the best constraints of current PTAs on continuous individual sources are at frequencies $f \sim 5 \times 10^{-9} - 10^{-8}$ Hz. However, the majority of the high-signal sources located above the stochastic background are at larger frequencies. Secondly, at frequencies $f \gtrsim 10^{-8}$ Hz, some of the loudest individual sources have characteristic strain larger than that given by the $-2/3$ power law. In contrast, the stochastic background from realizations of the cosmic BBH population has rms characteristic strain below the power law. Thirdly, those individual BBHs that have the highest signals generally have total masses $M_{\text{BH}} \sim 10^9M_{\odot}$ and low redshift $z \lesssim 1$, which should be among the first detection of the individual sources. The average numbers of the individual sources with signals higher than the background (grey curve) for one realization of the BBH population shown in the figure are ~ 1.0 at $h_c \gtrsim 10^{-15}$ and ~ 8.7 at $h_c \gtrsim 3 \times 10^{-16}$, potentially achievable by the PTA experiments involving next-generation radio telescopes, such as SKA and ngVLA.

5.7. Contribution to the LISA detection bands

In the above subsection, we investigate the GW radiation from the cosmic population of the BBHs at the frequency band of PTAs, and in this subsection we extend the investigation to higher GW frequencies (~ 0.1 mHz– 0.1 Hz; LISA/Taiji/Tianqin detection bands) and study the prospects of detecting GW signals from less massive BHs.

By using one Monte Carlo realization of the BBH populations generated in Section 5.5 and assuming a three-year or ten-year observational time of the LISA mission, we plot the characteristic strain of the BBH systems covering the whole mission period in Figure 22 (shown as the color lines, with different colors representing different total BBH masses, mass ratios, and redshifts in the top, middle, and bottom panels, respectively), and their starting values at the beginning of the observation are shown as the points. As seen from the figure, some of the sources have significant frequency shifts during the observation periods.

At frequencies $f \gtrsim 10^{-4}$ Hz, the number of the sources is not significant to form a background. However, as a reference, in Figure 22 we also plot the strain spectrum of the possible stochastic background estimated from the integration of Equation (31) as the red dashed line, with

the integration limits $M_{\text{BH}} > 10^5M_{\odot}, q_{\text{BH}} > 10^{-3}$.

For each generated source within the LISA band, we can calculate the signal-to-noise ratio (SNR) of the source for a given observational duration by using Equation (19) of Moore et al. (2015), i.e.,

$$\text{SNR} = \sqrt{\int_{-\infty}^{\infty} d \ln f \left[\frac{h_c(f)}{h_n(f)} \right]^2}, \quad (59)$$

where $h_n(f)$ corresponds to the LISA sensitivity curve shown in Figure 22. By simulating ten Monte Carlo realizations of the BBH samples within the LISA band, the average total number of the events with SNR above 8 is 2.8 for a 3-year mission and 9.1 for a 10-year mission, and thus the detection rate for LISA is estimated to be $\sim 0.9 \text{ yr}^{-1}$ (obtained by using the $M_{\text{BH}} - M_*$ relation of Kormendy & Ho 2013).

The above detection rate of BBHs by LISA is consistent with our previous results shown in Section 5.4. For the BBH coalescence rates shown in Figure 17, the integrated coalescence rate of the BBHs over the same ranges of total masses $M_{\text{BH}} > 10^5M_{\odot}$ and mass ratios $q_{\text{BH}} > 10^{-3}$ is $\sim 0.63 \text{ yr}^{-1}$, which is the median value of the results obtained by adopting all the BH–host galaxy relations listed in Table 1. If we adopt the $M_{\text{BH}} - M_*$ relation of Kormendy & Ho (2013) (see the bottom left panel of Figure 18), the integrated coalescence rate over the above same integration limits is $\sim 0.86 \text{ yr}^{-1}$, which is close to the median value. The BBH coalescence rate is consistent with the estimated LISA detection rate, since most of these sources have signals at their final chirping stages well above the LISA detection threshold. As seen from Figure 18, the possible range of the BBH coalescence rate can span two orders of magnitude, due to the use of the different BH–host galaxy relations (for example, at redshift $z \sim 3$, the standard deviation of the logarithms of the cumulative BBH coalescence rates around the median shown in Figure 18 is ${}_{-0.68}^{+0.46}$ dex for the case of $\log(M_{\text{BH}}/M_{\odot}) = 5$ and $\log q_{\text{BH}} = 0$ and ${}_{-0.46}^{+0.54}$ dex for the case of $\log(M_{\text{BH}}/M_{\odot}) = 8$ and $\log q_{\text{BH}} = -2$). If taking into account this scatter, the possible range of the LISA detection rate should be $\sim 0.1 - 10 \text{ yr}^{-1}$, with a median close to 0.9 yr^{-1} .

The events contributing to the LISA detection in Figure 22 are mainly from those sources with $M_{\text{BH}} \sim 10^5 - 10^7M_{\odot}, q_{\text{BH}} \gtrsim 0.01,$ and $z \lesssim 3$. The modeling of the low-mass BBH population here only represents an extrapolation of the BBH population obtained partly based on the BH–host galaxy relations determined from the high-mass BH sample, and MBHs with smaller masses, e.g., $M_{\text{BH}} \lesssim 10^5M_{\odot}$, is not considered here. The low-mass BBH population from the MBH seeds formed at high redshifts might provide an additional contribution to the detection. For example, based on the cosmological hydrodynamical simulations from the EAGLE project (Schaye et al. 2015), Salcido et al. (2016) predict a detection rate of ~ 2 per year for the eLISA, and Figures 7-8 in Salcido et al. (2016) find two peaks of the distribution of sources in the strain-merging frequency space, one of which has a location consistent with ours, while the other of which is caused by BBHs with smaller masses. A comparison of the previous results obtained from semi-analytical models (which predict higher rates by about

one order of magnitude) and those from hydrodynamical simulations can also be found in [Katz et al. \(2019\)](#) (see Table 2 therein).

6. DISCUSSION

Below we discuss and summarize the effects on the estimation of the stochastic GWB caused by the different factors.

- **GSMFs:** we also calculate the strain amplitudes by adopting the GSMFs of [Torrey et al. \(2015\)](#), [Tomczak et al. \(2014\)](#), [Ilbert et al. \(2013\)](#), and [Muzzin et al. \(2013\)](#), and find that the ratios of these results to the result obtained by adopting the GSMF of [Behroozi et al. \(2019\)](#) are 2.06, 0.92, 1.04, and 1.08, respectively. The difference in the estimated strain amplitude caused by the difference in the GSMFs, except for that from [Torrey et al. \(2015\)](#), is negligible.
- **Galaxy merger rates:** the uncertainties in the logarithm of the GW strain can be contributed roughly by half of the uncertainties in the logarithm of galaxy merger timescales and in the logarithm of close-pair fractions given by observations. The difference in the galaxy merger timescales of [Kitzbichler & White \(2008\)](#) and [Lotz et al. \(2011\)](#) is a factor of ~ 3 (see Eqs. 43 and 44), and the logarithm of the strain amplitude estimated by adopting those of [Kitzbichler & White \(2008\)](#) can be $\sim \lg(\sqrt{3}) \simeq 0.24$ dex lower than that obtained by adopting those of [Lotz et al. \(2011\)](#). Observational uncertainty in the close-pair fractions give an additional scatter of ~ 0.3 dex in the logarithm of the strain.
- The different choices of BH–host galaxy relations contribute to a difference as large as ~ 1 dex in the logarithm of the estimated strain amplitude, as shown in Figure 20.
- The difference in the logarithm of the estimated strain amplitude caused by the different observational galaxy shape distributions of [Padilla & Strauss \(2008\)](#); [Rodríguez & Padilla \(2013\)](#); [Weijmans et al. \(2014\)](#) is $\lesssim 0.15$ dex.
- In this work, the effect of the gas is not considered in the BBH evolution. The gas effect (e.g., [Haiman et al. 2009](#); [Mayer et al. 2007](#)) is negligible in the estimate of the GWB strain at the PTA band, as the GWB at the PTA band is mainly contributed by BBH mergers at $z < 2$ and in high-mass galaxies, which is generally gas-poor. In addition, the triaxiality of galaxy shapes has been shown to be effective enough to decrease the BBH coalescence timescales significantly. For smaller BBHs (e.g., $M_{\text{BH}} \lesssim 10^7 M_{\odot}$), they have relatively high probabilities to be hosted in gas-rich mergers. However, more than half of those BBHs have peak evolution timescales shorter than a few Gyrs, even without considering an acceleration of the merger processes caused by gas (see Figure 9). It is not clear, yet, on how much gas can sink into the vicinity of BBHs in reality and how significant the gas effect can be on

the merger timescales. If a significant amount of gas can sink into the BBH vicinity and accelerate its merging process significantly, the estimation of the surviving fractions and the coalescence rates of those small BBHs deserve further improvements in the future.

There are some other estimates of the stochastic GWB from the cosmic population of BBHs in the literature (e.g., [Kelley et al. 2017](#); [Roebber et al. 2016](#); [Sesana et al. 2016](#); [Ravi et al. 2015](#); [Kulier et al. 2015](#); [McWilliams et al. 2014](#); [Ravi et al. 2014](#)). Below we list some recent estimates of the strain amplitude in the literature, together with some brief descriptions of the astrophysical ingredients implemented in each of those models. The differences in those estimates come from the different uses of the ingredients (such as GSMFs, galaxy merger rates, BBH populations, BBH evolution models, and different numerical simulation results) in the model.

- [Kelley et al. \(2017\)](#) obtain the BBH population based on the Illustris Simulation and implement different binary hardening mechanisms at different BBH separation scales, including dynamical friction on galaxy scales, loss-cone stellar scatterings within parsec scales, viscous drag from a circumbinary disk, and GW emission at smaller scales. In the loss-cone stellar scattering stage, a “refilling fraction” coefficient describing the loss-cone refilling rate compared to the case of full loss-cone refilling is introduced. Within their model implementation, the BBH lifetimes are generally multiple Gyr. As a consequence, only a limited fraction of BBHs could finish final coalescence by $z = 0$, e.g., 45% for BBHs with total masses above $10^8 M_{\odot}$ and mass ratios above 0.2. (Our detailed considerations of the dynamical evolution of BBHs in this work find that according to Fig. 8, for galaxy mergers occurring at $z = 0$ and their BBHs with $M_{\text{BH}} = 10^8 M_{\odot}$ and $q_{\text{BH}} = 0.01$, the fraction of the BBHs with coalescence timescales shorter than the Hubble timescale is $\sim 87\%$ if the shape distribution from [Padilla & Strauss \(2008\)](#) is adopted, and $\sim 75\%$ if the shape distribution from [Weijmans et al. \(2014\)](#) is adopted, according to Fig. 8. For galaxy mergers at $z = 2$ and their corresponding BBHs, the fraction is $\sim 60\%$ if the shape distribution from [Padilla & Strauss \(2008\)](#) is adopted, and $\sim 38\%$ if the shape distribution from [Weijmans et al. \(2014\)](#) is adopted.) Their model taking into account the above hardening mechanisms predicts a strain amplitude of $A_{\text{yr}} = 3.7 \times 10^{-16}$.
- [Roebber et al. \(2016\)](#) also studies the GWB produced by the cosmic population of BBHs, especially on the high-frequency end strain spectral features contributed by a limited number of massive BBHs systems. Their halo merger sample is based on two recent dark matter simulations, i.e., the Dark Sky simulation ([Warren 2013](#)) and the MultiDark simulation ([Riebe et al. 2011](#); [Prada et al. 2012](#)). The halos are then filled with galaxies whose masses are determined based on the galaxy mass–halo mass relation of [Behroozi et al. \(2013\)](#). The GSMFs for galaxies in the two dark matter simulations are

consistent with our model within the mass range $[2 \times 10^{10}, 2 \times 10^{11}]M_{\odot}$, beyond which their GSMFs tend to be lower than the one that we adopt. The MBHs are then assigned to galaxies according to the $M_{\text{BH}} - M_*$ relation of [Kormendy & Ho \(2013\)](#). The BBH coalescence is assumed to occur instantaneously after halo mergers. Their estimated strain amplitude is $A_{\text{yr}} \sim 6-7 \times 10^{-16}$.

- In the estimate of [Sesana et al. \(2016\)](#), four sets of different GSMFs are adopted with equal weights, including those of [Bernardi et al. \(2013\)](#), [Ilbert et al. \(2013\)](#), [Muzzin et al. \(2013\)](#), and [Tomczak et al. \(2014\)](#); and four different sets of close-pair fractions are used, including those of [Bundy et al. \(2009\)](#), [de Ravel et al. \(2009\)](#), [López-Sanjuan et al. \(2012\)](#), and [Xu et al. \(2012\)](#). To convert the close pair fractions into fractional merger rates of galaxies, two sets of observability timescale of galaxy mergers are adopted, including those of [Kitzbichler & White \(2008\)](#) and [Lotz et al. \(2011\)](#). Three sets of the BH–host galaxy relations are used in their model, including the $M_{\text{BH}} - M_*$ relation and the $M_{\text{BH}} - \sigma$ relation of [Kormendy & Ho \(2013\)](#), and the $M_{\text{BH}} - M_* - \sigma$ relation of [Shankar et al. \(2016\)](#). The BBH coalescence is assumed to occur instantaneously after galaxy mergers. With the $M_{\text{BH}} - M_*$ and $M_{\text{BH}} - \sigma$ relations of [Kormendy & Ho \(2013\)](#), their estimated median strain amplitude is $A_{\text{yr}} \sim 1.3 \times 10^{-15}$, and with the BH–host galaxy relation of [Shankar et al. \(2016\)](#), the median value drops by a factor of ~ 3 , decreasing to 4×10^{-16} . Our results obtained by adopting the same $M_{\text{BH}} - M_*$ relation of [Kormendy & Ho \(2013\)](#) is $A_{\text{yr}} \sim 5.0 \times 10^{-16}$ (see [Table 1](#)) and lower than the above $A_{\text{yr}} \sim 1.3 \times 10^{-15}$ estimated by [Sesana et al. \(2016\)](#); the difference may be partly from the difference in the used galaxy merger rates and partly from the delayed BBH coalescence after galaxy merger.
- [Ravi et al. \(2015\)](#) adopts the GSMF of [Muzzin et al. \(2013\)](#) in their fiducial model. The galaxy merger rate in their model is also based on the observational galaxy close-pair counts, i.e., those of [Conselice et al. \(2009\)](#), [Xu et al. \(2012\)](#), and [Robotham et al. \(2014\)](#). Regarding the observability timescale of galaxy mergers, [Ravi et al. \(2015\)](#) adopt the normalization of [Lotz et al. \(2011\)](#) plus the redshift dependence of [Kitzbichler & White \(2008\)](#). The resulting 3 sets of galaxy fractional merger rates adopted by [Ravi et al. \(2015\)](#) are a factor of ~ 3 above that in our model. To convert the bulge masses to the MBH masses, the $M_{\text{BH}} - M_*$ relations of [Kormendy & Ho \(2013\)](#) and [Scott et al. \(2013\)](#) are adopted by [Ravi et al. \(2015\)](#). The BBH coalescence is assumed to occur instantaneously after galaxy mergers. Their estimated strain amplitude is $A_{\text{yr}} \sim 1.3 \times 10^{-15}$ for their fiducial model in which the $M_{\text{BH}} - M_*$ relation of [Kormendy & Ho \(2013\)](#) is chosen. The estimated strain amplitude is already quite close to the current upper limits on the stochastic GWB from the NANOGrav and the IPTA.

7. CONCLUSIONS

We have investigated the evolution of supermassive BBHs in galaxies with realistic property distributions, their statistical distributions, and the GW radiation emitted by their coalescence. In the model, by adopting the observational high-resolution surface brightness profiles of some galaxy samples and the observational galaxy shape distributions, we study the dynamical interactions of the BBHs with their environments and construct the BBH evolution tracks in the realistic galaxy distributions. By incorporating the BBH evolution tracks with the GSMF, galaxy merger rates, the BH–host galaxy relations, effects of multiple galaxy mergers during the evolution of a BBH, we obtain the following main results on the evolution of BBHs, their statistical distributions, and their GW radiation at the PTA and LISA bands.

- Triaxial galaxy shapes, even with a mild triaxiality, can significantly decrease the BBH peak evolution timescale (t_{peak}) after the BBH becomes bound, compared to a nearly spherical, or nearly prolate, or nearly oblate shape (see [Figs 2 and 7](#)), which is consistent with the results in [Yu \(2002\)](#). If the galaxy shape is triaxial and not close to nearly spherical/prolate/oblate, the peak timescale is not sensitive to the value of the triaxiality. The statistical distribution of the BBH coalescence timescales shifts towards longer timescales if the galaxy shape distribution is close to being axisymmetric, compared to the case in triaxial shape distributions (see [Fig. 8](#)), and thus the fractions of the BBHs that can evolve into the PTA band becomes smaller, leading to a lower stochastic GWB amplitude.
- The BBHs formed by local galaxy mergers ($z = 0$) have their coalescence timescales distributing widely from $\sim 10^8$ to $\sim 10^{12}$ yr (see [Fig. 8](#)). High-mass BBHs tend to have a relatively larger fraction with longer τ_0 than low-mass BBHs. Compared BBHs with large mass ratios, BBHs with smaller mass ratios tend to have a larger fraction with longer τ_0 , mainly due to the increased dynamical friction timescales, which is consistent with the study in [Yu \(2002\)](#). Compared with the distribution of $\log \tau_0$, the distribution of the BBH peak timescale after the dynamical friction stage, t_{peak} , is less sensitive to the BBH mass ratios (see [Fig. 9](#)). For low-mass BBHs, their coalescence timescales are relatively longer than their peak timescales after they become bound, which is also mainly due to the significant contribution of the dynamical friction timescale to the coalescence timescales. Overall, the slopes of the BBH evolution curves during the hard binary stage are in the range from -4 to -1 for systems with mass ratio greater than 0.1, not deviating from the value -1 by orders of magnitude, indicating that in most of those cases the stellar refilling rates to the loss cone are not low compared to the rates in the full loss cone case.
- Given the BBH total mass and its mass ratio, the surviving BBHs with large semimajor axes are mainly contributed by those systems which have coalescence timescales longer than the Hubble time and have not reached the gravitational

radiation stage, and the surviving BBHs at the low-semimajor axis end are those being at the gravitational radiation stage and having coalescence timescales shorter than the Hubble time (see Figs. 12). The semimajor axis distribution of the surviving BBHs peaks around the transition to the gravitational radiation stage, where the evolution of most of the BBHs are located at their “bottle-necks”. Below the peak semimajor axis, the distribution decreases with decreasing semimajor axes sharply, following a power law. Above the peak semimajor axis, the distribution decreases with increasing semimajor axes mildly. With increasing the total BBH mass or the BBH mass ratio, the peak of the distribution of surviving BBHs shifts to larger semimajor axes, longer orbital periods, and lower GW frequencies. The semimajor axes of some observational BBH candidates do not locate at the peak locations, which would imply a promising prospect for discovering more BBH candidates. The distributions of surviving BBHs can serve as a guide for searching BBH systems at parsec or sub-parsec separation scales.

- Among the MBHs at galactic centers in the local universe ($z = 0$), the fractions of surviving BBHs with $q_{\text{BH}} > 1/3$ and $a < 10 \text{ pc}$ are expected to $\sim 1\%$ - 3% . At $z = 0$, the fractions of surviving BBHs with $q_{\text{BH}} > 1/3$ and orbital periods $1 \text{ yr} < P < 10 \text{ yr}$ are expected to be $\sim 0.5\%$ - 1% in MBHs with $M_{\text{BH}} \sim 10^6$ - $10^7 M_{\odot}$. The fractions of those with $1 \text{ yr}^{-1} < P < 30 \text{ yr}^{-1}$ are expected to be $\sim 2\%$ in MBHs with $M_{\text{BH}} \sim 10^6$ - $10^7 M_{\odot}$, and the fractions decrease in MBHs with other masses, down to 10^{-4} for $M_{\text{BH}} \sim 10^9 M_{\odot}$. The fractions are not sensitive to redshifts at $z \lesssim 3$. The fractions of surviving BBHs can increase to $\sim 10\%$ for $q_{\text{BH}} > 1/100$.
- The time delays between host galaxy mergers and embedded BBH coalescences decrease the BBH coalescence rates at high redshifts while increase them at low redshifts, compared to the results obtained by assuming instantaneous BBH coalescences (see Fig. 17). This effect is significant especially for BBHs with smaller mass ratios, as BBHs with smaller mass ratios tend to have relatively longer coalescence timescales. The BBH coalescence rates obtained by using different sets of the BH–host galaxy relations differ a lot, up to ~ 2 orders of magnitude (see Fig. 18).
- The stochastic GWB strain spectrum around the PTA band contributed by the cosmic population of BBHs is estimated, and the effects of the physical ingredients involved in the estimation are discussed. The strain spectrum has a peak or turnover at the frequency $\sim 0.25 \text{ nHz}$. The spectrum follows a power law $\propto f^{-2/3}$ at frequencies higher than the turnover frequency, unless the frequencies are high enough so that the number of contributing sources is too small to have a significantly statistical estimate. And the spectrum declines with decreasing frequencies with an exponent of

$$-\frac{2}{3} + \frac{\kappa_{\text{gw}}}{2} \sim 1.2 \pm 0.2 \text{ at frequencies lower than the turnover frequency.}$$

- Using different BH–host galaxy relations in the model can lead to the difference in the GWB strain amplitude by one order of magnitude (see Fig. 19). At frequency 1 yr^{-1} , the median value of the characteristic strain amplitudes A_{yr} obtained with the different BH–host galaxy relations is $A_{\text{yr}} \sim 2.0 \times 10^{-16}$, the maximum value is $A_{\text{yr}} \sim 5.4 \times 10^{-16}$ obtained with the $M_{\text{BH}}-M_*$ relation of Kormendy & Ho (2013), and the minimum one is $A_{\text{yr}} \sim 6.1 \times 10^{-17}$ obtained with the $M_{\text{BH}}-M_*-\sigma$ relation of Shankar et al. (2016). The maximum and the median values are below the current upper limit set by the PTA experiments by a factor of ~ 2 and ~ 5 , respectively. Our estimate is lower than previous estimates by a factor of ~ 1.5 - 3 , partly due to the different choices of galaxy merger rates, and partly due to the inclusion of the time delay between BBH coalescences and galaxy mergers. The GWB strain amplitudes at a little lower frequency $\sim 10 \text{ nHz}$ are expected to be within the detection ability of future experiments (e.g., SKA, ngVLA).
- The above estimates obtained with including the BBH orbital evolution and the time delays between host galaxy mergers and BBH coalescence has decreased the estimated strain amplitude by ~ 0.1 - 0.2 dex, compared to the estimates obtained with an instantaneous BBH coalescence assumption. The above estimates are obtained by adopting the galaxy shape distributions in Padilla & Strauss (2008) or Rodríguez & Padilla (2013) is adopted, which prefers triaxial configurations. If the galaxy shape distribution of Weijmans et al. (2014) is adopted, which prefers axisymmetric configurations, the estimated strain amplitudes will decrease by another ~ 0.15 dex.
- At frequencies $f \gtrsim 10^{-8} \text{ Hz}$, the GWB strain spectrum deviates to below the $-2/3$ power law and fluctuates due to the small number of BBH sources at the high-frequency end. The prospect of detecting GW signals from individual BBH systems around the PTA band is studied, through simulating the cosmic BBH populations in our model (see Fig. 20). According to the simulated realizations, it is found that the majority of individual sources with signals higher than the stochastic backgrounds are located at frequencies $\gtrsim 10^{-8} \text{ Hz}$. The loudest signals located at 10^{-8} - 10^{-7} Hz have BBH masses higher than $\sim 10^9 M_{\odot}$, and redshifts $z \lesssim 1$, and their strain amplitudes are lower than the best constraints of current PTAs on continuous individual sources by about one order of magnitude.
- Finally, we extend the investigation of GW radiation from the cosmic population of BBHs to the LISA detection bands. Based on our realizations of the BBH populations, the detection rate of this population is predicted to be $\sim 0.9 \text{ yr}^{-1}$, which sets the lower limit for the LISA detection rates.

We thank Scott Tremaine for helpful discussions. This work was supported in part by the National Natural Science Foundation of China under Nos. 11673001, 11273004, 10973001, 11690024, 11873056, 11721303, the National Key R&D Program of China (Grant Nos. 2016YFA0400703, 2016YFA0400704), the Strategic Priority Program of the Chinese Academy of Sciences (Grant No. XDB 23040100), and National Supercomputer Center in Guangzhou, China.

REFERENCES

- Aggarwal, K., Arzoumanian, Z., Baker, P. T., et al. 2018, [arXiv e-prints](#), [arXiv:1812.11585](#).
- Amaro-Seoane, P., Eichhorn, C., Porter, E. K., & Spurzem, R. 2010, *MNRAS*, **401**, 2268
- Amaro-Seoane, P., Audley, H., Babak, S., et al. 2017, [arXiv e-prints](#), [arXiv:1702.00786](#).
- Arzoumanian, Z., Brazier, A., Burke-Spolaor, S., et al. 2014, *ApJ*, **794**, 141
- Arzoumanian, Z., Brazier, A., Burke-Spolaor, S., et al. 2016, *ApJ*, **821**, 13
- Arzoumanian, Z., Baker, P. T., Brazier, A., et al. 2018, *ApJ*, **859**, 47.
- Babak, S., & Sesana, A. 2012, *Phys. Rev. D*, **85**, 044034
- Babak, S., Petiteau, A., Sesana, A., et al. 2016, *MNRAS*, **455**, 1665
- Baker, R. M. L., Jr. 2006, *Astronomische Nachrichten*, **327**, 710
- Begelman, M. C., Blandford, R. D., & Rees, M. J. 1980, *Nature*, **287**, 307
- Behroozi, P. S., Wechsler, R. H., & Conroy, C. 2013, *ApJ*, **770**, 57
- Behroozi, P., Wechsler, R. H., Hearin, A. P., et al. 2019, *MNRAS*, **488**, 3143
- Beifiori, A., Courteau, S., Corsini, E. M., & Zhu, Y. 2012, *MNRAS*, **419**, 2497
- Benson, A., Holley-Bockelmann, K., & Gültekin, K. 2010, *Bulletin of the American Astronomical Society*, **42**, 404.16
- Berczik, P., Merritt, D., Spurzem, R., & Bischof, H.-P. 2006, *ApJ*, **642**, L21
- Bernardi, M., Meert, A., Sheth, R. K., et al. 2013, *MNRAS*, **436**, 697
- Bevington, P. R., & Robinson, D. K. 2003, Data reduction and error analysis for the physical sciences, 3rd ed., by Philip R. Bevington, and Keith D. Robinson. Boston, MA: McGraw-Hill, ISBN 0-07-247227-8, 2003
- Binney, J., & Merrifield, M. 1998, Galactic astronomy / James Binney and Michael Merrifield. Princeton
- Binney, J., & Tremaine, S. 2008, Galactic Dynamics: Second Edition, by James Binney and Scott Tremaine. ISBN 978-0-691-13026-2 (HB). Published by Princeton University Press, Princeton, NJ USA, 2008.
- Bonetti, M., Sesana, A., Barausse, E., et al. 2018, *MNRAS*, **477**, 2599.
- Boyle, L., & Pen, U.-L. 2012, *Phys. Rev. D*, **86**, 124028
- Bundy, K., Fukugita, M., Ellis, R. S., et al. 2009, *ApJ*, **697**, 1369
- Cappellari, M., Emsellem, E., Krajnović, D., et al. 2011, *MNRAS*, **413**, 813
- Cappellari, M., Scott, N., Alatalo, K., et al. 2013, *MNRAS*, **432**, 1709
- Chen, S., Sesana, A., & Del Pozzo, W. 2016, [arXiv:1612.00455](#)
- Conselice, C. J., Yang, C., & Bluck, A. F. L. 2009, *MNRAS*, **394**, 1956
- Conselice, C. J., Bluck, A. F. L., Mortlock, A., Palamara, D., & Benson, A. J. 2014, *MNRAS*, **444**, 1125
- Cui, X., & Yu, Q. 2014, *MNRAS*, **437**, 777
- de Ravel, L., Le Fèvre, O., Tresse, L., et al. 2009, *A&A*, **498**, 379
- Desvignes, G., Caballero, R. N., Lentati, L., et al. 2016, *MNRAS*, **458**, 3341
- Ellis, J. A., Siemens, X., & Creighton, J. D. E. 2012, *ApJ*, **756**, 175
- Emsellem, E., Cappellari, M., Krajnović, D., et al. 2007, *MNRAS*, **379**, 401
- Ferrarese, L., & Merritt, D. 2000, *ApJ*, **539**, L9
- Gallazzi, A., Charlot, S., Brinchmann, J., & White, S. D. M. 2006, *MNRAS*, **370**, 1106
- Gebhardt, K., Bender, R., Bower, G., et al. 2000, *ApJ*, **539**, L13
- Graham, A. W., Onken, C. A., Athanassoula, E., & Combes, F. 2011, *MNRAS*, **412**, 2211
- Graham, A. W., & Scott, N. 2013, *ApJ*, **764**, 151
- Graham, M. J., Djorgovski, S. G., Stern, D., et al. 2015, *Nature*, **518**, 74
- Gültekin, K., Richstone, D. O., Gebhardt, K., et al. 2009, *ApJ*, **698**, 198
- Guo, Q., White, S., Boylan-Kolchin, M., et al. 2011, *MNRAS*, **413**, 101
- Haiman, Z., Kocsis, B., & Menou, K. 2009, *ApJ*, **700**, 1952
- Häring, N., & Rix, H.-W. 2004, *ApJ*, **604**, L89
- Heggie, D. C. 1975, *MNRAS*, **173**, 729
- Hinshaw G. et al., 2013, *ApJS*, **208**, 19
- Hobbs, G. 2013, *Classical and Quantum Gravity*, **30**, 224007
- Holley-Bockelmann, K., & Khan, F. M. 2015, *ApJ*, **810**, 139
- Hopkins, P. F., Bundy, K., Croton, D., et al. 2010, *ApJ*, **715**, 202
- Hopkins, P. F., Croton, D., Bundy, K., et al. 2010, *ApJ*, **724**, 915
- Ilbert, O., McCracken, H. J., Le Fèvre, O., et al. 2013, *A&A*, **556**, A55
- Katz, M. L., Kelley, L. Z., Dosopoulou, F., et al. 2019, *MNRAS*, **2700**
- Kelley, L. Z., Blecha, L., Hernquist, L., Sesana, A., & Taylor, S. R. 2017, *MNRAS*, **471**, 4508
- Kelley, L. Z., Blecha, L., Hernquist, L., Sesana, A., & Taylor, S. R. 2018, *MNRAS*, **477**, 964
- Kelvin, L. S., Driver, S. P., Robotham, A. S. G., et al. 2014, *MNRAS*, **444**, 1647
- Khan, F. M., Just, A., & Merritt, D. 2011, *ApJ*, **732**, 89
- Khan, F. M., Holley-Bockelmann, K., Berczik, P., & Just, A. 2013, *ApJ*, **773**, 100
- Kitzbichler, M. G., & White, S. D. M. 2008, *MNRAS*, **391**, 1489
- Kormendy, J., & Ho, L. C. 2013, *ARA&A*, **51**, 511
- Krajnović, D., Emsellem, E., Cappellari, M., et al. 2011, *MNRAS*, **414**, 2923
- Krajnović, D., Karick, A. M., Davies, R. L., et al. 2013, *MNRAS*, **433**, 2812
- Kulier, A., Ostriker, J. P., Natarajan, P., et al. 2015, *ApJ*, **799**, 178
- Lackner, C. N., Cen, R., Ostriker, J. P., et al. 2012, *MNRAS*, **425**, 641
- Lauer, T. R., Ajhar, E. A., Byun, Y.-I., et al. 1995, *AJ*, **110**, 2622
- Lauer, T. R., Gebhardt, K., Faber, S. M., et al. 2007, *ApJ*, **664**, 226
- Lauer, T. R., Faber, S. M., Richstone, D., et al. 2007, *ApJ*, **662**, 808
- Lee, K. J., Wex, N., Kramer, M., et al. 2011, *MNRAS*, **414**, 3251
- Lentati, L., Taylor, S. R., Mingarelli, C. M. F., et al. 2015, *MNRAS*, **453**, 2576
- Lim, S. H., Mo, H. J., Lan, T.-W., & Ménard, B. 2017, *MNRAS*, **464**, 3256
- López-Sanjuan, C., Le Fèvre, O., Ilbert, O., et al. 2012, *A&A*, **548**, A7
- Lotz, J. M., Jonsson, P., Cox, T. J., et al. 2008, *MNRAS*, **391**, 1137
- Lotz, J. M., Jonsson, P., Cox, T. J., & Primack, J. R. 2010, *MNRAS*, **404**, 575
- Lotz, J. M., Jonsson, P., Cox, T. J., et al. 2011, *ApJ*, **742**, 103
- Magorrian, J., Tremaine, S., Richstone, D., et al. 1998, *AJ*, **115**, 2285
- Magorrian, J., & Tremaine, S. 1999, *MNRAS*, **309**, 447
- Mayer, L., Kazantzidis, S., Madau, P., et al. 2007, *Science*, **316**, 1874
- McConnell, N. J., & Ma, C.-P. 2013, *ApJ*, **764**, 184
- McLaughlin, M. A. 2013, *Classical and Quantum Gravity*, **30**, 224008
- McWilliams, S. T., Ostriker, J. P., & Pretorius, F. 2014, *ApJ*, **789**, 156
- Milosavljević, M., & Merritt, D. 2001, *ApJ*, **563**, 34
- Mingarelli, C. M. F., Lazio, T. J. W., Sesana, A., et al. 2017, *Nature Astronomy*, **1**, 886.
- Moore, C. J., Cole, R. H., & Berry, C. P. L. 2015, *Classical and Quantum Gravity*, **32**, 015014
- Muzzin, A., Marchesini, D., Stefanon, M., et al. 2013, *ApJ*, **777**, 18
- NANOGrav Collaboration 2018, [ArXiv e-prints](#), [arXiv:1810.06594](#).

- Padilla, N. D., & Strauss, M. A. 2008, *MNRAS*, **388**, 1321
- Peters, P. C., & Mathews, J. 1963, *Physical Review*, **131**, 435
- Peters, P. C. 1964, *Physical Review*, **136**, 1224
- Phinney, E. S. 2001, [arXiv:astro-ph/0108028](https://arxiv.org/abs/astro-ph/0108028)
- Planck Collaboration XIII, 2016, *A&A*, **594**, A13
- Polnarev, S., & Rees, M. J. 1994, *A&A*, **283**, 301
- Prada, F., Klypin, A. A., Cuesta, A. J., et al. 2012, *MNRAS*, **423**, 3018
- Preto, M., Berentzen, I., Berczik, P., & Spurzem, R. 2011, *ApJ*, **732**, L2
- Qu, Y., Helly, J. C., Bower, R. G., et al. 2017, *MNRAS*, **464**, 1659
- Quinlan, G. D. 1996, *New Astronomy*, **1**, 35
- Quinlan, G. D., & Hernquist, L. 1997, *New Astronomy*, **2**, 533
- Ravi, V., Wyithe, J. S. B., Hobbs, G., et al. 2012, *ApJ*, **761**, 84
- Ravi, V., Wyithe, J. S. B., Shannon, R. M., et al. 2014, *MNRAS*, **442**, 56
- Ravi, V., Wyithe, J. S. B., Shannon, R. M., & Hobbs, G. 2015, *MNRAS*, **447**, 2772
- Riebe, K., Partl, A. M., Enke, H., et al. 2011, [arXiv e-prints](https://arxiv.org/abs/1109.0003), [arXiv:1109.0003](https://arxiv.org/abs/1109.0003)
- Robotham, A. S. G., Driver, S. P., Davies, L. J. M., et al. 2014, *MNRAS*, **444**, 3986
- Rodríguez, S., & Padilla, N. D. 2013, *MNRAS*, **434**, 2153
- Rodríguez-Gomez, V., Genel, S., Vogelsberger, M., et al. 2015, *MNRAS*, **449**, 49
- Roebber, E., Holder, G., Holz, D. E., & Warren, M. 2016, *ApJ*, **819**, 163
- Rosado, P. A., Sesana, A., & Gair, J. 2015, *MNRAS*, **451**, 2417
- Ruan, W.-H., Guo, Z.-K., Cai, R.-G., et al. 2018, [arXiv e-prints](https://arxiv.org/abs/1807.09495), [arXiv:1807.09495](https://arxiv.org/abs/1807.09495)
- Ruan, W.-H., Liu, C., Guo, Z.-K., et al. 2019, [arXiv e-prints](https://arxiv.org/abs/1909.07104), [arXiv:1909.07104](https://arxiv.org/abs/1909.07104)
- Salcido, J., Bower, R. G., Theuns, T., et al. 2016, *MNRAS*, **463**, 870.
- Sani, E., Marconi, A., Hunt, L. K., & Risaliti, G. 2011, *MNRAS*, **413**, 1479
- Schaye, J., Crain, R. A., Bower, R. G., et al. 2015, *MNRAS*, **446**, 521
- Schutz, B. F. 2011, *Classical and Quantum Gravity*, **28**, 125023
- Scott, N., Graham, A. W., & Schombert, J. 2013, *ApJ*, **768**, 76
- Sesana, A., Volonteri, M., & Haardt, F. 2007, *MNRAS*, **377**, 1711
- Sesana, A., Vecchio, A., & Volonteri, M. 2009, *MNRAS*, **394**, 2255
- Sesana, A., Gualandris, A., & Dotti, M. 2011, *MNRAS*, **415**, L35
- Sesana, A. 2013, *MNRAS*, **433**, L1
- Sesana, A., Shankar, F., Bernardi, M., & Sheth, R. K. 2016, [arXiv:1603.09348](https://arxiv.org/abs/1603.09348)
- Shankar, F., Bernardi, M., Sheth, R. K., et al. 2016, *MNRAS*, **460**, 3119
- Shannon, R. M., Ravi, V., Lentati, L. T., et al. 2015, *Science*, **349**, 1522
- Sijacki, D., Vogelsberger, M., Genel, S., et al. 2015, *MNRAS*, **452**, 575
- Snyder, G. F., Lotz, J. M., Rodriguez-Gomez, V., et al. 2017, *MNRAS*, **468**, 207
- Somerville, R. S., Hopkins, P. F., Cox, T. J., Robertson, B. E., & Hernquist, L. 2008, *MNRAS*, **391**, 481
- Springel, V. 2005, *MNRAS*, **364**, 1105
- Stone, N. C., & Metzger, B. D. 2016, *MNRAS*, **455**, 859
- Tomczak, A. R., Quadri, R. F., Tran, K.-V. H., et al. 2014, *ApJ*, **783**, 85
- Torrey, P., Wellons, S., Machado, F., et al. 2015, *MNRAS*, **454**, 2770
- Tremaine, S., Gebhardt, K., Bender, R., et al. 2002, *ApJ*, **574**, 740
- Valtonen, M. J., Lehto, H. J., Nilsson, K., et al. 2008, *Nature*, **452**, 851
- van den Bosch, R. C. E. 2016, *ApJ*, **831**, 134
- Vasiliev, E., Antonini, F., & Merritt, D. 2015, *ApJ*, **810**, 49
- Verbiest, J. P. W., Lentati, L., Hobbs, G., et al. 2016, *MNRAS*, **458**, 1267
- Vincent, R. A., & Ryden, B. S. 2005, *ApJ*, **623**, 137
- Vogelsberger, M., Genel, S., Springel, V., et al. 2014, *MNRAS*, **444**, 1518
- Wang, H.-T., Jiang, Z., Sesana, A., et al. 2019, *Phys. Rev. D*, **100**, 043003
- Warren, M. S. 2013, [arXiv e-prints](https://arxiv.org/abs/1310.4502), [arXiv:1310.4502](https://arxiv.org/abs/1310.4502)
- Weijmans, A.-M., de Zeeuw, P. T., Emsellem, E., et al. 2014, *MNRAS*, **444**, 3340
- Wyithe, J. S. B., & Loeb, A. 2003, *ApJ*, **590**, 691
- Xu, C. K., Zhao, Y., Scoville, N., et al. 2012, *ApJ*, **747**, 85
- Yan, C.-S., Lu, Y., Dai, X., & Yu, Q. 2015, *ApJ*, **809**, 117
- Yu, Q. 2002, *MNRAS*, **331**, 935
- Zhu, X.-J., Hobbs, G., Wen, L., et al. 2014, *MNRAS*, **444**, 3709

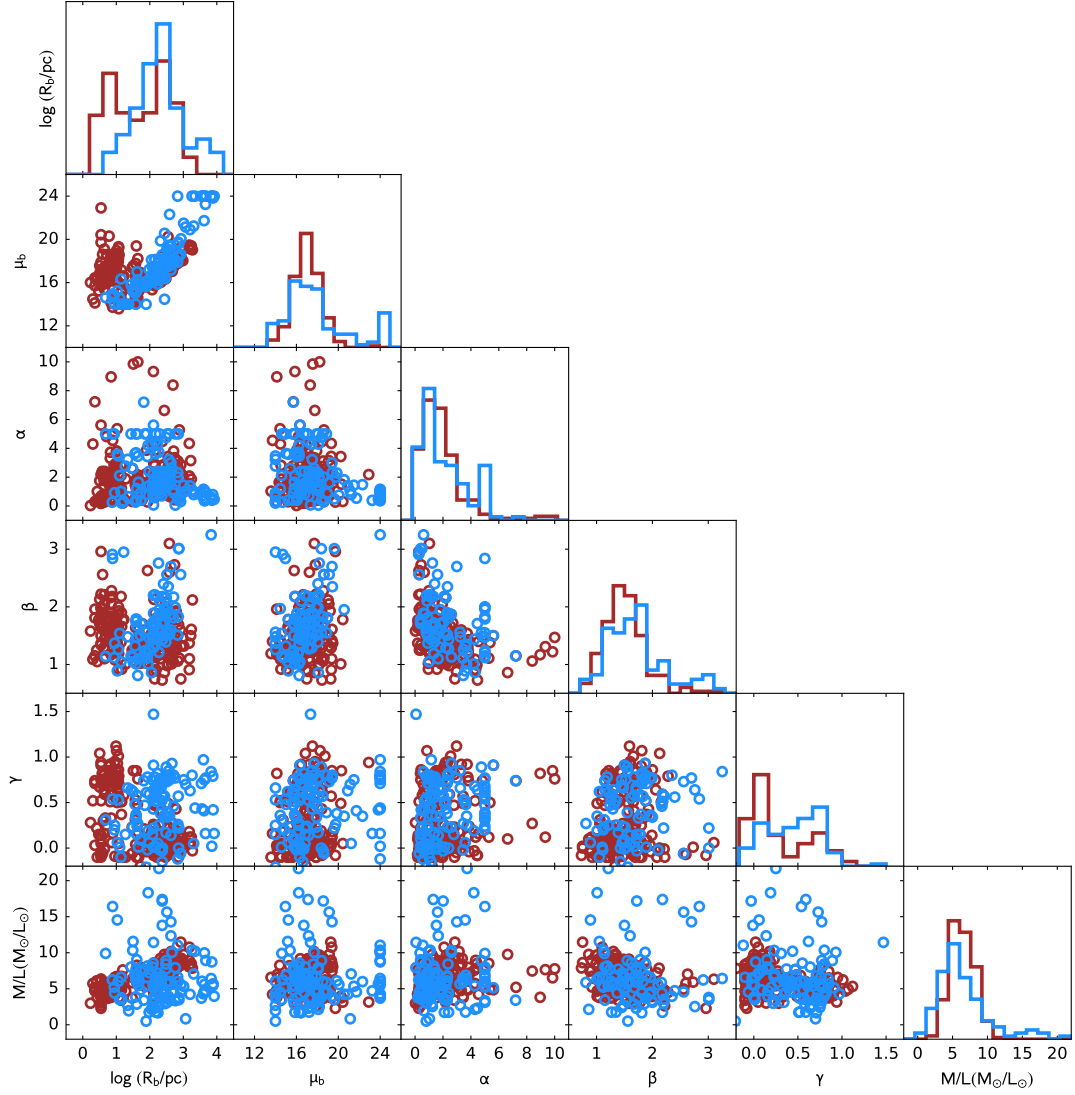


Figure 1. Distributions of the galaxy properties for the galaxies from the ATLAS^{3D} (Cappellari et al. 2011) sample (blue) and Lauer et al. (2007a) sample (red). The parameters shown in the figure include the five “Nuker law” parameters (i.e., break radius R_b , surface brightness at break radius μ_b , α , β , γ ; see Eq. 39) and mass-to-light ratio M/L in the V band. Each circle represents one galaxy, and the solid lines represent the histograms of the corresponding parameters. See Section 4.1.1.

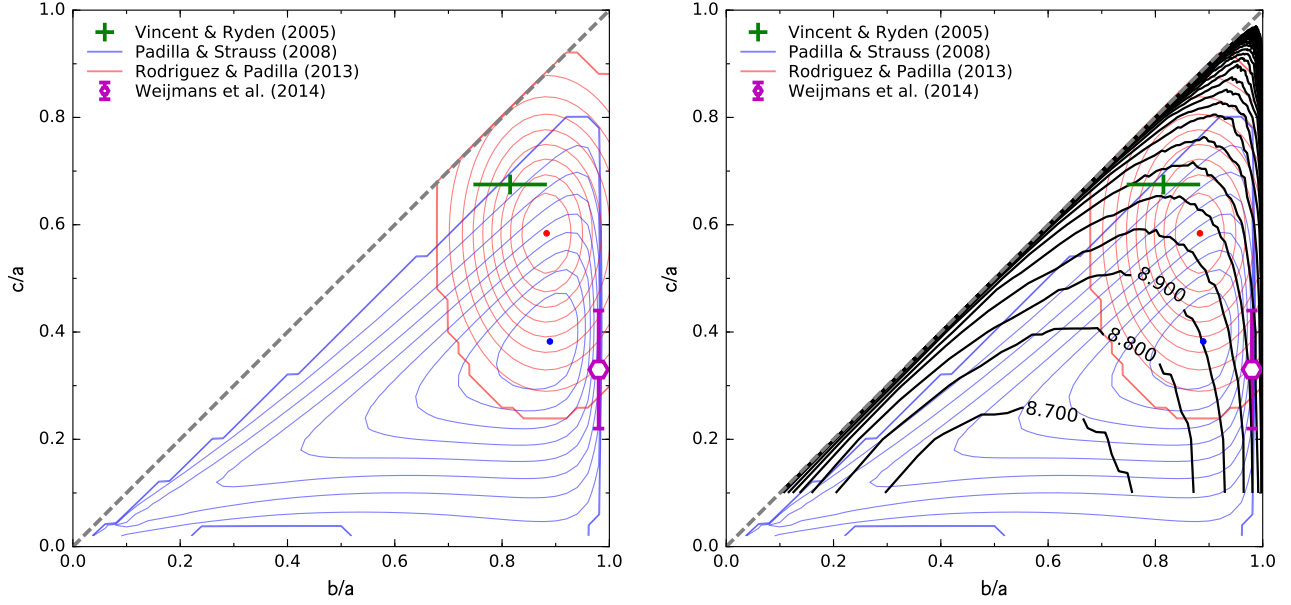


Figure 2. The left panel shows the observational shape distributions of early-type galaxies, based on the different works labeled by the texts. The blue and red contours show the probability distributions obtained in Padilla & Strauss (2008) and Rodríguez & Padilla (2013), respectively, and the contour levels decrease from the center to the outer parts by an interval of 10% of the maximum of the corresponding probability distribution. The green plus symbol marks the possible ranges of the mean medium-to-major and minor-to-major axis ratios of the early-type galaxies in the SDSS DR3 data set, obtained in (Vincent & Ryden 2005), and the ranges are converted from their constraints on the triaxiality and the minor-to-major axis ratio of the bright galaxies sample with a de Vaucouleurs profile therein. For Weijmans et al. (2014), only the best fitting results for their fast-rotator galaxies are shown, whose shape distribution is consistent with an almost oblate sample; and the magenta point and the error bar show the mean value and the standard deviation of their c/a ratios. The right panel shows the dependence of the peak timescale of the BBH evolution on galaxy shapes. The thick black curves represent the contours of $\log(t_{\text{peak}}/\text{yr})$ of a BBH system (with $q_{\text{BH}} = 1$) after becoming bound in the example galaxy shown in Figure 6. The values labeled for the corresponding black curves are $\log(t_{\text{peak}}/\text{yr})$ calculated from the BBH evolution model presented in Section 2, with an interval level of 0.1 dex. This figure shows that even a mild triaxiality can decrease t_{peak} significantly (see also Fig. 2 below). See details in Sections 4.1.2 and 5.1.

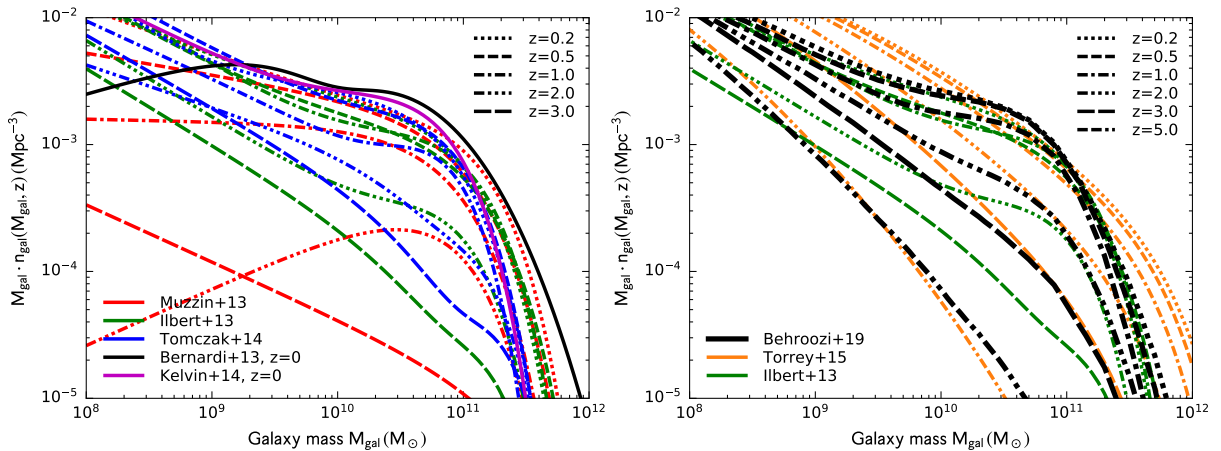


Figure 3. Galaxy stellar mass functions $n_{\text{gal}}(M_{\text{gal}}, z)$ obtained from both observations and hydrodynamical simulations (see Section 4.3.1). The vertical axis represents $M_{\text{gal}} \cdot n_{\text{gal}}(M_{\text{gal}}, z)$. The left panels show the observational GSMFs. The black and the magenta curves correspond to the local ($z = 0$) GSMFs obtained from Bernardi et al. (2013) and Kelvin et al. (2014), respectively. The red curves show the GSMFs from Muzzin et al. (2013); and the different line styles represent the different redshifts ($z = 0.2, 0.5, 1.0, 2.0, 3.0$), as labeled by the texts. The green and the blue curves show the results from Ilbert et al. (2013) and Tomczak et al. (2014), respectively. The right panel shows the GSMFs used in this work, which is from Behroozi et al. (2019) (black). The GSMFs from the observational results in Ilbert et al. (2013) (green) and the Illustris simulation results in Torrey et al. (2015) (orange) are also shown in the panel for comparison. The differences in the stochastic GWB strain amplitude caused by using the different GSMFs are discussed in Section 6.

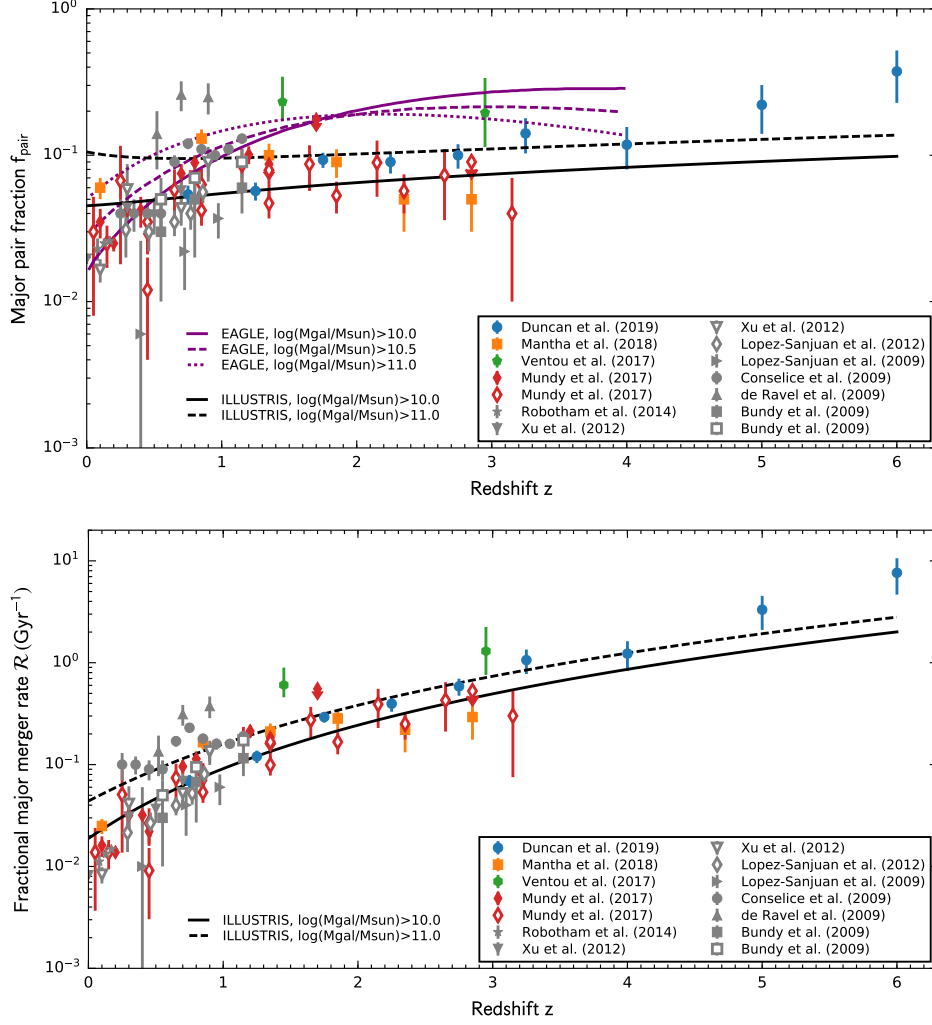


Figure 4. Galaxy major pair fractions f_{pair} (upper panel) and fractional major merger rates $\mathcal{R}(> M_{\text{gal}}, z)$ (lower panel) as a function of redshift z (see Eqs. 41 and 42), which are converted from both hydrodynamical simulations and observational results. In the upper panel, the grey symbols show the close pair fraction of galaxies obtained from the observational samples at $z \lesssim 1$, and the other color symbols show some recent observational results that extend to high redshift $z \gtrsim 3$, as labeled by their references. Those observational results are based on close pair counts or the morphological disturbance. The filled and the empty symbols correspond to the samples of galaxies with $M_{\text{gal}} \gtrsim 10^{10} M_{\odot}$ and $M_{\text{gal}} \gtrsim 10^{11} M_{\odot}$, respectively. Note that besides the difference in total masses, the different samples have different cut criteria on the maximum projected separation and velocity difference between two galaxy members in a pair. The black curves show the close pair fraction of galaxies with total mass greater than $10^{10} M_{\odot}$ (solid) and $10^{11} M_{\odot}$ (dashed), obtained by the product of the galaxy fractional major merger rate from Rodriguez-Gomez et al. (2015) and the average observability timescale of galaxy mergers from Snyder et al. (2017) (both based on the results of the Illustris Project described in Vogelsberger et al. 2014). Here $C_{\text{mrg}} = 1.0$ is assumed in Equation (41), and only the major pairs with $q_{\text{gal}} \geq q_{\text{major}} = 1/4$ (see Eq. 42) are considered. The purple curves correspond to the close pair fraction of the galaxies with total mass greater than $10^{10} M_{\odot}$ (solid), $10^{10.5} M_{\odot}$ (dashed) and $10^{11} M_{\odot}$ (dotted), respectively, as shown in Qu et al. (2017), which is based on the EAGLE simulation (Schaye et al. 2015). In the lower panel, the black curves show the fractional galaxy merger rates obtained from the numerical simulations in Rodriguez-Gomez et al. (2015), and the observational symbols are converted from the corresponding symbols of close-pair fractions in the upper panel and the average observability timescale of galaxy mergers obtained from Snyder et al. (2017) (see Eq. 41). This figure illustrates the uncertainty in the close-pair fraction, the fractional merger rate of galaxies and their dependence on the redshift, from both observations and hydrodynamical simulations. This figure shows that the fractional galaxy merger rates obtained from Rodriguez-Gomez et al. (2015) is close to the observational one converted by using Equation (45) (which evolves with redshift strongly).

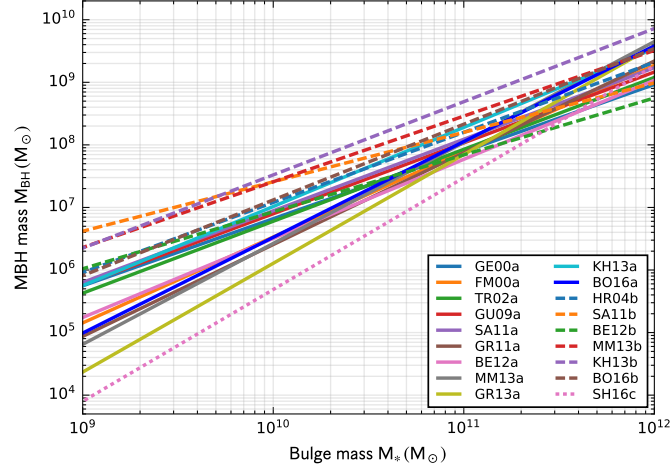


Figure 5. Different BH–host galaxy relations used in this study, expressed through the relations between the MBH masses and the masses of the spheroidal components of the host galaxies. The solid, the dashed, and the dotted lines represent the relations converted from the $M_{\text{BH}} - \sigma$, the $M_{\text{BH}} - M_*$, and the $M_{\text{BH}} - M_* - \sigma$ relations shown by Equation (46), respectively. Different lines represent the different works as labeled by the texts (see also Table 1). The $M_{\text{BH}} - M_*$ relations shown by Equation (46) are drawn in this figure directly, and the $M_{\text{BH}} - \sigma$ and the $M_{\text{BH}} - M_* - \sigma$ relations are converted to the $M_{\text{BH}} - M_*$ relation by applying the relation between σ and M_* obtained in Gallazzi et al. (2006). See Section 4.4.

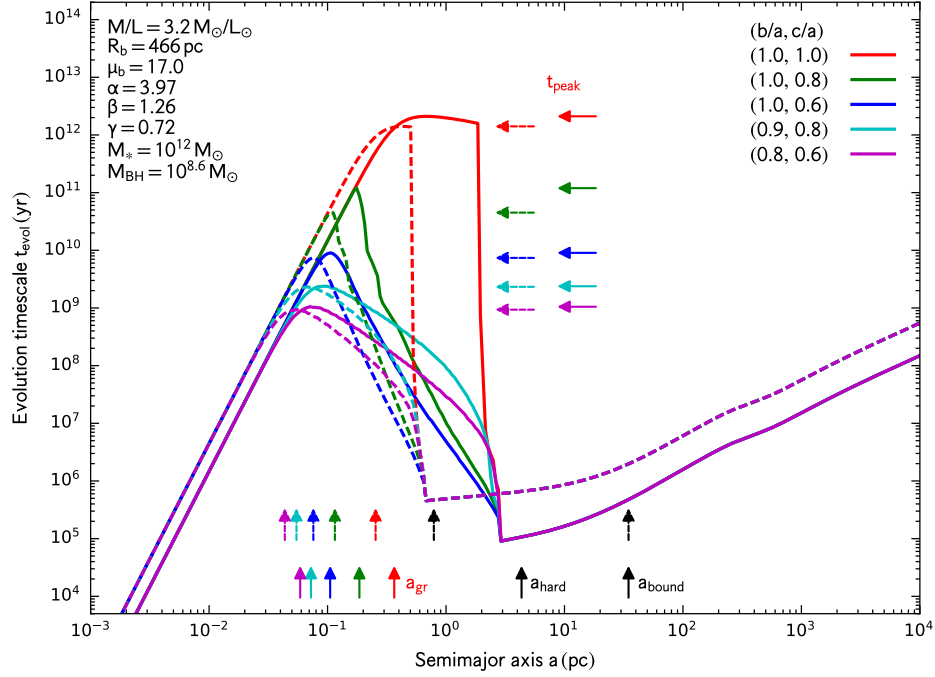


Figure 6. Examples of the evolution tracks of BBHs in a galaxy, with different assumed BBH mass ratios and merger remnant shapes. The radial surface brightness of the spheroidal component of this galaxy is described by the Nuker-law profile with parameters $R_b = 466$ pc, $\mu_b = 17.0$, $\alpha = 3.97$, $\beta = 1.26$, $\gamma = 0.72$, and the mass-to-light ratio in the V band $M/L = 3.2 M_\odot/L_\odot$. The total stellar mass of the merger remnant is $10^{12} M_\odot$ and the total mass of the BBH is $10^{8.6} M_\odot$. The solid and the dashed curves correspond to the cases with the assumed BBH mass ratio $q_{\text{BH}} = 1$ and 0.1 , respectively. The different colors represent the assumed different shapes of the galaxy merger remnant, i.e., red for $(b/a, c/a) = (1.0, 1.0)$, green for $(1.0, 0.8)$, blue for $(1.0, 0.6)$, cyan for $(0.9, 0.8)$, and magenta for $(0.8, 0.6)$, where b/a and c/a correspond to the medium-to-major and the minor-to-major axis ratios of the mass density distribution. The vertical arrows at the bottom of the figure mark the semimajor axes at which the BBH enters the gravitational radiation stage for the corresponding evolution curves with the same colors, and the horizontal arrows mark the peak evolution timescales after the BBH becomes hard for the corresponding evolution curves with the same colors. See Section 5.1.

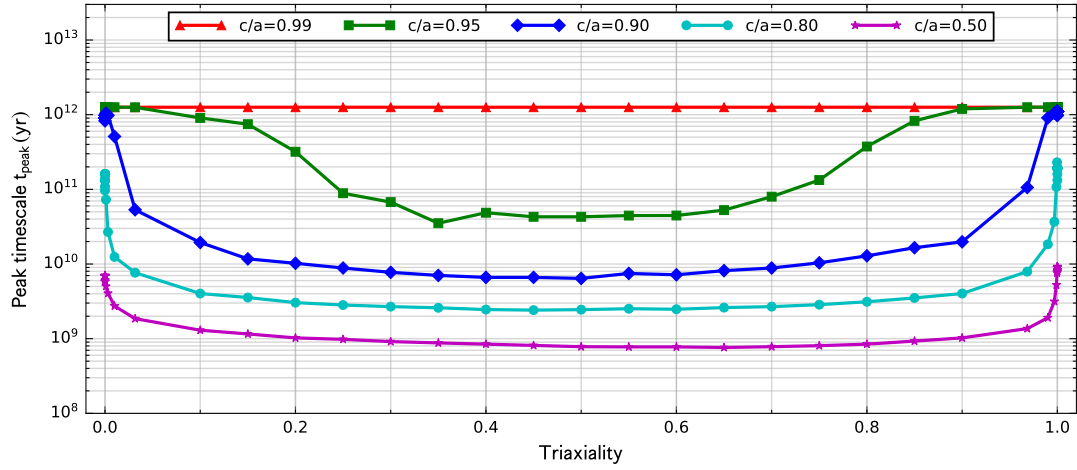


Figure 7. The dependence of the peak timescale t_{peak} on the triaxiality parameter $T = (a^2 - b^2)/(a^2 - c^2)$ for the same BBH system shown in Figure 2. Different curves show the results obtained with the different sets of the minor-to-major axis ratios c/a of the mass density distribution of the host merger remnant. The sharp decrease of t_{peak} at $T \sim 0$ and 1 is consistent with those shown in Figure 2.

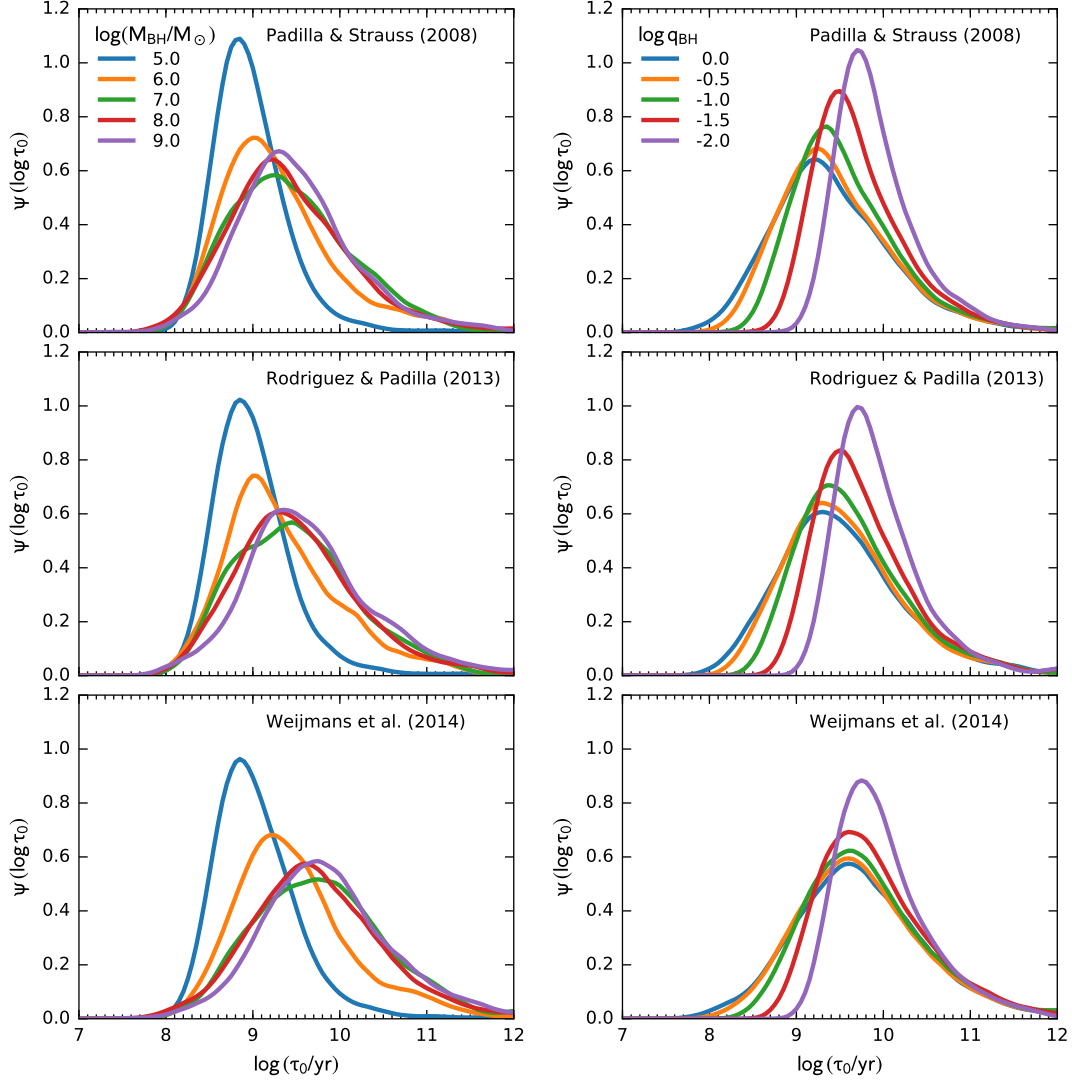


Figure 8. Probability distributions of the logarithm of the coalescence timescale $\log \tau_0$ (cf. Equation 48) of a population of BBHs whose host galaxies merge at redshift $z' = 0$, $\psi_{\log \tau_0}(\log \tau_0 | M_{\text{BH}}, q_{\text{BH}}, z' = 0)$, and their dependence on the properties of the BBHs and their host galaxies. The left panels show the distributions of $\log(\tau_0/\text{yr})$ for BBHs with mass ratio $q_{\text{BH}} = 1.0$ and with different total masses M_{BH} (shown by different colors), which suggest that the BBHs with high total masses (e.g., $\sim 10^9$ - $10^{10} M_{\odot}$) have a relatively large fraction of long τ_0 (e.g., longer than the Hubble timescale $\sim 10^{10}$ yr). The right panel shows the distributions of $\log(\tau_0/\text{yr})$ for BBHs with total mass $M_{\text{BH}} = 10^8 M_{\odot}$ and with different mass ratios q_{BH} , which suggest that the BBHs with smaller BH mass ratios (e.g., $q_{\text{BH}} = 0.01$) have a relatively larger fraction of long τ_0 . The different rows represent the results obtained with the shape distributions of early-type galaxies in the different works, i.e., Weijmans et al. (2014), Rodríguez & Padilla (2013), and Padilla & Strauss (2008) from top to bottom panels, respectively. The distributions obtained with triaxial shape distributions in the top and the middle panels are close to each other, and the distributions obtained with nearly oblate shape distribution in the bottom panel are relatively broadened towards longer τ_0 . See Section 5.2.

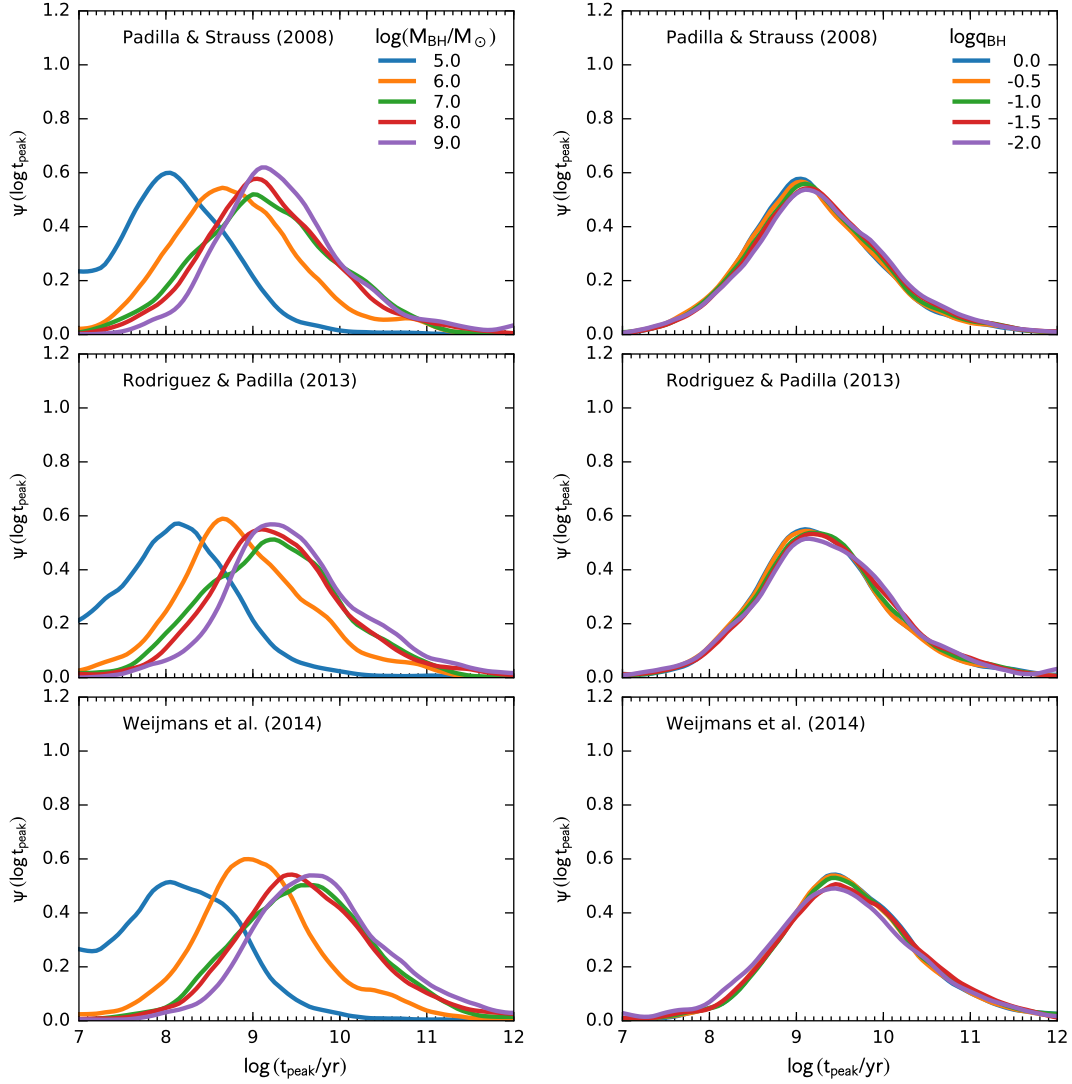


Figure 9. Probability distributions of the logarithm of the timescale $\log t_{\text{peak}}$ (cf. Equation 48) for the same BBH population shown in Figure 8, $\psi_{\log t_{\text{peak}}}(\log t_{\text{peak}}|M_{\text{BH}}, q_{\text{BH}}, z' = 0)$, and their dependence on the properties of the BBHs and their host galaxies. The curves with different colors and the texts have meanings similar to those in Figure 8. Compared to those in Figure 8, the distributions are less sensitive to the BBH mass ratios.

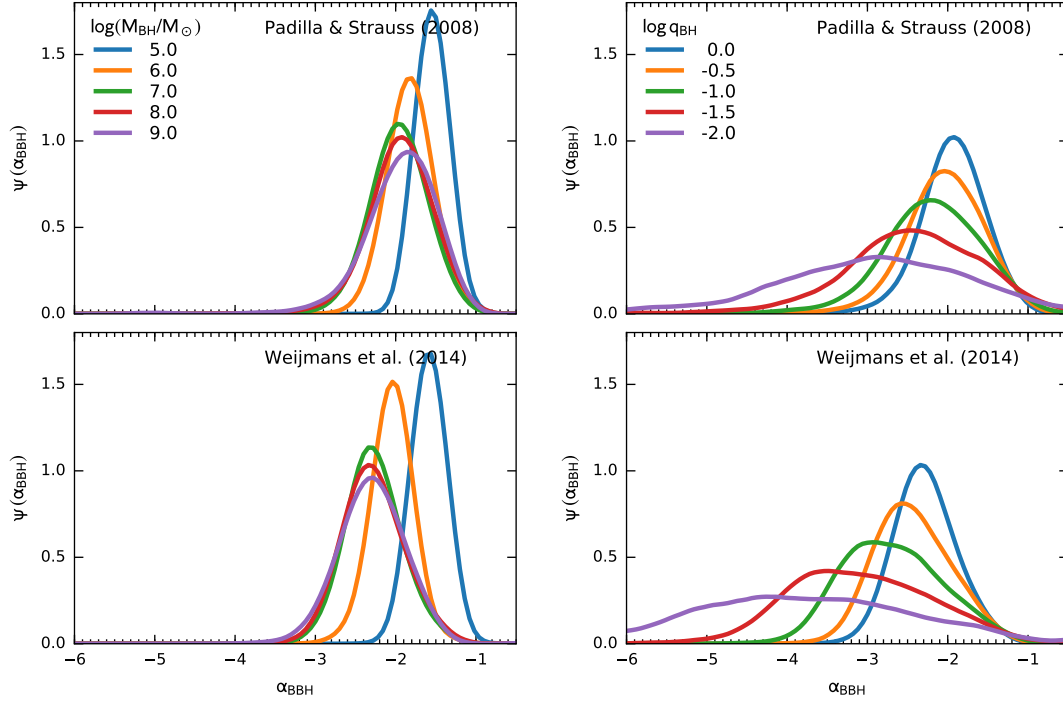


Figure 10. Probability distributions of the slope of BBH evolution tracks α_{BBH} (cf. Equation 48) in the logarithmic evolution timescale $\log t_{\text{evol}}$ versus logarithmic semimajor axis $\log a$ space during the hard-binary stage of the same BBH population shown in Figure 8, $\psi_{\alpha_{\text{BBH}}}(\alpha_{\text{BBH}}|M_{\text{BH}}, q_{\text{BH}}, z' = 0)$, and their dependence on the properties of the BBHs and their host galaxies. The curves, the colors, and the texts have meanings similar to those in Figure 8. In the upper panels, the galaxy shape distribution of early-type galaxies from Weijmans et al. (2014) is adopted. Whereas in the lower panels, the shape distribution of Padilla & Strauss (2008) is adopted. The results obtained by adopting the shape distribution of Rodríguez & Padilla (2013) are very close to those obtained by adopting the shape distribution of Padilla & Strauss (2008), and are not shown here.

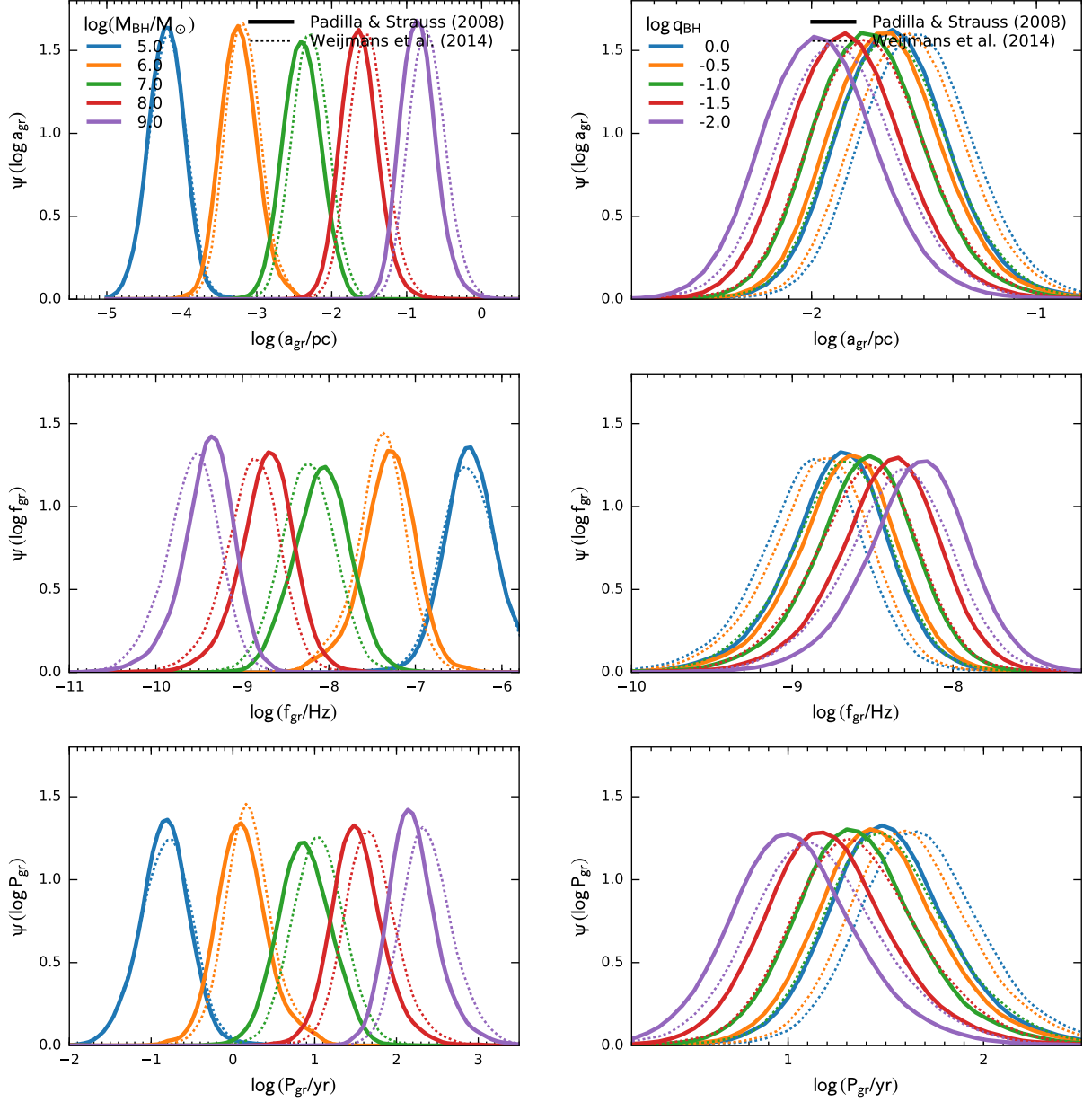


Figure 11. Probability distributions of the logarithms of the semimajor axis $\log a_{\text{gr}}$ (top panel), the GW frequency $\log f_{\text{gr}}$ (middle panel), and the orbital period $\log P_{\text{gr}}$ (bottom panel) at which the BBHs enter the gravitational stage for the same population of BBHs shown in Figure 8, i.e., $\psi_{\log a_{\text{gr}}}(\log a_{\text{gr}}|M_{\text{BH}}, q_{\text{BH}}, z' = 0)$, $\psi_{\log f_{\text{gr}}}(\log f_{\text{gr}}|M_{\text{BH}}, q_{\text{BH}}, z' = 0)$, and $\psi_{\log P_{\text{gr}}}(\log P_{\text{gr}}|M_{\text{BH}}, q_{\text{BH}}, z' = 0)$. In each panel, the solid and the dotted curves show the results obtained with adopting the galaxy shape distributions of Padilla & Strauss (2008) and Weijmans et al. (2014), respectively. The results obtained with adopting the galaxy shape distribution of Rodríguez & Padilla (2013) are very close to those of Padilla & Strauss (2008) and are therefore not shown in the figure.

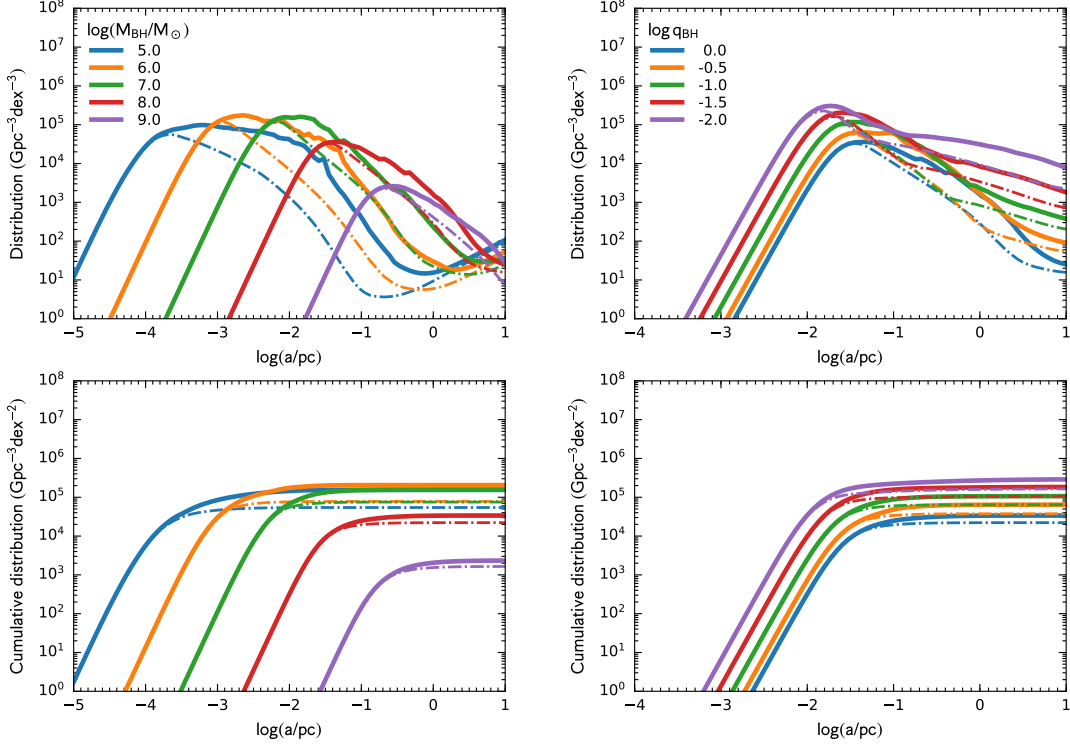


Figure 12. Semimajor axis distributions of the surviving BBHs at redshift $z = 0$. In the upper panels the vertical axis represents the variables $aM_{\text{BH}}q_{\text{BH}}(\ln 10)^3\Phi_{\text{BBH}}(M_{\text{BH}}, q_{\text{BH}}, a, z = 0)$. In the lower panels the vertical axis represents the cumulative semimajor axis distribution over semimajor axis of the corresponding upper panel, $\int_0^a M_{\text{BH}}q_{\text{BH}}(\ln 10)^2\Phi_{\text{BBH}}(M_{\text{BH}}, q_{\text{BH}}, a', z = 0) da'$. In the left panels, the BBH mass ratio is set to $q_{\text{BH}} = 1.0$, and the different colors represent the different BBH total masses M_{BH} , as labeled by the texts. In the right panels, the BBH total mass is set to $M_{\text{BH}} = 10^8 M_{\odot}$, and the different colors represent the different BBH mass ratios q_{BH} , as labeled by the texts. In the figure, the dot-dashed curves represent the contribution only by those BBHs whose coalescence timescale τ_0 are shorter than the Hubble timescale, and the solid curves represent all the contribution. As seen from the differences between the solid and the dot-dashed curves, the distributions of the surviving BBHs with large semimajor axes (at the binary stages) are mainly contributed by those not being able to finish their final coalescences within the Hubble timescale, while the distributions of the BBHs with low semimajor axes (at the gravitational radiation stage) are those that can coalesce within the Hubble timescale. In the calculation, we adopt the GSMF from Behroozi et al. (2019) and the galaxy fractional merger rate from Rodriguez-Gomez et al. (2015), and the galaxy shape distribution of Padilla & Strauss (2008) is used in modeling the BBH evolution (similarly for all the figures below). All the BH–host galaxy relations listed in Table 1 are used, and the median distributions obtained with those relations are shown in the figure (similarly for Figs. 13–17 below). See Section 5.3.

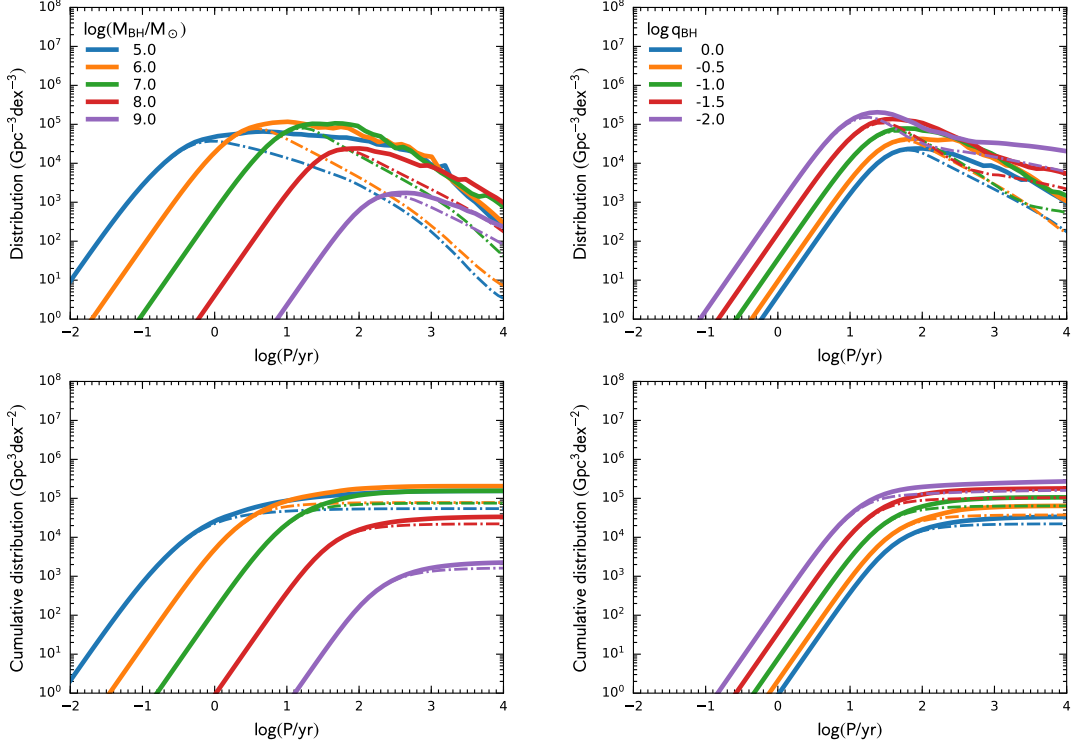


Figure 13. The orbital period distributions and the cumulative orbital period distributions of the same BBH populations shown in Figure 12. The line colors and styles have the same meanings as those shown in the corresponding panels of Figure 12. We set $q_{\text{BH}} = 1.0$ in the left panels and $M_{\text{BH}} = 10^8 M_{\odot}$ in the right panels, as shown in Figure 12. See Section 5.3.

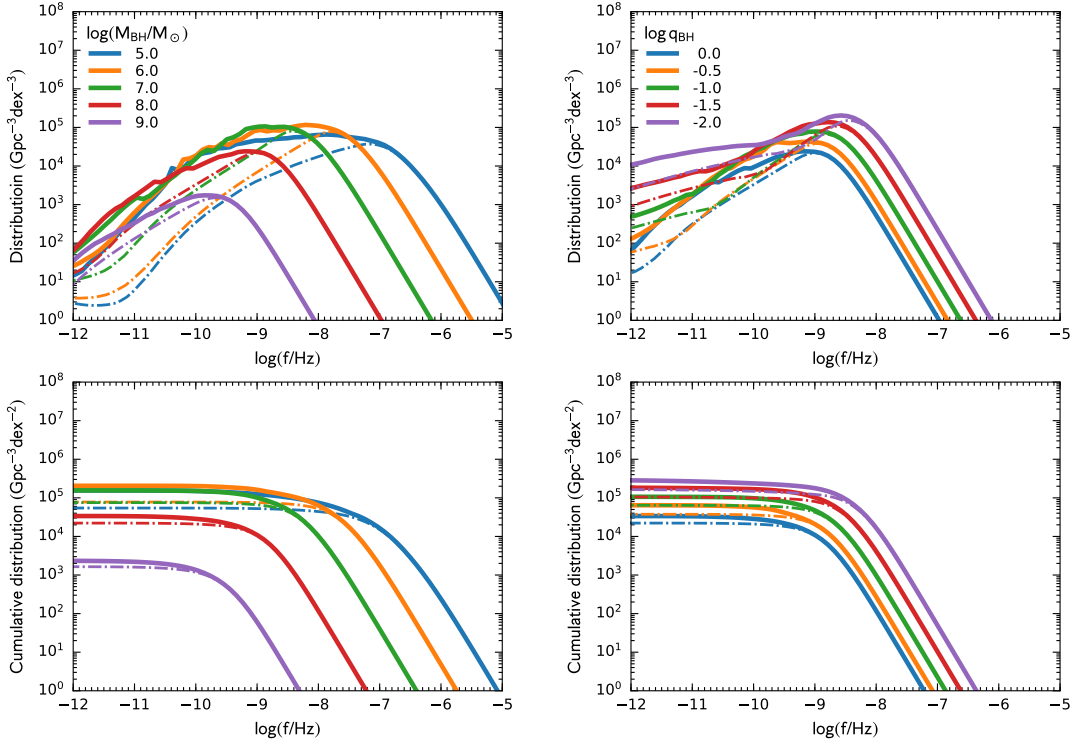


Figure 14. The GW frequency distributions and the cumulative GW frequency distributions of the same BBH populations shown in Figure 12. The line colors and styles have the same meanings as those shown in the corresponding panels of Figure 12. We set $q_{\text{BH}} = 1.0$ in the left panels and $M_{\text{BH}} = 10^8 M_{\odot}$ in the right panels, as shown in Figure 12. See Section 5.3.

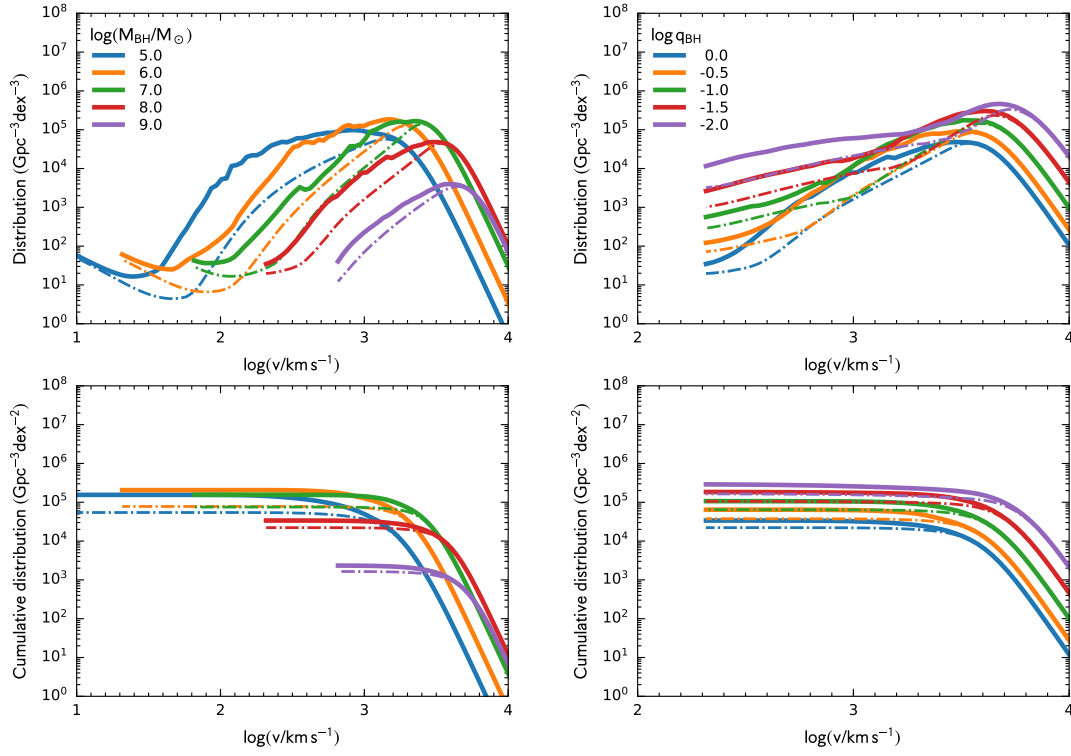


Figure 15. The BBH relative velocity distribution and the cumulative distribution of the same BBH populations shown in Figure 12, where the relative velocities are obtained by assuming that BBHs are on circular orbits, given their masses and separations. The line colors and styles have the same meanings as those shown in the corresponding panels of Figure 12. We set $q_{\text{BH}} = 1.0$ in the left panels and $M_{\text{BH}} = 10^8 M_{\odot}$ in the right panels, as shown in Figure 12. See Section 5.3.

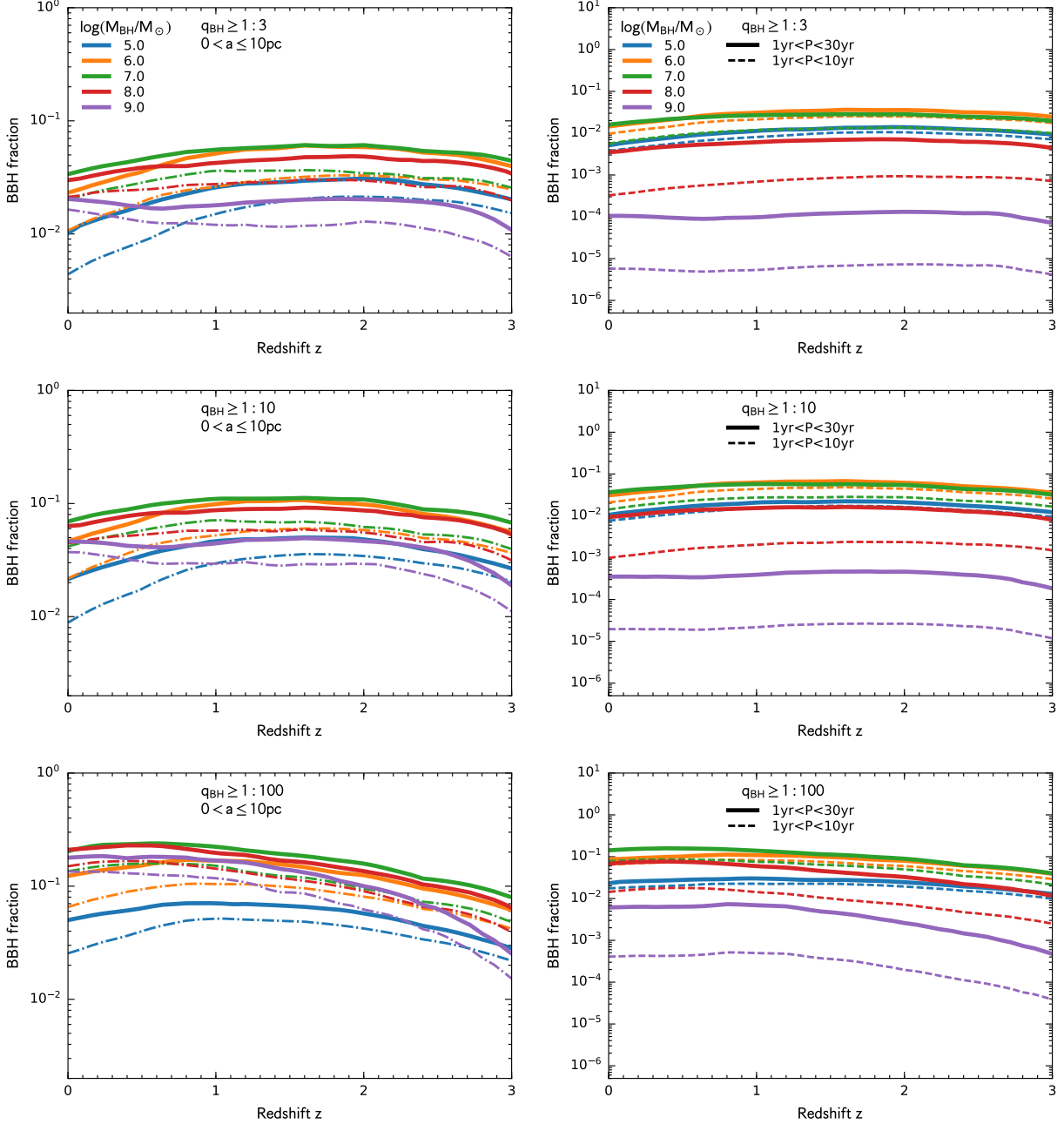


Figure 16. The fractions of the MBHs that are surviving BBHs with $q_{\text{BH}} \geq 1/3, 1/10, 1/100$, as a function of redshift. In the left panels, only BBHs with semimajor axis $0 < (a/\text{pc}) \leq 10$ are included, and in the right panels, only BBHs with orbital periods $1 \text{ yr} < P < 10 \text{ yr}$ or $1 \text{ yr} < P < 30 \text{ yr}$ are included. The different colors represent the different BBH total masses M_{BH} , as denoted by the texts. The dot-dashed curves represent the contribution only by those BBHs whose coalescence timescale τ_0 are shorter than the Hubble timescale at the corresponding redshift, and the solid curves represent all the contribution. As seen from the top left panel, the surviving BBH fractions with $q_{\text{BH}} \geq 1/3$ are around $\sim 1\%$ – 3% (solid curves) for different BH masses, and more than about a half of them have total evolution timescales shorter than the Hubble timescale. The surviving BBH fractions with $q_{\text{BH}} \geq 1/100$ increase to $\sim 10\%$ in the bottom left panel. As seen from the top right panel, at $z = 0$, the fractions of surviving BBHs with $q_{\text{BH}} \geq 1/3$ and orbital periods $1 \text{ yr} < P < 10 \text{ yr}$ are expected to be $\sim 0.5\%$ – 1% in MBHs with $M_{\text{BH}} \sim 10^6$ – $10^7 M_{\odot}$, the fractions of those with $1 \text{ yr} < P < 30 \text{ yr}$ are expected to be $\sim 2\%$ in MBHs with $M_{\text{BH}} \sim 10^6$ – $10^7 M_{\odot}$, and the fractions decrease in MBHs with other masses, down to 10^{-4} for $M_{\text{BH}} \sim 10^9 M_{\odot}$. The fractions are not sensitive to redshifts at $z \lesssim 3$. The fractions of surviving BBHs with $q_{\text{BH}} \geq 1/100$ and $1 \text{ yr} < P < 30 \text{ yr}$ increase to $\sim 10\%$ for $M_{\text{BH}} \sim 10^6$ – $10^7 M_{\odot}$ and $\sim 6 \times 10^{-3}$ for $M_{\text{BH}} \sim 10^9 M_{\odot}$, as shown in the bottom right panel. See Section 5.3.

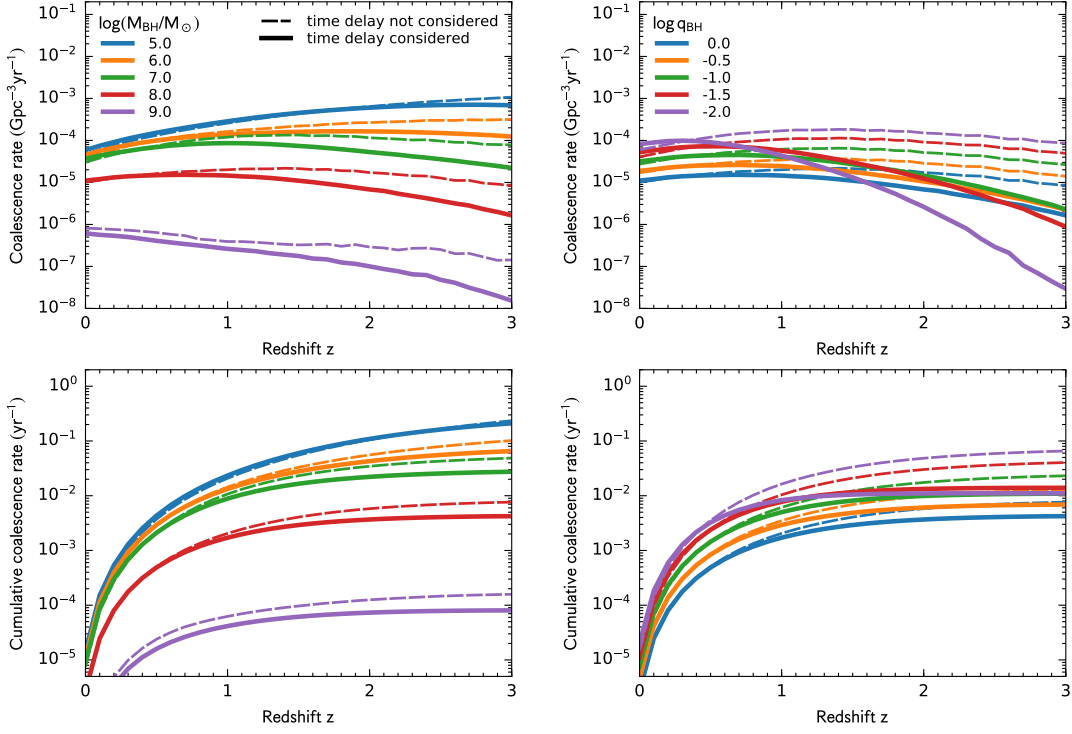


Figure 17. The BBH coalescence rates as a function of redshift, and their dependence on BBH total masses and mass ratios. In the upper panels, the vertical axis represents the variable $M_{\text{BH}}q_{\text{BH}}(\ln 10)^2 R_{\text{BH}}(M_{\text{BH}}, q_{\text{BH}}, z)$ (see Eq. 20). In the lower panels, the vertical axis represents the volume-integrated rates for for the corresponding upper panel, i.e., $\int_0^z M_{\text{BH}}q_{\text{BH}}(\ln 10)^2 R_{\text{BH}}(M_{\text{BH}}, q_{\text{BH}}, z) dV_c/dz/(1+z) dz$, where dV_c is the comoving volume of the universe at the redshift range $z \rightarrow z + dz$. The line colors have the same meanings as those shown in the corresponding panels of Figure 12. We set $q_{\text{BH}} = 1.0$ in the left panels and $M_{\text{BH}} = 10^8 M_{\odot}$ in the right panels, as shown in Figure 12. The solid and the dashed lines represent the results obtained with and without including the time delays between host galaxy mergers and embedded BBH coalescences, respectively, and their differences are significant for low BBH mass ratios and at high redshifts. In addition, the low q_{BH} cases illustrated in the right panels suggest that the ignorance of the time delays between galaxy mergers and BBH coalescences may lead to an overestimate of the LISA detection rates. See Sections 5.4 and 5.7.

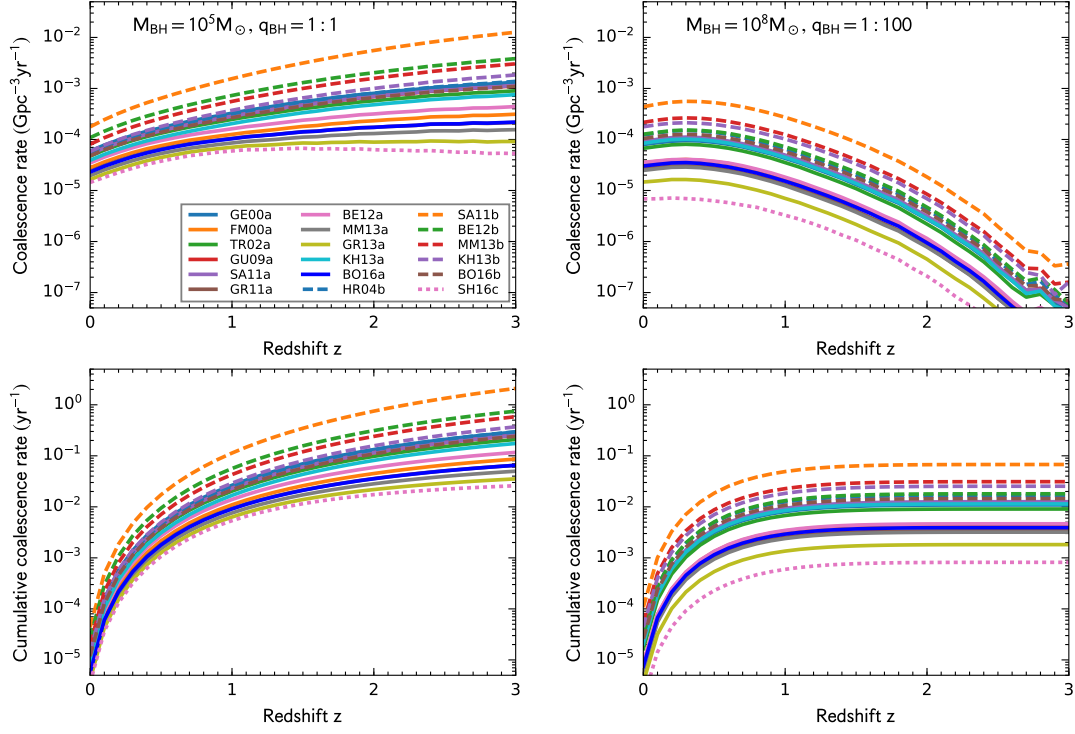


Figure 18. The BBH coalescence rates obtained with the different sets of BH–host galaxy relations listed in Table 1. The vertical axes represent the same variables as those in the corresponding panels of Figure 17, and the time delays between host galaxy mergers and embedded BBH coalescences are included. The left panels show the results for the case of $(M_{\text{BH}}, q_{\text{BH}}) = (10^5 M_{\odot}, 1)$, and the right panels show the results for the case of $(M_{\text{BH}}, q_{\text{BH}}) = (10^8 M_{\odot}, 0.01)$. As seen from the figure, the difference in the BBH coalescence rates caused by the difference in the BH–host galaxy relations can be up to two orders of magnitude. See Section 5.4.

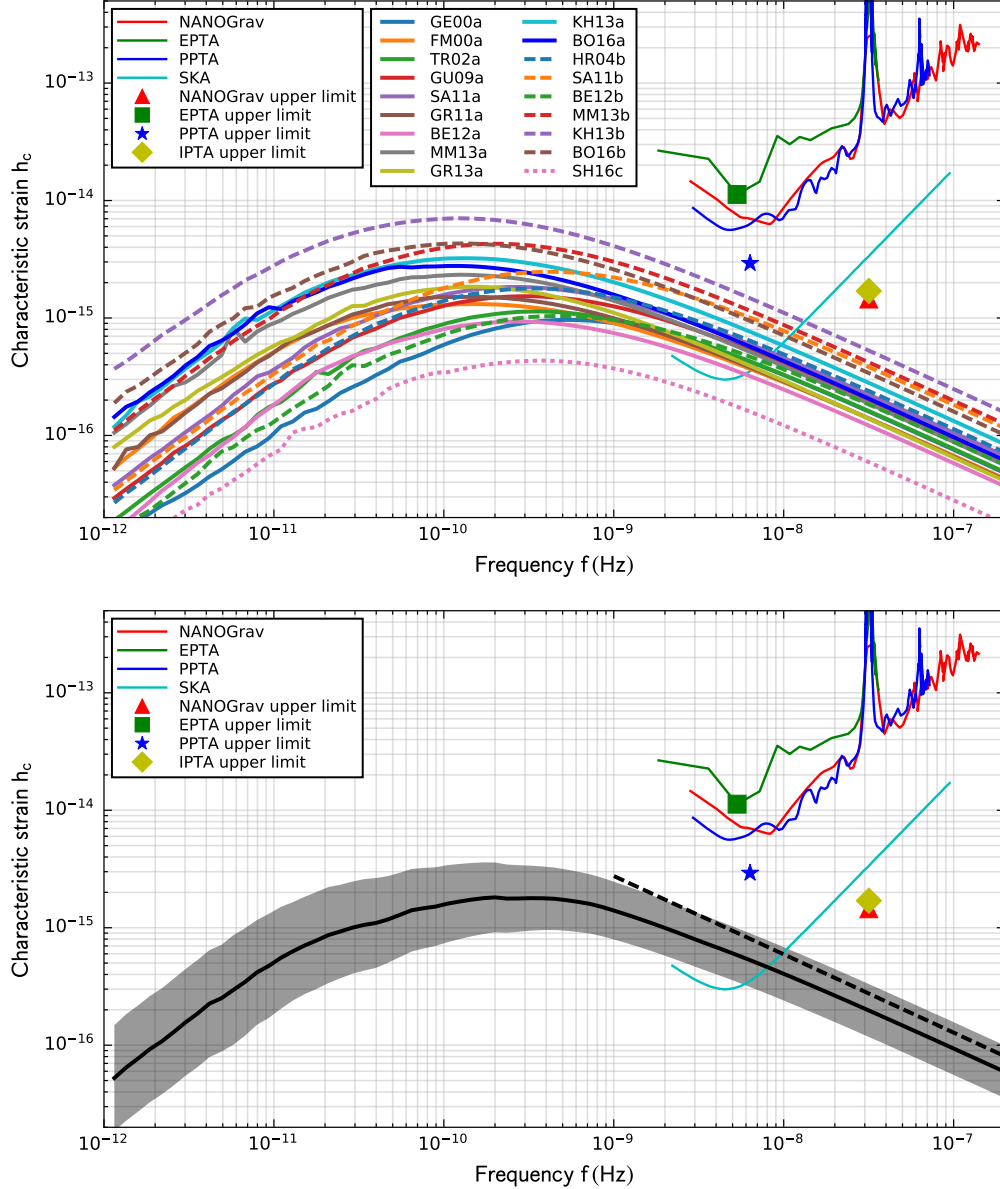


Figure 19. The characteristic strain spectra h_c of the stochastic GWB from the cosmic population of BBHs (cf. Eq. 31), as a function of the observer-rest frequency f around the PTA band. The upper panel shows the characteristic strain spectra h_c of the stochastic GWB from the cosmic population of BBHs expected from the model in this work. The different curves covering the whole frequency range in the upper panel represent the results obtained with the different sets of BH–host galaxy relations listed in Table 1, which differ by one order of magnitude and contribute significantly to the uncertainty in the estimate of the stochastic GWB. In the lower panel, the black solid curve and the shaded region represent the median and the standard deviation of the spectra shown in the upper panel. The dashed curve represents the median spectrum obtained without including the time delays between the galaxy mergers and BBH coalescences in the model. The spectrum at the high-frequency end follows the unique $-2/3$ power law of the observational frequency. The bending of the strain spectrum shown at the low-frequency end ($\lesssim 10^{-9}$ Hz) is caused by that a significant part of the BBH energy loss is driven by three-body interactions with surrounding stars, and the spectra correspond to the BBH evolution tracks at $a \gtrsim a_{\text{gr}}$. In the figure, the red, green, blue, and cyan curves located close to the upper right corner are the currently most stringent sensitivity curves obtained by NANOGrav (Arzoumanian et al. 2018), EPTA (Lentati et al. 2015), PPTA (Shannon et al. 2015), and the expected sensitivity curves of the planned PTAs based on SKA (Bonetti et al. 2018), respectively, as labeled by the texts. The red, green, blue, and yellow symbols mark the currently upper limit of the GWB set by NANOGrav, EPTA, PPTA, and IPTA, respectively. As seen from the figure, the estimated maximum strain amplitude at $f = 1 \text{ yr}^{-1}$ is below the current upper limit set by the PTA experiments by a factor of ~ 2 , while the median of the predicted values is smaller than the current upper limit by a factor of ~ 5 . The GWB strain amplitudes at a little lower frequency ~ 10 nHz are expected to be within the detection ability of future experiments (e.g., SKA). See Section 5.5.

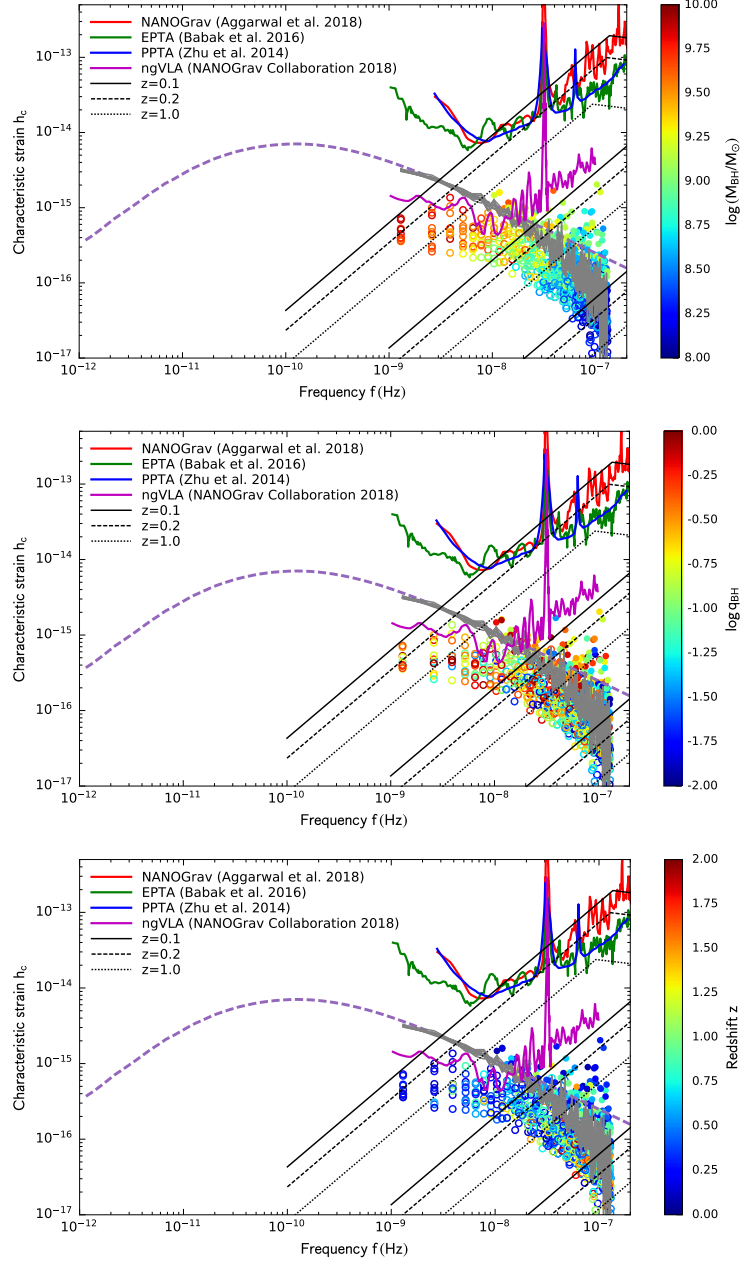


Figure 20. Demonstration of the GW strain spectrum fluctuation at the high-frequency end of the PTA band due to the limited number of BBH systems within those frequencies, and the prospects for detecting individual BBH sources with characteristic strain amplitudes standing above the average background at the PTA band. The distributions of the characteristic strain amplitudes of individual BBH sources are obtained from ten realizations of the cosmic population of BBHs generated in our model (see Section 5.6). In each panel, the purple dashed curve shows the same strain spectrum as the one in Figure 19, obtained with the $M_{\text{BH}}-M_*$ relation of Kormendy & Ho (2013). Each grey curve represents the background strain spectrum of one realization of the cosmic population of BBHs, obtained by removing the loudest source in each frequency bin and then adding up the GW signal of the rest sources (Eq. 55). The grey curves fluctuate at high frequencies, due to the limited number of the BBH sources within these frequencies. The loudest source in each frequency bin is shown by a color circle in the figure, and it is shown by a filled circle if it is loud enough to stand above its corresponding background (grey curve). The different colors in circles represent different total BBH masses, different BBH mass ratios, and different redshifts in the top, the middle, and the bottom panels, respectively. The characteristic strain amplitudes of the individual sources within the given frequency bins are obtained by assuming an observational run lasting $T_{\text{obs}} = 25$ years. At the upper right corner of the panels, the red curve represents the 95% upper limit on the characteristic strain amplitude of individual continuous sources, based on a Bayesian analysis of the NANOGrav 11-year data set (Aggarwal et al. 2018); the green curve shows the same limit, but based on a \mathcal{F}_p statistics analysis of the EPTA data set (see Figure 6 in Babak et al. 2016); the blue curve represents the sensitivity curve towards the median sensitive sky position shown in Figure 10 of Zhu et al. (2014), based on an analysis of the PPTA DR1; and the magenta curve represents the expected sensitivity curve of the planned PTAs based on Next-Generation Very Large Array (ngVLA; NANOGrav Collaboration 2018). As a reference, the broken black lines (see Eq. 58) illustrate the characteristic strain amplitude of some example BBH systems as a function of observer-rest frequency. The example BBHs have the same mass ratios $q_{\text{BH}} = 0.1$, different total BBH masses $M_{\text{BH}} = 10^{10}$, 10^9 , and $10^8 M_{\odot}$ from the top to bottom (given the same line style), and different redshifts $z = 0.1$ (solid), 0.2 (dashed), and 1.0 (dotted) shown by the different line styles. The black lines are also obtained by assuming an observational run lasting $T_{\text{obs}} = 25$ years for those example BBH systems.

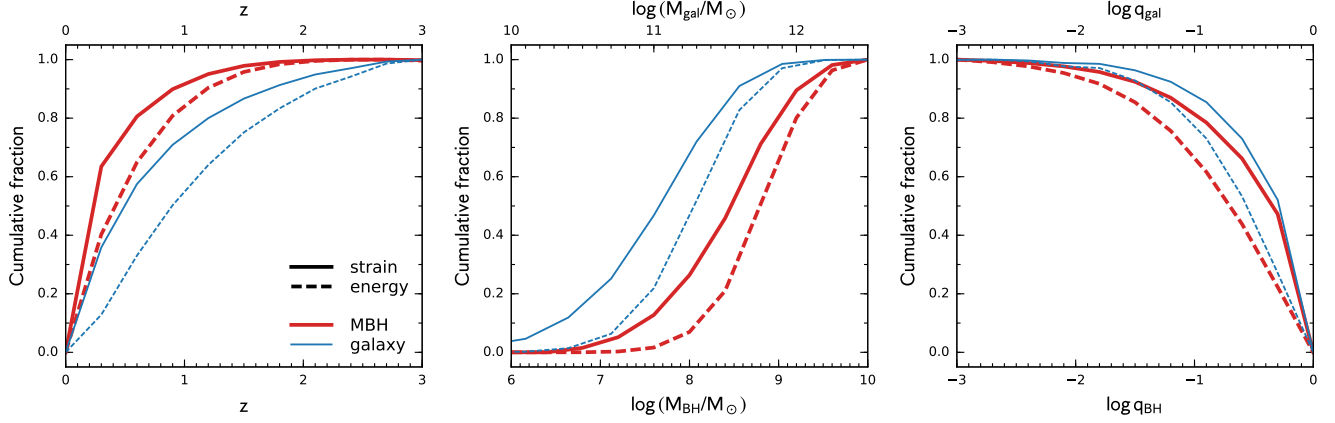


Figure 21. Cumulative fractions of the GWB energy density (dashed) and the characteristic strain amplitude (solid) at the observer-rest frequency $f = 1 \text{ yr}^{-1}$. The left, the middle, and the right panels show the fractions contributed by galaxy mergers or BBH mergers at redshift $< z$, total stellar mass $< M_{\text{gal}}$ or BBH mass $< M_{\text{BH}}$, mass ratios $> q_{\text{gal}}$ or $> q_{\text{BH}}$ (right), respectively. The blue curves represent galaxy mergers, and the red curves represent BBH mergers. The $M_{\text{BH}}-M_*$ relation of [Kormendy & Ho \(2013\)](#) is adopted in this figure. As seen from the figure, most of the GWB energy density is contributed by galaxy or BBH mergers within redshift lower than 2, with total galaxy mass within $\sim 10^{10}-10^{12}M_{\odot}$ or BBH mass within $\sim 10^8-10^{10}M_{\odot}$, and with merging galaxy or BH mass ratio greater than ~ 0.01 . See Section 5.5.

Table 1
The BH–host galaxy relations

Abbr	$\tilde{\alpha}$	$\tilde{\beta}$	$\tilde{\gamma}$	$\tilde{\epsilon}$	$\log(A_{\text{yr}}^{\text{pl}})$	$\log(A_{\text{yr}})$	Drop dex	$\log(f_{\text{turn}}/\text{Hz})$	κ_{gw}	γ_{gw}	Reference
GE00a	–	3.75	8.08	0.30	-15.69	-15.80	0.11	-9.28	3.27	0.27	Gebhardt et al. (2000)
FM00a	–	4.80	8.14	0.30	-15.71	-15.85	0.14	-9.87	4.57	0.12	Ferrarese & Merritt (2000)
TR02a	–	4.02	8.13	0.30	-15.67	-15.79	0.12	-9.48	3.65	0.20	Tremaine et al. (2002)
GU09a	–	3.96	8.23	0.31	-15.58	-15.70	0.13	-9.54	3.63	0.21	Gültekin et al. (2009)
SA11a	–	4.00	8.29	0.33	-15.52	-15.65	0.13	-9.60	3.78	0.19	Sani et al. (2011)
GR11a	–	5.13	8.13	0.34	-15.71	-15.85	0.14	-9.84	3.94	0.17	Graham et al. (2011)
BE12a	–	4.42	7.99	0.36	-15.79	-15.91	0.12	-9.61	4.18	0.15	Beifiori et al. (2012)
MM13a	–	5.64	8.32	0.38	-15.56	-15.73	0.17	-9.93	3.96	0.17	McConnell & Ma (2013)
GR13a	–	6.08	8.15	0.41	-15.68	-15.86	0.18	-9.84	3.38	0.25	Graham & Scott (2013)
KH13a	–	4.42	8.50	0.29	-15.40	-15.55	0.15	-9.90	4.25	0.15	Kormendy & Ho (2013)
BO16a	–	5.35	8.32	0.49	-15.51	-15.69	0.18	-9.98	3.99	0.17	van den Bosch (2016)
HR04b	1.12	–	8.20	0.30	-15.50	-15.62	0.12	-9.50	3.72	0.20	Håring & Rix (2004)
SA11b	0.79	–	8.20	0.37	-15.30	-15.42	0.12	-9.41	3.59	0.21	Sani et al. (2011)
BE12b	0.91	–	7.84	0.46	-15.62	-15.73	0.11	-9.36	3.64	0.19	Beifiori et al. (2012)
MM13b	1.05	–	8.46	0.34	-15.24	-15.38	0.14	-9.72	3.74	0.20	McConnell & Ma (2013)
KH13b	1.17	–	8.69	0.29	-15.11	-15.28	0.17	-9.94	3.70	0.19	Kormendy & Ho (2013)
BO16b	1.21	–	8.33	0.49	-15.31	-15.47	0.16	-9.89	3.74	0.19	van den Bosch (2016)
SH16c	0.50	4.50	7.70	0.25	-16.09	-16.22	0.14	-9.48	3.38	0.24	Shankar et al. (2016)

Note. — The BH–host galaxy relations in different works and the characteristic strain amplitudes of the stochastic GWBs obtained with the relations. The BH–host galaxy relations are described by the parameters $\tilde{\alpha}$, $\tilde{\beta}$, $\tilde{\gamma}$ (see Eq. 46), and the intrinsic scatter of the relation $\tilde{\epsilon}$ (see Section 4.4), and the references to the relations are listed in the last column of the table. Regarding the relation in [Ferrarese & Merritt \(2000\)](#) (FM00a), an intrinsic scatter is not provided in the original work; and here a scatter of 0.3 dex is assumed, as listed in the table. The $\log(A_{\text{yr}})$ and $\log(A_{\text{yr}}^{\text{pl}})$ represent the strain amplitudes at $f = 1 \text{ yr}^{-1}$, obtained with and without including the time delays between galaxy mergers and BBH coalescences in our model, respectively. The column of “Drop” gives the values of $\log(A_{\text{yr}}^{\text{pl}}) - \log(A_{\text{yr}})$. The parameter f_{turn} is the turnover frequency of the obtained GWB spectrum, κ_{gw} is the power describing the spectrum at the low-frequency end of the spectrum, and γ_{gw} is a parameter to describe the shape transition of the GWB spectrum around the turnover frequency (see Eqs. 53 and 54). The numbers in bold are about the medians of $\log(A_{\text{yr}})$ and κ_{gw} , respectively.

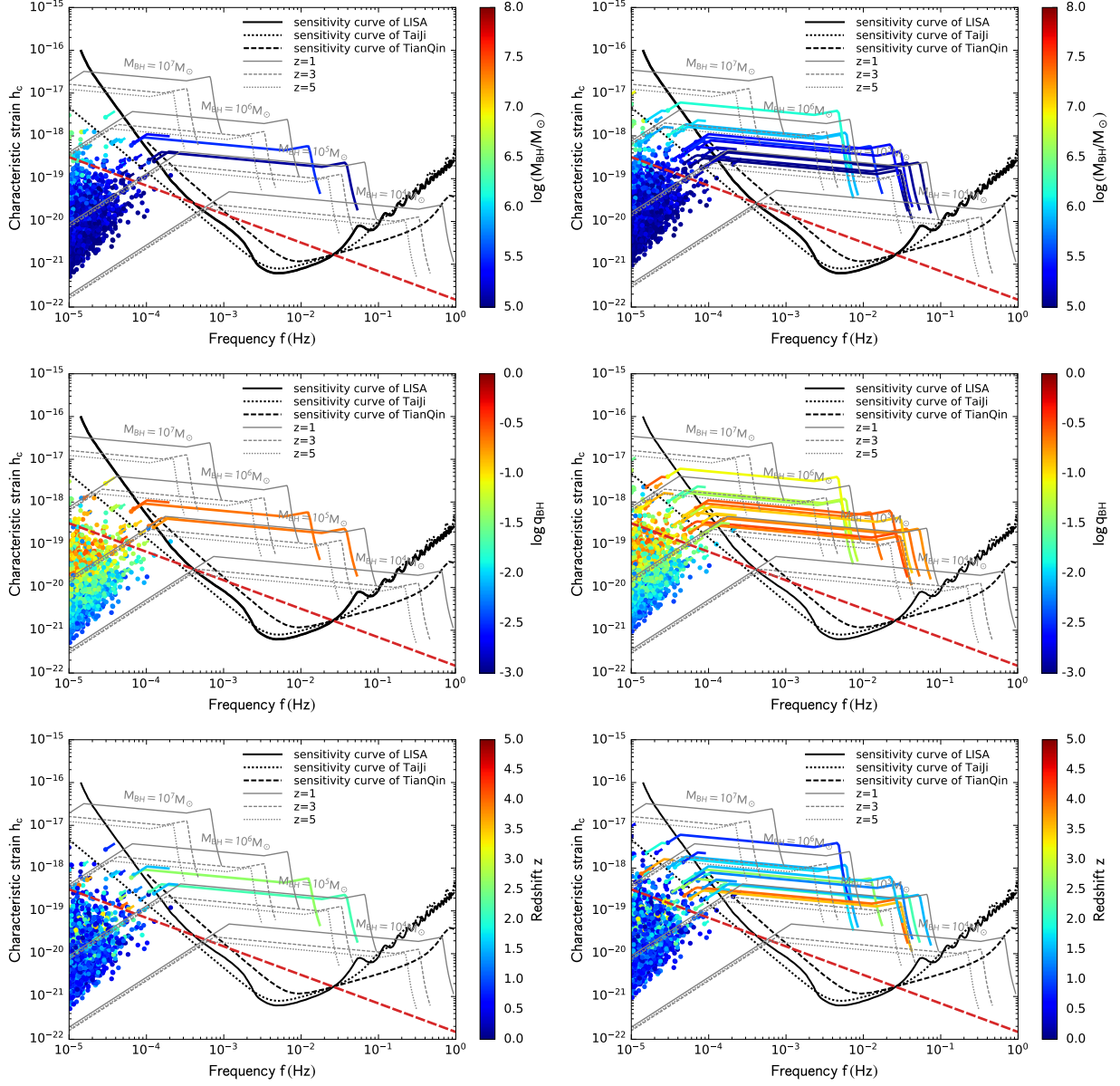


Figure 22. Demonstration of prospects for the detection of merging BBHs around the LISA frequency band. The black solid curve is the sensitivity curve of the LISA detector (shown in Figure 1 of [Amaro-Seoane et al. 2017](#)), the black dotted curve is for Taiji ([Ruan et al. 2018](#)), and the black dashed curve is for TianQin ([Wang et al. 2019](#)). The red dashed line represents a reference to the characteristic strain spectrum of the stochastic background obtained by applying Equation (31) in our model and extending the involved model gradients to the LISA band. Also as a reference, the grey curves illustrate the evolution tracks of some example merging BBH systems in the GW strain-frequency space. The example BBHs have the same mass ratio $q_{\text{BH}} = 0.1$, different total masses as labeled on the curves, and different redshifts shown by different line styles and labeled by the texts. The GW characteristic strains of individual BBH generated from one realization of the BBH population in our model are shown as color points at the beginning, with the color scales representing the BBH total masses, mass ratios, and redshifts in the top, middle, and bottom panels, respectively. The color solid lines start from the color points and correspond to the evolution tracks of the same sources during three years' observation in the left panels and during ten years' observation in the right panels. The $M_{\text{BH}}-M_*$ relation of [Kormendy & Ho \(2013\)](#) is adopted in this figure. The detection rate demonstrated in this figure is $\sim 0.9 \text{ yr}^{-1}$. See Section 5.7.